



HAL
open science

Laser spectroscopy of tin across $N=82$

Liss Vázquez Rodríguez

► **To cite this version:**

Liss Vázquez Rodríguez. Laser spectroscopy of tin across $N=82$. Nuclear Experiment [nucl-ex]. Université Paris Saclay (COMUE), 2018. English. NNT : 2018SACLS339 . tel-03429865

HAL Id: tel-03429865

<https://theses.hal.science/tel-03429865v1>

Submitted on 16 Nov 2021

HAL is a multi-disciplinary open access archive for the deposit and dissemination of scientific research documents, whether they are published or not. The documents may come from teaching and research institutions in France or abroad, or from public or private research centers.

L'archive ouverte pluridisciplinaire **HAL**, est destinée au dépôt et à la diffusion de documents scientifiques de niveau recherche, publiés ou non, émanant des établissements d'enseignement et de recherche français ou étrangers, des laboratoires publics ou privés.

Laser spectroscopy of tin across $N=82$

Thèse de doctorat de l'Université Paris-Saclay
préparée à l'Université Paris-Sud

Ecole doctorale n°576
Particules, Hadrons, Énergie, Noyau, Instrumentation, Imagerie,
Cosmos et Simulation (PHENIICS)
Spécialité de doctorat : Structure et réactions nucléaires

Thèse présentée et soutenue à Orsay, le 28 Septembre 2018, par

Liss Vázquez Rodríguez

Composition du Jury :

Dr. Elias Khan Professeur, Institut de physique nucléaire d'Orsay, IPN	Président
Dr. Bradley Cheal Maître de conférences, Université de Liverpool	Rapporteur
Dr. Bertram Blank Directeur de recherche CNRS, Centre Etudes Nucléaires de Bordeaux Gradignan, CENBG	Rapporteur
Dr. Dimiter Loukanov Balabanski Professeur, Extreme Light Infrastructure - Nuclear Physics, ELI-NP	Examineur
Dr. Luis Fraile Professeur, Organisation européenne pour la recherche nucléaire, CERN	Examineur
Dr. Jean-Charles Thomas Chargé de recherche CNRS, Grand accélérateur national d'ions lourds, GANIL	Examineur
Dr. Deyan Yordanov Chargé de recherche CNRS, Institut de physique nucléaire d'Orsay, IPN	Directeur de thèse

Contents

1	Introduction	1
1.1	Physics motivation	2
1.2	Aim of this work	3
2	Atomic and nuclear structures	5
2.1	Atomic Hamiltonian	5
2.1.1	Angular momenta in many-electron atoms	8
2.1.2	Atomic levels of the tin atom	9
2.2	Nuclear Hamiltonian	11
2.2.1	Nuclear spin and parity	14
2.2.2	Nuclear magnetic dipole moment	15
2.2.3	Nuclear electric quadrupole moment	16
2.3	Atomic hyperfine structure	20
2.3.1	Magnetic dipole interaction	22
2.3.2	Electric quadrupole interaction	23
2.3.3	Isotope shift	25
3	Collinear laser spectroscopy	31
3.1	The ISOLDE facility	31
3.2	Experimental setup	33
3.2.1	Voltages read-out	35
3.2.2	Laser system	38
3.3	Data collection	38
3.3.1	Lineshapes observation	38
4	Data analysis and results	41
4.1	Independent analysis	41
4.1.1	Fitting procedure I	41
4.1.2	The $5p^2\ ^1S_0 \rightarrow 5p6s\ ^1P_1$ transition	42
4.1.3	The $5p^2\ ^3P_0 \rightarrow 5p6s\ ^3P_1$ transition	46
4.2	Simultaneous analysis	49
4.2.1	Fitting procedure II	49

4.2.2	<i>A</i> and <i>B</i> -ratios	50
4.2.3	Even-even isotopes	50
4.3	Nuclear moments	54
4.3.1	Magnetic moments	54
4.3.2	Quadrupole moments	57
4.4	Charge radii	63
4.4.1	Isotope and isomer shifts	63
4.4.2	King plot	65
4.4.3	Charge radii	66
5	Conclusions	73
	Bibliography	79
	Contribution to the ISOLDE Newsletter 2018	81
	Paper in preparation	83
	“Other work: Shell model calculations for Mg”	93
	J. Phys. G: Nucl. Part. Phys. 44 (2017) 075104	98
	Acknowledgments	105

List of Figures

1.1	Isotopic chain of tin	3
2.1	Atomic levels of tin	10
2.2	Woods-Saxon potential	14
2.3	Hyperfine states of tin in the $5p6s\ ^1P_1$ and $5p6s\ ^3P_1$	21
2.4	Size of the hyperfine splitting of the $5p6s\ ^3P_1$ electronic level for isotopes with $I = 1/2$	24
2.5	Mass and field shift contribution	26
3.1	ISOLDE	32
3.2	ISCOOL	33
3.3	COLLAPS	34
3.4	Stability of ISCOOL voltage	35
3.5	KEPCO amplification factor	36
3.6	Block diagram of the data acquisition system	37
3.7	Reference isotope	39
4.1	Hyperfine structure of ^{133}Sn in the $5p6s\ ^1P_1$ level	44
4.2	Hyperfine structure of ^{129}Sn in the $5p6s\ ^1P_1$ level	45
4.3	Hyperfine structure of ^{133}Sn in the $5p6s\ ^3P_1$ level	47
4.4	Hyperfine structure of ^{129}Sn in the $5p6s\ ^3P_1$ level	48
4.5	Hyperfine spectra of ^{130}Sn in the $5p6s\ ^3P_1$ and $5p6s\ ^1P_1$ levels .	52
4.6	Hyperfine spectra of ^{128}Sn in the $5p6s\ ^3P_1$ and $5p6s\ ^1P_1$ levels .	53
4.7	Magnetic moments of odd isotopes in the tin chain	54
4.8	Magnetic moments of the $h_{11/2}$ neutron states in cadmium, tin and tellurium	57
4.9	Quadrupole moments of odd-isotopes in the tin chain	58

4.10	Quadrupole moments of the $h_{11/2}$ states in tin compared to those calculated using the seniority scheme	59
4.11	Quadrupole moments of the $h_{11/2}$ neutron states in cadmium, indium and tin.	60
4.12	Differences between the values extracted in this work and literature values for low and high spin states	62
4.13	King plot	67
4.14	Changes in mean square nuclear charge radii	68
4.15	Differences in mean square charge radii of tin isotopes	68
4.16	Experimental root mean-square charge radius versus neutron number around closed-shells	70
4.17	Differences in mean square charge radius between $11/2$ states and $1/2, 3/2$ states	71
4.18	Comparison of mean square charge radii changes from this work to theoretical calculations of the even tin isotopes.	72
5.1	Fluorescence spectrum of ^{134}Sn in the 286-nm transition in the neutral atom.	82
5.2	Optical spectra of some chosen isotopes for the determination of the isotope shift in the $5p^2\ ^1S_0 \rightarrow 5p6s\ ^1P_1$ transition. Shown is the number of counts as a function of the relative frequency.	86
5.3	Evolution of the nuclear charge radii of the tin isotopic chain. Shown is the change in mean square nuclear charge radius $\delta \langle r^2 \rangle$ as a function of the mass number (lower x-axis), respectively the neutron number (upper x-axis). The red line shows the theoretical prediction.	89
5.4	Energy levels for ^{29}Mg	95
5.5	Experimental magnetic moments of odd-magnesium isotopes versus calculated values	96

Chapter 1

Introduction

All science is either physics or stamp collecting.

- Ernest Rutherford -

The understanding of the quantum structure of the atomic nucleus has attracted the attention of many experimentalists and theorists for more than a century. Being a complex many-body quantum system, it possesses fundamental properties, such as spin and electromagnetic moments, that are considered valuable inputs for the determination and testing of nuclear models. The systematic investigation of these observables along an isotopic (isotonic) chain reveals progressive changes in structure with respect to the number of valence nucleons. The semi-magic tin isotopes are in the center stage of this powerful line of inquiry. They form the longest known isotopic chain in the nuclear landscape accessible to current experimental studies with the highest number of stable isotopes (ten), extending from the doubly-magic nucleus with $A = 100$ up and beyond the doubly-magic nucleus with $A = 132$. The main goal of this doctoral dissertation is the determination of model-independent properties of ground and long-lived isomeric states in neutron-rich tin isotopes up to and beyond the $N = 82$ shell closure as a main tool for the understanding of the nuclear structure far away from the line of stability.

1.1 Physics motivation

The shell model of nuclei, first proposed by M. Goeppert-Mayer and J. H. D. Jensen [1], is considered the cornerstone of the nuclear physics. One of the simple foundations of this model implies that the quadrupole moments of nuclear states, for a nucleus with n valence particles (holes) in an orbital with angular momentum j , follow a simple linear relation with respect to the number of valence protons [1] or neutrons [2]. Due to this characteristic behavior, the systematics of electric quadrupole moments provide a rigorous test of the model. Linear trends, associated with unique-parity orbitals, have been observed and discussed in the cadmium [3], mercury and lead chains [4]. However, they are expected to occur only in the cases in which the proton (neutron) shells are closed, and the differences in their structure are entirely determined by differences in the number of neutrons (protons) in the valence shell, as mentioned above. The tin isotopes offer a unique opportunity for examining the origin of the “simple structure” in these “complex nuclei” through the quadrupole moments of their $11/2$ states. From the quadrupole moments available in the literature [5–8], one can not extract the true structure of the relevant states considering the accuracy and precision of the reported values. New measurements of this observable, enhancing the resolution and improving the accuracy, will help at the understanding of the causes that originate this “simple” behavior and will clarify the nuclear structure of tin itself, expected to exhibit a similar picture of simplicity.

Detailed investigations of the nuclear structure of the single-neutron nucleus ^{133}Sn through its electromagnetic moments will provide important benchmarks for the development of shell model calculations in the region. They are considered valuable inputs due to the anticipated single-particle nature of its ground state [9, 10]. Furthermore, the charge radii of those isotopes that lie outside the double shell closure will provide stringent testing of this observable at the $N = 82$ shell gap. The systematics in the region show a well-pronounced “kink” at $N = 82$ as observed at shell closures [11]. Former charge radii measurements on tin [5, 7, 8] could not be propagated beyond $N = 82$ and from a theoretical point of view, the “kink” may or may not appears according to relativistic Mean Field [12] and Hartree-Fock-Bogoliubov calculations [13].

Sn108 g: 0^+	Sn109 g: $5/2^+$	Sn110 g: 0^+	Sn111 g: $7/2^+$	Sn112 g: 0^+	Sn113 g: $1/2^+$ is: $7/2^+$	Sn114 g: 0^+
Sn121 g: $3/2^+$ is: $11/2^-$	Sn120 g: 0^+	Sn119 g: $1/2^+$ is: $11/2^-$	Sn118 g: 0^+	Sn117 g: $1/2^+$ is: $11/2^-$	Sn116 g: 0^+	Sn115 g: $1/2^+$
Sn122 g: 0^+	Sn123 g: $11/2^-$ is: $3/2^+$	Sn124 g: 0^+	Sn125 g: $11/2^-$ is: $3/2^+$	Sn126 g: 0^+	Sn127 g: $11/2^-$ is: $3/2^+$	Sn128 g: 0^+ is: 7^-
	Sn134 g: 0^+	Sn133 g: $7/2^-$	Sn132 g: 0^+	Sn131 g: $3/2^+$ is: $11/2^-$	Sn130 g: 0^+ is: 7^-	Sn129 g: $3/2^+$ is: $11/2^-$

Figure 1.1: Ground and isomeric states of tin isotopes measured in this thesis. Stable isotopes are noted by grey corners while blue corners indicate those isotopes for which nuclear properties were measured for the first time.

Therefore, the charge radius measurement of ^{133}Sn together with the one of ^{134}Sn , are essential to enable a conclusion on the evolution of the nuclear charge radii beyond the $N = 82$ shell closure.

1.2 Aim of this work

Laser spectroscopy provides a powerful technique to explore the structure of nuclei along the nuclear landscape [14, 15]. From the perturbation and splitting of the electronic energy levels by the nucleus, properties such as nuclear spin, mean-square charge radius, magnetic dipole and spectroscopic electric quadrupole moments can be extracted with high-precision and in a model-independent way. This thesis aims to investigate the nuclear structure of the neutron-rich tin isotopes by high-resolution laser spectroscopy. A primary goal has been to extend the measured chain beyond $N = 82$ in order to test the robustness of the shell gap and to assess the doubly-magic-plus-one-neutron ^{133}Sn . Information on what has been measured in this work is displayed in Fig. 1.1.

The manuscript is organized as follows: In Ch. 2, some elements of atomic and nuclear structure, as well as the theory of the nuclear moments and charge radii, are introduced. In Ch. 3, a brief description of the facility and the experimental set-up is presented. Ch. 4 is dedicated to the data analysis and the extraction of the relevant nuclear physics observables together with their interpretation. Ch. 5 is devoted to the conclusions. The contribution of this work to the ISOLDE Newsletter 2018, entitled, “*High-resolution laser spectroscopy of the neutron-rich tin isotopes*” together with an article in preparation are attached to the thesis. Another work, focused on shell model calculations in magnesium isotopes and an article entitled: “*Spin and magnetic moment of ^{23}Mg* ” are annexed to the thesis.

Chapter 2

Atomic and nuclear structures

Mathematics began to seem too much like puzzle solving. Physics is puzzle solving, too, but of puzzles created by nature, not by the mind of man.

- Maria Goeppert-Mayer -

2.1 Atomic Hamiltonian

The description of an atomic system is given by the wave function $\Psi(\vec{r}, t)$ obtained by solving the time-dependent Schrödinger equation [16]

$$i\hbar \frac{\partial \Psi}{\partial t} = \hat{H} \Psi \quad (2.1)$$

where \hat{H} is the *Hamilton linear operator*, \hbar is the *reduced Planck constant*, and i is the *imaginary unit*. The total energy is conserved when the system is closed, particles plus electromagnetic field, and the Hamilton operator in (2.1) should simultaneously describe both subsystems. In the absence of an external field, it can be separated into three different parts:

$$\hat{H} = \hat{H}_0 + \hat{H}_{\text{rep}} + \hat{H}_{S.O.} \quad (2.2)$$

The first term \hat{H}_0 is called *hydrogen-like Hamiltonian* such that:

$$\hat{H}_0 = -\frac{\hbar^2}{2M} \nabla_{\vec{R}}^2 - \frac{\hbar^2}{2m_e} \sum_{i=1}^{N_e} \nabla_{\vec{r}_i}^2 - \sum_{i=1}^{N_e} \frac{Ze^2}{|\vec{R} - \vec{r}_i|} \quad (2.3)$$

where \vec{R} and \vec{r}_i are the *position vectors* of the atomic nucleus and *i*th-electron, respectively. These vectors are in a coordinate system space-fixed at the laboratory frame. M and m_e are the mass of the nucleus and the electrons, respectively, Z is the *atomic number*, and N_e is the *number of electrons* with a charge e . \hat{H}_0 can be interpreted as the Hamiltonian of N_e non-interacting electrons moving in a central force field created by a point-nucleus. The first two terms in (2.3) hold the kinetic-energy operator of the nucleus and the N_e electrons, respectively, while the third term describes the attraction potential energy between them.

The second term in (2.2) accounts for the interelectronic repulsions between pairs of electrons,

$$\hat{H}_{\text{rep}} = \sum_{i=1}^{N_e} \sum_{j>i}^{N_e} \frac{e^2}{|\vec{r}_i - \vec{r}_j|} \quad (2.4)$$

where $|\vec{r}_i - \vec{r}_j|$ is the distance between electron i and j . The restriction $j > i$ avoids counting the same interelectronic repulsion twice and the self-repulsion.

The last term in (2.2) arises from the electromagnetic interaction between the spin and the orbital magnetic dipole moment of the electrons. It is known as the relativistic spin-orbit interaction term [17] and can be expressed as:

$$\hat{H}_{S.O.} = \frac{1}{m_e^2 c^2} \sum_{i=1}^{N_e} \frac{1}{r_i} \frac{d\hat{V}_i(r_i)}{dr_i} \hat{L}_i \cdot \hat{S}_i \quad (2.5)$$

where $\hat{V}_i(r_i)$ is an *effective potential* felt by the *i*th-electron. It is originated by the nucleus and a cloud created by the remaining $(N_e - i)$ th electrons. \hat{L}_i and \hat{S}_i are the *orbital* and the *spin angular momenta operators* for the *i*th-electron and c is the *speed of light*.

A subtle approximation is made in (2.2). The nucleus has been considered as a point of mass M and charge Ze ; therefore, the effect of its size, shape and charge distribution have been neglected. A discussion will be offered later in

this chapter.

The Hamiltonian (2.2) is time-independent; accordingly, the wave function in (2.1) can be written as a product of a time-dependent $\tau(t)$ function and a position-dependent $\psi(\{\vec{r}_i\}, \vec{R})$ function:

$$\Psi(\{\vec{r}_i\}, \vec{R}; t) = \psi(\{\vec{r}_i\}, \vec{R}) \cdot \tau(t) \quad (2.6)$$

Substituting (2.6) in (2.1) and applying the Fourier method [18], for solving partial differential equations, the time evolution of the system,

$$\tau(t) = \exp\left(-i\frac{E \cdot t}{\hbar}\right) \quad (2.7)$$

and the stationary Schrödinger equation,

$$\hat{H}\psi(\{\vec{r}_i\}, \vec{R}) = E\psi(\{\vec{r}_i\}, \vec{R}) \quad (2.8)$$

are obtained, being E the energy eigenvalues of the system. Several methods have been developed to solve the eigenvalues and eigenvectors problem (2.8) [19]. The cornerstone of those methods is the Hartree-Fock self-consistent field theory [20, 21]. It gives an approximate wave function written as a Slater determinant of one-electron spin-orbitals to which the Pauli exclusion principle applies [22],

$$\psi(\vec{r}_1, \vec{r}_2, \dots, \vec{r}_{N_e}) \approx \frac{1}{\sqrt{N_e!}} \begin{vmatrix} \phi_1(\vec{r}_1)\sigma(1) & \phi_2(\vec{r}_1)\sigma(1) & \dots & \phi_{N_e}(\vec{r}_1)\sigma(1) \\ \phi_1(\vec{r}_2)\sigma(2) & \phi_2(\vec{r}_2)\sigma(2) & \dots & \phi_{N_e}(\vec{r}_2)\sigma(2) \\ \vdots & \vdots & \ddots & \vdots \\ \phi_1(\vec{r}_{N_e})\sigma(N_e) & \phi_2(\vec{r}_{N_e})\sigma(N_e) & \dots & \phi_{N_e}(\vec{r}_{N_e})\sigma(N_e) \end{vmatrix}$$

where $\phi_j(\vec{r}_i)$, with $i, j \in [1, N_e]$, denotes the one-electron orbitals in the body-fixed frame, i.e., the coordinate system has its origin at the nucleus, and $\sigma(i)$ describes the spin functions. The latter indicate the spin of the i th-electron, which is either $\alpha(i)$ (spin up) or $\beta(i)$ (spin down). From the eigenvalues and the eigenvectors that satisfy (2.8) the well known ‘‘atomic shell model’’ comes out. This model can explain the properties in the periodic table such that the trends of the ionization energies as a function of the atomic number. It is worth to mention some definitions from this model that are significant :

- electron shell: the set of orbitals belonging to a given principal quantum number n . They are labeled as K, L, M, \dots for $n = 1, 2, 3, \dots$, respectively,
- electron subshell: set of orbitals belonging to a given n and have an angular quantum number $L \in [0; n - 1]$,
- Unsöld's theorem: the square of the total electron wavefunction, i.e., probability density, for a filled or half-filled subshell is spherically symmetric.

The direct consequence of the Unsöld theorem, as shown in Sec. 2.1.2, lies in the fact that those subshells that are in agreement with the theorem do not contribute to the total angular momentum of the atom.

2.1.1 Angular momenta in many-electron atoms

The total orbital angular momentum \hat{L} and the total spin angular momentum \hat{S} of N_e electrons in an atom is defined as:

$$\hat{L} = \sum_{i=1}^{N_e} \hat{L}_i \quad \wedge \quad \hat{S} = \sum_{i=1}^{N_e} \hat{S}_i \quad (2.9)$$

Neglecting the spin-orbit coupling, the operators \hat{L} and \hat{S} commute with the atomic Hamiltonian (2.2) making possible the characterization of an atomic state by the quantum numbers L and S . Therefore, the electronic wave function of an atom satisfies:

$$\hat{L}^2 \psi = L(L+1)\hbar^2 \psi \quad \wedge \quad \hat{S}^2 \psi = S(S+1)\hbar^2 \psi \quad (2.10)$$

where $L(L+1)\hbar^2$ and $S(S+1)\hbar^2$ give the square of the magnitude of the total orbital and spin angular momentum, respectively. A code letter is widely used to specify the total orbital angular momentum quantum number:

L	0	1	2	3	4	5	6	7	8
letter	S	P	D	F	G	H	I	K	L

Based on the Pauli principle those subshells that are fully filled do not contribute to the total electronic spin angular momentum. When the spin-orbit interaction is taken into account, the operator \hat{L} does not commute with the Hamiltonian. Therefore, the total electronic angular momentum \hat{J} of an atom is introduced, such that:

$$\hat{J} = \hat{L} + \hat{S} \quad (2.11)$$

This type of coupling is known as *Russell-Saunders coupling* or LS coupling [23]. The operator \hat{J} commutes with the Hamiltonian, in consequence, the atomic state can be described by the quantum number J , having the possible values:

$$|L - S| \leq J \leq |L + S| \quad (2.12)$$

In addition,

$$\hat{J}^2 \psi = J(J + 1)\hbar^2 \psi \quad (2.13)$$

2.1.2 Atomic levels of the tin atom

The previously discussed theory helps at the understanding of the atomic lines of the tin atom studied in this thesis. The eigenvalues and eigenfunctions of the hydrogen-like Hamiltonian, \hat{H}_0 in (2.2), give all the possible *electron configurations* for the fifty electrons of tin, two of which are used in this thesis for studying its nuclear structure, see Fig. 2.1,

1. $[Kr] 4d^{10} 5s^2 5p^2$
2. $[Kr] 4d^{10} 5s^2 5p 6s$

When the electron correlations, \hat{H}_{rep} in (2.2), are included, different *atomic terms* appear for each electronic configuration, see Fig. 2.1. Those states can have the same or different energies depending on whether the interelectronic repulsions are the same or different. According to the Unsöld's theorem, only the two electrons at the $5p$ subshell, in the first electronic configuration, and the isolated electrons at the $5p$ and $6s$ subshells, in the second electronic configuration, are responsible for the total electronic orbital angular momentum in each level. In the first case and following the algebra of the total angular momentum, three values of L are possible, $L_1 \in \{0, 1, 2\}$ while for the second

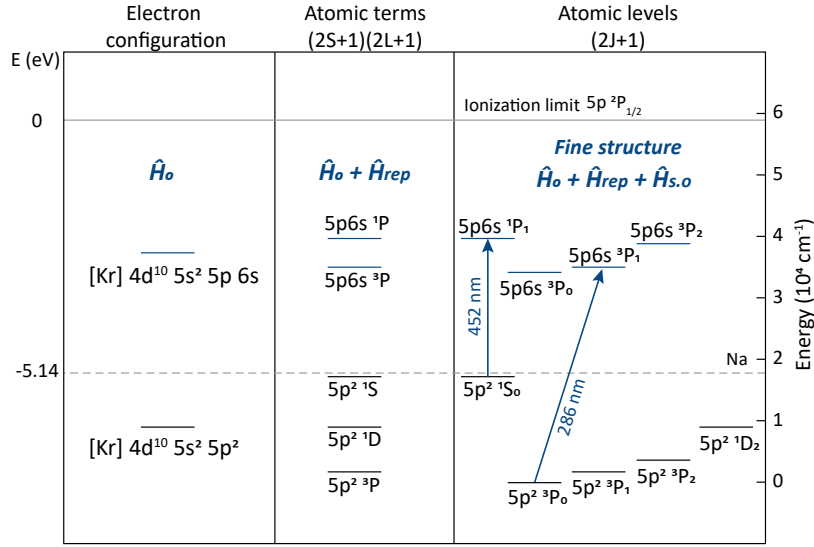


Figure 2.1: Relevant part of the electron configuration (first column), the atomic terms (second column) and the atomic levels scheme of Sn I. The resonant charge exchange level with Na is given as a dashed line, for further discussion in Ch. 4.

case L can take the single value $L_2 \in \{1\}$. We have to note that the subshell $6s$ has zero contribution to the angular momentum. The total spin angular momentum can be $S_{1,2} \in \{0, 1\}$ in both electronic configurations. Only the electrons in the open subshells contribute to it.

By including the relativistic spin-orbit interaction, $\hat{H}_{S,O}$ in (2.2), the *atomic levels* arise, see Fig. 2.1. The spectroscopic notation $n^{2S+1}L_J$ is being used.

1. $5p^2^3 P_0$ (1), $5p^2^3 P_1$ (3), $5p^2^3 P_2$ (5)
 $5p^2^1 D_2$ (5)
 $5p^2^1 S_0$ (1)
2. $5p6s^3 P_0$ (1), $5p6s^3 P_1$ (3), $5p6s^3 P_2$ (5)
 $5p6s^1 P_1$ (3).

Each atomic level consists of $2J + 1$ states of equal energy. The $(2J + 1)$ -fold degeneracy is highlighted in parenthesis in the previous items. It is related to the $2J + 1$ values of M_J where $M_J \hbar$ is the z component of the total electronic angular momentum \vec{J} .

The two atomic transitions highlighted in Fig. 2.1 are studied in this thesis to measure the nuclear properties of the tin isotopes.

2.2 Nuclear Hamiltonian

In the previous section, the nucleus was treated as a point of mass M and charge Ze . Further to this subtle approximation, the nucleus is a complex many-body system composed of $A = N + Z$ nucleons being Z the number of protons and N the number of neutrons. The nature of the interactions that keep the nucleons together in a limited region of the space can be found in the field of quantum chromodynamics [24,25]. This theory is well-beyond this thesis; nevertheless, some properties of the nucleus will be discussed.

The nuclear Hamiltonian can be written as:

$$\hat{H}_{\text{nuc}} = - \sum_{i=1}^A \frac{\hbar^2}{2m_i} \nabla_{\vec{r}_i}^2 + \sum_{j=1}^A \sum_{j>i}^A \hat{V}_{\text{nuc}}(|\vec{r}_i - \vec{r}_j|) + \sum_{j=1}^Z \sum_{j>i}^Z \frac{e^2}{|\vec{r}_i - \vec{r}_j|} + \sum_{j=1}^A \hat{H}_{s.o.}^j \quad (2.14)$$

where \vec{r}_i is the *position vector* of the i th-nucleon and m_i its mass.

The first term addresses the kinetic energy of the nucleons while the second one accounts for the nuclear interaction between them. The latter can be considered, in a first approximation, as a two-body interaction type: proton-proton ($\pi\pi$), neutron-neutron ($\nu\nu$), and proton-neutron ($\pi\nu$). The third term takes into account the Coulomb repulsion between the protons while the last term represents the relativistic spin-orbit interaction of the nucleons [26].

Two main differences between the atomic and nuclear Hamiltonian are significant:

- in the nuclear Hamiltonian, there is not an external potential as in the atomic one, where the nuclear charge creates a robust central potential for each electron;
- the spin-orbit interaction term has an electromagnetic origin for the elec-

trons, however, there is no similar origin for the same term for nucleons.

Aside from these differences, experimental evidence suggests a nuclear shell structure for nucleons [27,28] similar to the electronic shell structure observed for electrons. The Hamiltonian (2.14) can be rewritten as:

$$\hat{H}_{\text{nuc}} = \sum_{j=1}^N \hat{H}_j^\nu + \sum_{k=1}^Z \hat{H}_k^\pi + \sum_{j=1}^A \hat{H}_{s.o.}^j \quad (2.15)$$

where the one-particle Hamiltonians \hat{H}_j^ν for neutrons and \hat{H}_k^π for protons have the following explicit form:

$$\hat{H}_j^\nu = -\frac{\hbar^2}{2m_\nu} \nabla_{\vec{r}_j}^2 + \sum_{j>i}^A \hat{V}_{\text{nuc}}(|\vec{r}_i - \vec{r}_j|) \quad (2.16)$$

$$\hat{H}_k^\pi = -\frac{\hbar^2}{2m_\pi} \nabla_{\vec{r}_k}^2 + \sum_{j>k}^A \hat{V}_{\text{nuc}}(|\vec{r}_k - \vec{r}_j|) + \sum_{j>k}^Z \frac{e^2}{|\vec{r}_k - \vec{r}_j|} \quad (2.17)$$

being m_π and m_ν are the proton and neutron masses [29], respectively.

The spin-orbit interaction term for nucleons can be expressed as:

$$\hat{H}_{s.o.}^j = \frac{1}{\hbar^2} \hat{V}_{s.o.}(r) \hat{\ell}_j \cdot \hat{s}_j \quad (2.18)$$

where $\hat{\ell}_j$ and \hat{s}_j are the orbital and spin angular momenta of the j th-nucleon, respectively. The potential $\hat{V}_{s.o.}(r)$ is derived from the electron movement around the nucleus and its form and strength are determined phenomenologically.

The obtention of the eigenvalues and the eigenfunctions of the Hamiltonian (2.15) is extremely difficult and often impossible. Only small systems, like the deuteron to cite an example, are feasible. The most common approximation is the “*mean field theory*” widely used to treat many-body problems. The latter is also known as “*self-consistent field theory*” analogous to the Hartree-Fock method for the electrons. The fundamental principle of this theory lies in counting all the interactions to any one-body with an average or effective potential [30,31]. As a result, any multi-body system is treated as an effective

one-body problem. More specifically, it considers only the Hamiltonians \hat{H}_j^ν and \hat{H}_j^π , that describe a single nucleon subjected to a potential $\hat{V}_{\text{nuc}}^j(r_j)$ for a neutron or $\hat{V}_{\text{eff}}^j = \hat{V}_{\text{nuc}}^j(r_j) + \hat{V}_{\text{coul}}^j(r_j)$ for a proton. These potentials are the mean field created by all the other nucleons that interact with the j th-nucleon. The spin-orbit coupling is assumed as a single particle term. In other words, after the mean field approximation, the Hamiltonian for the j th-nucleon adopts the following form:

$$\hat{H}_{\text{nuc}}^j = -\frac{\hbar^2}{2m_j} \nabla_{\vec{r}_j}^2 + \hat{V}_{\text{eff}}^j + \frac{1}{\hbar^2} V_{\text{s.o.}}(r) \hat{\ell}_j \cdot \hat{s}_j \quad (2.19)$$

where the j th-nucleon can be a proton or a neutron. Therefore, the mean field potential can be expressed as:

$$\hat{V}_{\text{eff}}^j(r_j) = \begin{cases} \hat{V}_{\text{nuc}}^j(r_j) & \text{for neutrons} \\ \hat{V}_{\text{nuc}}^j(r_j) + \hat{V}_{\text{coul}}^j(r_j) & \text{for protons} \end{cases}$$

A new problem is glimpsed that lies in how to estimate the nuclear mean field interaction $\hat{V}_{\text{nuc}}^j(r_j)$. One of the most straightforward and successful potential wells is the Woods-Saxon potential [32]. It is an intermediate between the harmonic oscillator and the infinite well potential, having the following analytical form:

$$\hat{V}_{\text{nuc}}^j(r_j) = \frac{-V_0}{1 + \exp\left(\frac{r_j - R_{1/2}}{a}\right)} \quad (2.20)$$

where $R_{1/2}$ and a give a realistic description of the nuclear interaction. The first one is the radius for which the nuclear interaction reaches half of its starting value. The second one is related to the *skin thickness* parameter t through the expression: $a \approx t/(4 \ln 3)$, where t is defined as the distance at which the nuclear interaction drops from 90% of its starting value down to 10%. The experiments suggest that $t \approx 2.3$ fm, i.e., $a \approx 0.524$ fm for most nuclei. The well-depth V_0 is around 50 MeV, and it is optimized to give the proper separation energy of nuclear states. In Fig. 2.2, $\hat{V}_{\text{eff}}^j(r_j)$ for the j th-nucleon is sketched.

By using (2.20), the nuclear shell structure is obtained through the eigenvalues of the time-independent nuclear Hamiltonian (2.19). Two shell structures

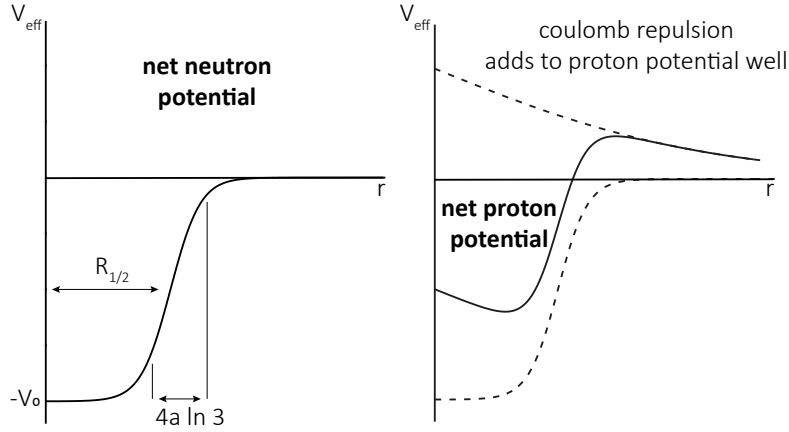


Figure 2.2: Woods-Saxon potential for the nuclear effective interaction.

completely independent can be considered; one for the neutrons and one for the protons. They have a similar order but slightly shifted in energy due to Coulomb repulsion. This simplified shell model can explain the nuclear “magic numbers.” In addition, ground state nuclear properties such that spin, parity and electromagnetic moments can be predicted.

2.2.1 Nuclear spin and parity

Similar to the total angular momentum \hat{J} for the electrons in the atom, a given nuclear state has associated a total angular momentum \hat{I} . The latter involves the orbital and intrinsic angular momentum of A -nucleons and can be defined as:

$$\hat{I} = \sum_{i=1}^A (\hat{\ell}_i + \hat{s}_i) \quad (2.21)$$

As a matter of convenience \hat{I} can be expressed in terms of the total angular momentum of the i th-nucleon \hat{j}_i (jj -coupling) or in terms of the total spin \hat{s} and orbital momentum $\hat{\ell}$ of A -nucleons (ls -coupling)

$$\hat{I} = \sum_{i=1}^A \hat{j}_i \quad \vee \quad \hat{I} = \hat{\ell} + \hat{s} \quad (2.22)$$

Therefore, each nuclear state is assigned a unique spin quantum number I . In the extreme single particle picture, depending on the number of protons and neutrons (odd or even) several rules can be followed for its determination:

- even-even nuclei: all nucleons are coupled pairwise ($\pi\pi$ and $\nu\nu$) to zero spin $I = 0$,
- odd-even nuclei: the total spin is determined by the j -value of the unpaired particle ($\pi \vee \nu$) while the remaining $(A - 1)$ nucleons are coupled to spin zero,
- odd-odd nuclei: the total spin is determined by the vector coupling of the \hat{j} of the unpaired neutron and proton, $\hat{I} = \hat{j}_\pi + \hat{j}_\nu$, taking values between $|j_\pi - j_\nu| \leq I \leq |j_\pi + j_\nu|$.

The parity of the nucleus, defined as the parity of the nuclear wavefunction, is given by the unpaired nucleon(s) and can be expressed as the product of the single nucleon parity $(-1)^\ell$.

2.2.2 Nuclear magnetic dipole moment

An operational definition of the nuclear magnetic dipole moment $\hat{\mu}$ associated to a total nuclear angular momentum \hat{I} can be expressed as:

$$\hat{\mu} = \sum_{i=1}^A \left(g_{\ell,\pi\nu\nu} \cdot \hat{\ell}_i + g_{s,\pi\nu\nu} \cdot \hat{s}_i \right) \quad (2.23)$$

where $g_{\ell,\pi\nu\nu}$ and $g_{s,\pi\nu\nu}$ are the *orbital* and *spin* angular momentum g factors, respectively. For protons, $g_{\ell,\pi} = 1$ while for neutrons $g_{\ell,\nu} = 0$. The spin g factors have the following values $g_{s,\pi} = 5.585694713(46)$ for protons and $g_{s,\nu} = -3.82608545(90)$ for neutrons [29]. They can be obtained by solving the relativistic Dirac equation for a point particle with spin 1/2.

In the single particle approximation, the expectation value of the operator

(2.23), well known as the *Schmidt moments*, has the following form:

$$\langle \hat{\mu} \rangle_{\pi\nu\nu}^{\text{S.P.}}(j) = \begin{cases} [(j - \frac{1}{2})g_{\ell,\pi\nu\nu} + \frac{1}{2}g_{s,\pi\nu\nu}] \mu_N & \text{for } j = \ell + \frac{1}{2} \\ \frac{j}{j+1} [(j + \frac{3}{2})g_{\ell,\pi\nu\nu} - \frac{1}{2}g_{s,\pi\nu\nu}] \mu_N & \text{for } j = \ell - \frac{1}{2} \end{cases}$$

where μ_N is the *nuclear magneton* ($\mu_N = e\hbar/2m_\pi \approx 3 \cdot 10^{-8} \text{eV/T}$) [29]. Based on this approximation, the ground states properties of odd-mass nuclei are characterized by the last unpaired nucleon; however, the experiments show that those nuclei that have nuclear magnetic moments deviate from the Schmidt values such that:

$$\mu_{\text{exp}} \approx [0.5; 1.5] \cdot \langle \hat{\mu} \rangle_{\pi\nu\nu}^{\text{S.P.}}(j) \quad (2.24)$$

The latter suggests that the interaction among all the nucleons should be taken into account. In order to correct this deviation, effective g factors should be used. They are defined as those values g_s^{eff} and g_ℓ^{eff} that minimize the differences between the experimental and the Schmidt values. Typical values are, $g_s^{\text{eff}} \sim 0.7g_{s,\pi\nu\nu}$ and $g_\ell^{\text{eff}} \sim g_{\ell,\pi\nu\nu}$ [33].

In terms of the nuclear spin \hat{I} , the magnetic moment can be written as:

$$\hat{\mu}_I = g_I \hat{I} \mu_N \quad (2.25)$$

where g_I is the *gyromagnetic ratio*.

2.2.3 Nuclear electric quadrupole moment

Most of the nuclei found in life have a non-spherical nuclear charge distribution, giving rise to a nuclear electric quadrupole moment. The quadrupole moment operator in a Cartesian coordinate system is defined [34] as:

$$\hat{Q}_{zz} = \sum_{i=1}^A e_{\pi\nu\nu} (3z_i^2 - r_i^2) \quad (2.26)$$

where $e_{\pi\nu\nu}$ are the free-nucleon charges with the values, $e_\pi = e$ and $e_\nu = 0$ and (z_i, r_i) the position coordinates of the i th-nucleon.

In a spherical coordinate system, it can be expressed as:

$$\hat{Q}_{zz} = \sqrt{\frac{16\pi}{5}} \sum_{i=1}^A e_{\pi\nu\nu} r_i^2 Y_2^0(\theta_i, \varphi_i) \quad (2.27)$$

where $Y_2^0(\theta_i, \varphi_i)$ is the zero-order second spherical harmonic.

The experimentally observed nuclear quadrupole moment, called spectroscopic nuclear quadrupole moment Q_S , is the expectation value of \hat{Q}_{zz} for a nuclear state with $m = I$. It is obtained by applying the Wigner-Eckart theorem [35] in terms of the reduced matrix element,

$$Q_S = \begin{pmatrix} I & 2 & I \\ -I & 0 & I \end{pmatrix} \sqrt{\frac{16\pi}{5}} \langle I || \sum_{i=1}^A e_{\pi\nu\nu} r_i^2 Y_2^0(\theta_i, \varphi_i) || I \rangle$$

Expanding the $3j$ -symbols and assigning the intrinsic nuclear quadrupole moment to the latest term, the expression can be rewritten as:

$$Q_S = \sqrt{\frac{I(2I-1)}{(I+1)(2I+3)}} Q_0 \quad (2.28)$$

Expression (2.28) shows that for a nuclear spin $I \in \{0, 1/2\}$, the spectroscopic quadrupole moment is identically zero, whatever value Q_0 is. It means that those nuclei with spin $I = 0$ or $I = 1/2$ may possess an intrinsic quadrupole deformation due to a non-zero reduced matrix element; nevertheless, its nuclear quadrupole moment cannot be measured experimentally. Two different approaches are conventionally used to estimate the spectroscopic quadrupole moment of a given nucleus:

- extreme single particle model: those nuclei with properties which can be defined by the unpaired proton or neutron in the j -orbital, the quadrupole moment can be calculated as the expectation value of (2.27) such that

$$\langle \hat{Q}_{zz} \rangle_{\pi\nu\nu}^{\text{S.P.}}(j) = -e_{\pi\nu\nu} \cdot \frac{2j-1}{2(j+1)} \cdot \langle r_j^2 \rangle_{\pi\nu\nu} \quad (2.29)$$

where $\langle r_j^2 \rangle_{\pi\nu\nu}$ is the mean square radius of the nucleon in that orbital.

Due to the interaction of the valence nucleons with the core, the elec-

tric quadrupole moment can strongly deviate from this expression. An example, discussed in this thesis, is the double magic plus one neutron nucleus ^{133}Sn , for which according to equation (2.29), the quadrupole moment should be zero, which is not the case, see Ch. 4.

The valence neutrons and/or valence protons can polarize the core resulting in small oblate or prolate shapes. Similar to the effective g factors, previously presented in Sec. 2.2.2, an empirical effective charge is introduced to take into account the core polarization effect,

$$Q_{\text{exp}} \approx \frac{e_{\pi\nu\nu}^{\text{eff}}}{e_{\pi\nu\nu}} \cdot \langle \hat{Q}_{zz} \rangle_{\pi\nu\nu}^{\text{S.P.}}(j) \quad (2.30)$$

Empirical effective charges have been obtained in several regions of the nuclear chart, where the expression (2.29) can be applied. They are found to be of the order of $e_{\pi}^{\text{eff}} \approx [1.3, 1.6]e$ and $e_{\nu}^{\text{eff}} \approx [0.1, 0.95]e$ [4].

- seniority scheme: those nuclei that contain n nucleons in a j -orbital with α nucleons unpaired (α is the seniority) and coupled to a spin I , the expectation values of (2.27), under the mean field approximation and using the angular momentum coupling rules, can be expressed [35] as

$$Q_n = \langle j^{n,\alpha} | \hat{Q}_{zz} | j^{n,\alpha} \rangle = \frac{2j+1-2n}{2j+1-2\alpha} \cdot \langle j^\alpha | \hat{Q}_{zz} | j^\alpha \rangle \quad (2.31)$$

The latter expression is called the quadrupole moment of multi-particle configurations. In the simplest case, where the seniority $\alpha = 1$ or “normal coupling” [1, 36], all but one particle are coupled to spin zero. Then, $\langle j | \hat{Q} | j \rangle = \langle \hat{Q}_{zz} \rangle_{\pi\nu\nu}^{\text{S.P.}}(j)$ and (2.31) shows a linear trend, between $-\langle \hat{Q}_{zz} \rangle_{\pi\nu\nu}^{\text{S.P.}}(j)$ and $\langle \hat{Q}_{zz} \rangle_{\pi\nu\nu}^{\text{S.P.}}(j)$, being zero at the middle of the shell.

Nuclear deformations

Far from the single-particle shell model, the breakdown of the single particle representation, the interaction between the valence nucleons and the core will lead to a non-spherical charge distribution. The experimental observations in those nuclei are better described under the assumption of the liquid drop model. It considers the motion of a charged liquid drop which may produce

small surface oscillation around the spherical equilibrium shape or it may rotate if the nucleus has a stable ground state deformation. In this scenario, the intrinsic quadrupole moment Q_0 can be linked to the deformation parameter β -charge deformation related to the proton charge distribution- for an axially deformed spheroid nucleus [37, 38]

$$Q_0 = eZ\sqrt{\frac{5}{\pi}}\langle r^2\rangle\langle\beta\rangle\left(1 + \frac{\langle\beta\rangle}{8}\sqrt{\frac{5}{\pi}}\right) \quad (2.32)$$

$$Q_S = \frac{3K^2 - I(I+1)}{(I+1)(2I+3)}Q_0 \quad (2.33)$$

where K is the projection of the total spin \hat{I} onto the symmetry axis of the deformed nucleus with a mean square charge radius $\langle r^2\rangle$. Two regions can be distinguished according to the sign of the beta parameter, e.g., $\beta > 0$ corresponds to a prolate shape and $\beta < 0$ to an oblate shape.

The mean square charge radius

The radial moments of a nuclear charge distribution are defined [39] as,

$$\langle r^n\rangle = \frac{\int \rho(r)r^n d^3r}{\int \rho(r)d^3r} \quad (2.34)$$

where the denominator is the total nuclear charge, Ze , being $\rho(r)$ the charge density of the protons in the nucleus. The mean square charge radius is obtained for $n = 2$.

For spherical nuclei, different functional forms are proposed for $\rho(r)$ in order to estimate (2.34).

- The liquid-drop model [40]: it assumes a uniform proton distribution over the nuclear volume, such that:

$$\rho(r)^{\text{L.D.}} = \frac{A}{\frac{4}{3}\pi R^3} \quad (2.35)$$

where the protons are distributed along the radius of the mass distribution, given as $R = R_0 A^{1/3}$. The experimental data indicate that

$R_0 \approx 1.2$ fm gives a reasonable approximation for the homogeneous nuclear charge distribution. Assuming this simple model, the expression (2.34), for $n = 2$ has the following expectation value:

$$\langle r^2 \rangle_{\text{sph}}^{\text{L.D.}} = \frac{3}{5} R_0^2 A^{2/3} \quad (2.36)$$

- The Fermi charge distribution [41]: it is commonly used to describe the nuclear charge density in those nuclei having finite surface thickness instead of uniform distribution. It has the same functional shape as a Woods-Saxon potential and gives a more physical representation of the nuclear structure

$$\rho(r) = \frac{\rho_0}{1 + \exp\left(\frac{r - R_{1/2}}{a}\right)} \quad (2.37)$$

where ρ_0 , called the central density, is the nuclear density at $r = 0$. The other parameters were previously introduced in (2.20), but now they are expressed concerning the nuclear density. The computation of the mean square charge radius using the Fermi distribution does not have an analytical solution. Instead of that, an approximation [42] is usually made :

$$\langle r^2 \rangle_{\text{sph}}^{\text{F.D.}} \approx \frac{3}{5} R_{1/2}^2 + \frac{7}{5} \pi a^2 \quad (2.38)$$

The mean square charge radius of a deformed nucleus [43] can be expressed by the mean square charge radius of a spherical nucleus $\langle r^2 \rangle_{\text{sph}}$ which has the same volume as the deformed one plus a term that depends on the quadrupole deformation parameter β

$$\langle r^2 \rangle = \langle r^2 \rangle_{\text{sph}} + \frac{5}{4\pi} \langle r^2 \rangle_{\text{sph}} \langle \beta^2 \rangle \quad (2.39)$$

2.3 Atomic hyperfine structure

As we have already seen, beyond the point-like assumption, a magnetic dipole and an electric quadrupole moment are associated with the nucleus with non-zero nuclear spin. The interaction of these moments with the field created by the electrons causes an additional splitting of the atomic levels, called

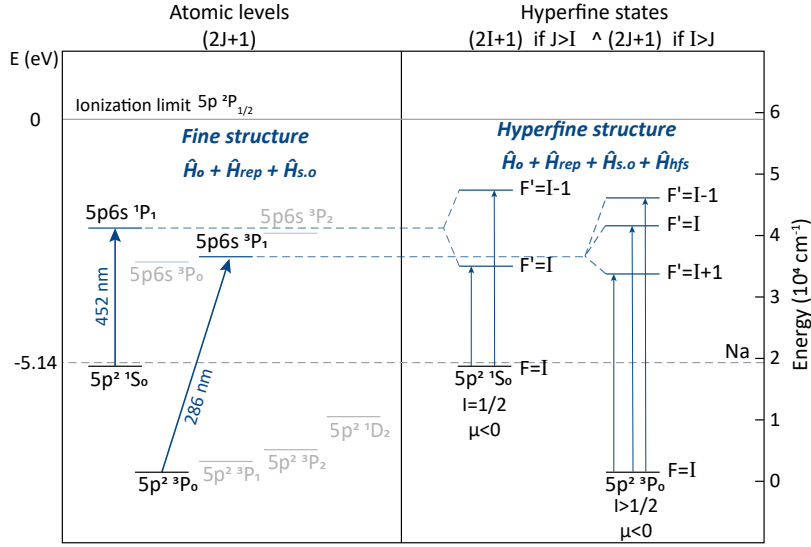


Figure 2.3: Relevant part of the atomic levels (first column) and hyperfine states (second columns) of Sn I. The resonant charge exchange level with Na is given as grey dashed line, for further discussion in Ch. 4. The allowed transitions between the hyperfine states for $I = 1/2$ and $I > 1/2$ ($\mu < 0$ in both cases) are included on the picture. Hyperfine energy levels are not to scale.

hyperfine structure (hfs), see Fig. 2.3, being the best-known example of nuclear structure effect. It arises from the coupling between the nuclear spin \hat{I} and the total angular momenta of the electrons \hat{J} giving place to the total angular momentum operator $\hat{F} = \hat{I} + \hat{J}$. From this coupling, the quantum number F is allowed to range from:

$$|I - J| \leq F \leq |I + J| \quad (2.40)$$

One hyperfine multiplet contains a number of states equal to $2I + 1$ for $J > I$ and $2J + 1$ for $I > J$. The hyperfine Hamiltonian that describes the additional energy splitting of the atomic levels depicted in Fig. 2.3 can be written considering two major contributions [44]:

$$\hat{H}_{\text{hfs}} = \hat{H}(M1) + \hat{H}(E2) + \dots \quad (2.41)$$

being $\hat{H}(M1)$ and $\hat{H}(E2)$ the *magnetic dipole* and *electric quadrupole interaction*, respectively. The allowed dipole transitions between different multiplets,

labeled as F and F' , are $\Delta F = 0, \pm 1$ with $F + F' \geq 1$. As additional conditions, transitions between the same multiplet are forbidden as well as transitions between levels of the same parity. The dipole transition strengths \mathcal{S} between the F and F' components, also known as Racah intensities [45], can be expressed by,

$$\mathcal{S}_{F \rightarrow F'} \propto (2F + 1)(2F' + 1) \left\{ \begin{matrix} J' & F' & I \\ F & J & 1 \end{matrix} \right\}^2 \quad (2.42)$$

2.3.1 Magnetic dipole interaction

The first term in (2.41) originates from the interaction of the magnetic field generated by the electrons, $\hat{\vec{B}}_J$, and the nuclear magnetic dipole moment, $\hat{\vec{\mu}}_I$. The Hamiltonian that accounts for this effect [46,47] can be written as:

$$\hat{H}(M1) = -\hat{\vec{\mu}}_I \cdot \hat{\vec{B}}_J = A \frac{\hat{\vec{I}} \cdot \hat{\vec{J}}}{\hbar^2} \quad (2.43)$$

where A is the *magnetic hyperfine* parameter. The nuclear magnetic moment $\hat{\vec{\mu}}_I$ was previously defined in (2.25) and by expressing $\hat{\vec{B}}_J$ in terms of the average magnetic field created at the position of the nucleus $B_J(0)$ [44], the A -hyperfine parameter can be expressed as

$$A = \frac{\mu_I B_J(0)}{IJ} \quad (2.44)$$

The previous equation implies that μ_I can be extracted from the measured hyperfine constant if $B_J(0)$ is known. This value is usually extracted from independent measurements on stable isotopes of the same element or estimated by atomic theories. Assuming that $B_J(0)$ is constant along the isotopic chain, neglecting hyperfine anomaly effects, the hyperfine parameters A of any two isotopes in the chain can be related through the expression:

$$A \frac{I}{\mu_I} = \text{const.} \quad (2.45)$$

The scalar product in (2.43) can be rewritten as:

$$\hat{I} \cdot \hat{J} = \frac{1}{2} [\hat{F}^2 - \hat{I}^2 - \hat{J}^2] \quad (2.46)$$

therefore, the contribution to the atomic energies, arising from the magnetic dipole interaction is:

$$\begin{aligned} E(M1) &= \frac{A}{2} [F(F+1) - I(I+1) - J(J+1)] \\ &\equiv \frac{A}{2} K \end{aligned} \quad (2.47)$$

2.3.2 Electric quadrupole interaction

The second term in (2.41) arises from the interaction between the nuclear quadrupole moment, due to a non-spherical charge distribution of the nucleus, and the electric field gradient generated by the electron cloud at the position of the nucleus, V_{zz} . The Hamiltonian that accounts for this interaction [46, 47] can be written as:

$$\hat{H}(E2) = \frac{h\nu_Q}{4I(2I-1)\hbar^2} [3\vec{I}_z^2 - \vec{I}^2 + \eta(\vec{I}_x^2 - \vec{I}_y^2)] \quad (2.48)$$

where

$$\nu_Q = \frac{eQV_{zz}}{h} \quad (2.49)$$

is known as *quadrupole frequency* and $\eta = (V_{xx} - V_{yy})/V_{zz}$ is called *asymmetry parameter* of the electric field gradient.

The electric quadrupole hyperfine splitting arising from the electric quadrupole interaction is:

$$E(E2) = B \frac{3K(K+1) - 4I(I+1)J(J+1)}{8I(2I-1)J(2J-1)} \quad (2.50)$$

where B is the *quadrupole hyperfine parameter* and is defined as

$$B = eQ V_{JJ}(0) \quad (2.51)$$

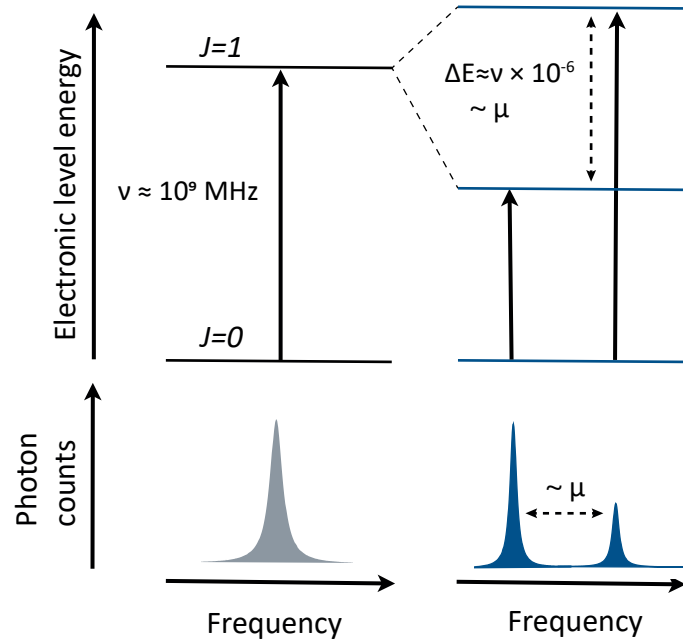


Figure 2.4: Size of the hyperfine splitting of the $5p6s\ ^3P_1$ electronic level for isotopes with $I = 1/2$ compared to the fine structure splitting. Adapted from [48].

being $V_{JJ}(0)$ the average electric field gradient at the nucleus induced by the electrons having cylindrical symmetry about the J axis. The hyperfine parameter B of any two isotopes can be related through the expression:

$$\frac{B}{Q} = \text{const.} \quad (2.52)$$

The hyperfine splitting of the $5p6s\ ^3P_1$ electronic level for isotopes with $I = 1/2$ is depicted in Fig. 2.4. The size of the hyperfine splitting, due to magnetic splitting because there is no quadrupole splitting in this case, is 10^{-6} the size of the fine structure splitting.

2.3.3 Isotope shift

The first direct effect of the shape and size of a nucleus into the fine-electronic structure is the isotope shift (IS). It is defined as the differences in energy of a spectral line i [49] for two isotopes (A, A'),

$$\delta\nu_i^{AA'} = \nu_i^{A'} - \nu_i^A \quad (2.53)$$

where A' and A are the mass numbers of the two isotopes. Two complementary transitions are studied in this thesis, $i : 5p^2 \ ^1S_0 \rightarrow 5p6s \ ^1P_1$ and $j : 5p^2 \ ^3P_0 \rightarrow 5p6s \ ^3P_1$, see Fig. 2.3.

The isotope shift in (2.53) can be split into two components, the *mass shift* ($\delta\nu_{i,MS}^{AA'}$) and the *field shift* ($\delta\nu_{i,FS}^{AA'}$),

$$\delta\nu_i^{AA'} = \delta\nu_{i,MS}^{AA'} + \delta\nu_{i,FS}^{AA'} \quad (2.54)$$

From one isotope to the other, the mass of the atomic nucleus is slightly modified while the angular momentum has to remain the same, therefore, the energy of the level changes. This shift in energy is one of the main parts of the isotope shift and correspond to the first term in (2.54). The second term arises because of the dependence of the atomic level upon the size and shape of the electric charge distribution of the nucleus. From one isotope to the other, the number of protons is the same, but its distribution in space is different due to the influence of the number of neutrons.

For light nuclei, the mass shift dominate the field shift while for heavy nuclei the field shift becomes predominant, See Fig. 2.5

Mass shift

The mass shift term can be further presented as a sum of two contributions: the normal mass shift (NMS) and the specific mass shift (SMS).

$$\delta\nu_{i,MS}^{AA'} = \delta\nu_{i,NMS}^{AA'} + \delta\nu_{i,SMS}^{AA'} \quad (2.55)$$

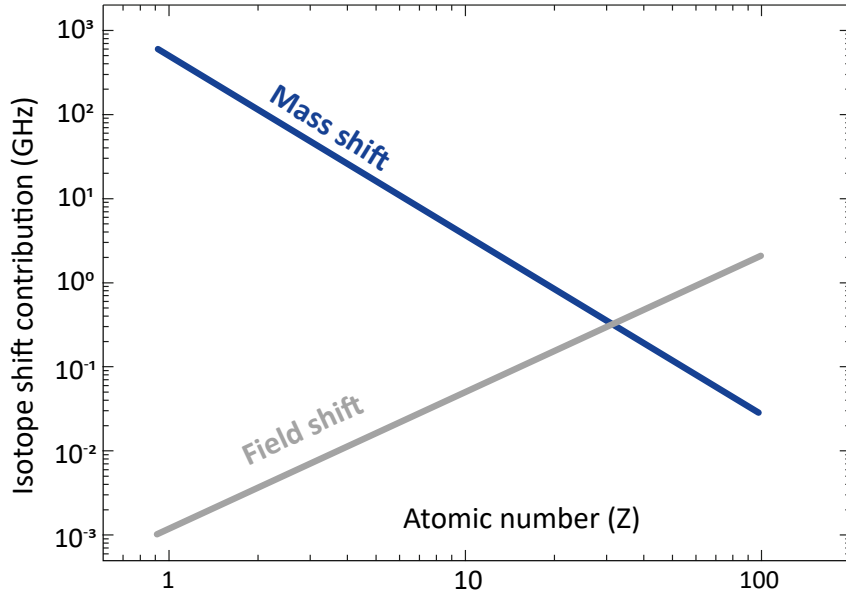


Figure 2.5: Mass and field shift contribution as a function of the atomic number Z . Adapted from [50].

The first term accounts for the effect of the reduced mass correlation of the electron-nucleus system on the fine transition frequency and can be expressed as:

$$\delta\nu_{i,NMS}^{AA'} = K_{i,NMS} \frac{m_{A'} - m_A}{m_{A'} m_A} \quad (2.56)$$

where $K_{i,NMS}$ is called the *normal mass shift constant* and its value is $\nu_i m_e$, being ν_i the frequency of the i fine transition and m_e the mass of the electron. The second term in (2.55) takes into account a small effect due to the electronic correlation changes from isotope to isotope into the frequency of the fine transition. It can be expressed as:

$$\delta\nu_{i,SMS}^{AA'} = K_{i,SMS} \frac{m_{A'} - m_A}{m_{A'} m_A} \quad (2.57)$$

where $K_{i,SMS}$ is known as *specific mass shift constant*.

Inserting (2.56) and (2.57) into (2.55), one can get the mass shift as a function

of the mass shift constants, $K_i = K_{i,NMS} + K_{i,SMS}$, such that:

$$\delta\nu_{i,MS}^{AA'} = K_i \frac{m_{A'} - m_A}{m_{A'} m_A} \quad (2.58)$$

Field shift

The field shift is commonly expressed as:

$$\delta\nu_{i,FS}^{AA'} = F_i \cdot \lambda^{AA'} \quad (2.59)$$

where the quantity F_i is known as *electronic factor*. It is proportional to the variation of the electronic charge at the nucleus for a given i fine structure transition. The nuclear parameter $\lambda^{AA'}$, can be expanded as:

$$\lambda^{AA'} = \sum_{n=1}^{\infty} \frac{C_n}{C_1} \delta \langle r^{2n} \rangle^{AA'}, \quad (2.60)$$

where $\delta \langle r^{2n} \rangle^{AA'} = \langle r^{2n} \rangle^{A'} - \langle r^{2n} \rangle^A$ is the difference in the even-radial moments between two isotopes, see (2.34). The coefficients C_n are tabulated in [51] for $30 \leq Z \leq 103$. To a good approximation, the first term in (2.60) can be considered,

$$\delta\nu_{i,FS}^{AA'} = F_i \cdot \delta \langle r^2 \rangle^{AA'}. \quad (2.61)$$

The isotope shift can be linked to the differences between nuclear mean square charge radii through the following expression:

$$\delta\nu_i^{AA'} = K_i \frac{m_{A'} - m_A}{m_{A'} m_A} + F_i \cdot \delta \langle r^2 \rangle^{AA'} \quad (2.62)$$

One can see from this expression that by measuring the isotope shift of an optical spectral line, and knowing the electronic factors K_i and F_i , information on isotopic differences between nuclear mean square charge radii can be extracted. The values of K_i and F_i can be obtained by theoretical calculations or through a common approach based on the fact that these two quantities are not isotope dependent. For that, (2.62) is rewritten in the following way

$$\delta\nu_{i,\text{mod}}^{AA'} = K_i + F_i \cdot \delta \langle r^2 \rangle_{\text{mod}}^{AA'} \quad (2.63)$$

where

$$\delta\nu_{i,\text{mod}}^{AA'} = \delta\nu_i^{AA'} \cdot \frac{m_{A'}m_A}{m_{A'} - m_A} \quad \wedge \quad \langle r^2 \rangle_{\text{mod}}^{AA'} = \langle r^2 \rangle^{AA'} \cdot \frac{m_{A'}m_A}{m_{A'} - m_A} \quad (2.64)$$

By plotting (2.63) using the IS of stables isotopes with known mean square charge radii, usually from muonic data, one can get the information about the electronic factors which are then used for the radioactive cases.

King plots

The King plot method has been widely used to extract information on the electronic factors using isotopes with known mean square charge radii. The method can be applied when a single fine electronic transition is studied, and the accuracy of the extracted constants can be improved if the same isotopes are measured in two different transitions (i, j) .

- The King plot when a single fine-electronic transition is studied.

Knowing in advance changes in mean charge radius from another experimental data, usually from muonic data and for stables isotopes, one can plot $\delta\nu_{i,\text{mod}}^{AA'}$ obtained from the experiment as a function of $\langle r^2 \rangle_{\text{mod}}^{AA'}$ using (2.63). By a linear regression, one can obtain the F_i parameter from the slope and the K_i factor from the intercept with the y -axis.

- The King plot when two fine electronic transitions are studied.

Considering two fine-electronic transition (i, j) :

$$i : \quad \delta\nu_{i,\text{mod}}^{AA'} = K_i + F_i \cdot \delta \langle r^2 \rangle_{\text{mod}}^{AA'}$$

$$j : \quad \delta\nu_{j,\text{mod}}^{AA'} = K_j + F_j \cdot \delta \langle r^2 \rangle_{\text{mod}}^{AA'}$$

one can eliminate $\langle r^2 \rangle_{\text{mod}}^{AA'}$ and get a linear regression, such that:

$$\delta\nu_{i,\text{mod}}^{AA'} = \frac{F_i}{F_j} \cdot \delta\nu_{j,\text{mod}}^{AA'} + K_i - \frac{F_i}{F_j} K_j \quad (2.65)$$

where the slope (α) and the y -intercept (β) are:

$$\alpha = \frac{F_i}{F_j} \quad \wedge \quad \beta = K_i - \frac{F_i}{F_j} K_j \quad (2.66)$$

consequently, α and β can be obtained through a linear fit of (2.65). A plot of data according to (2.65) does not depend on $\langle r^2 \rangle_{\text{mod}}^{AA'}$; therefore, all the measured isotopes can be used in the plot and as a result, the accuracy of the extracted electronic factors is improved.

A self-consistent King plot analysis is carried out in this thesis to extract the isotopic differences between nuclear mean square charge radii along the tin chain, see Ch. 4.

Chapter 3

Collinear laser spectroscopy

The farther the experiment is from theory, the closer it is to the Nobel Prize.

- Irene Joliot Curie -

3.1 The ISOLDE facility

The Isotope Separation OnLine DEvice, ISOLDE [52], is a radioactive beam facility dedicated to the production of a wide range of radioactive species via the ISOL method [53]. A layout of the facility located at the European Organization for Nuclear Research, CERN [54], is given in Fig. 3.1.

The neutron-rich tin isotopes are produced at ISOLDE-CERN by 1.4 GeV high energy protons impinging on a target/converter assembly [55]. The latter consisted of a tungsten rod coupled to a standard UC_x target. The arrangement has the purpose of suppressing the isobaric contamination, from spallation products mainly cesium, normally produced by direct bombardment of the target. The reaction products diffuse out of the target into the Resonance Ionisation Laser Ion Source, RILIS [56], to chemically select tin with typical yields according to [57]. Following electrostatic acceleration up to 40 or 50 keV and mass selection with the High-Resolution Separator (HRS) [58]. The ions are subsequently injected into the radio frequency quadrupole cooler and buncher, ISCOOL [59].

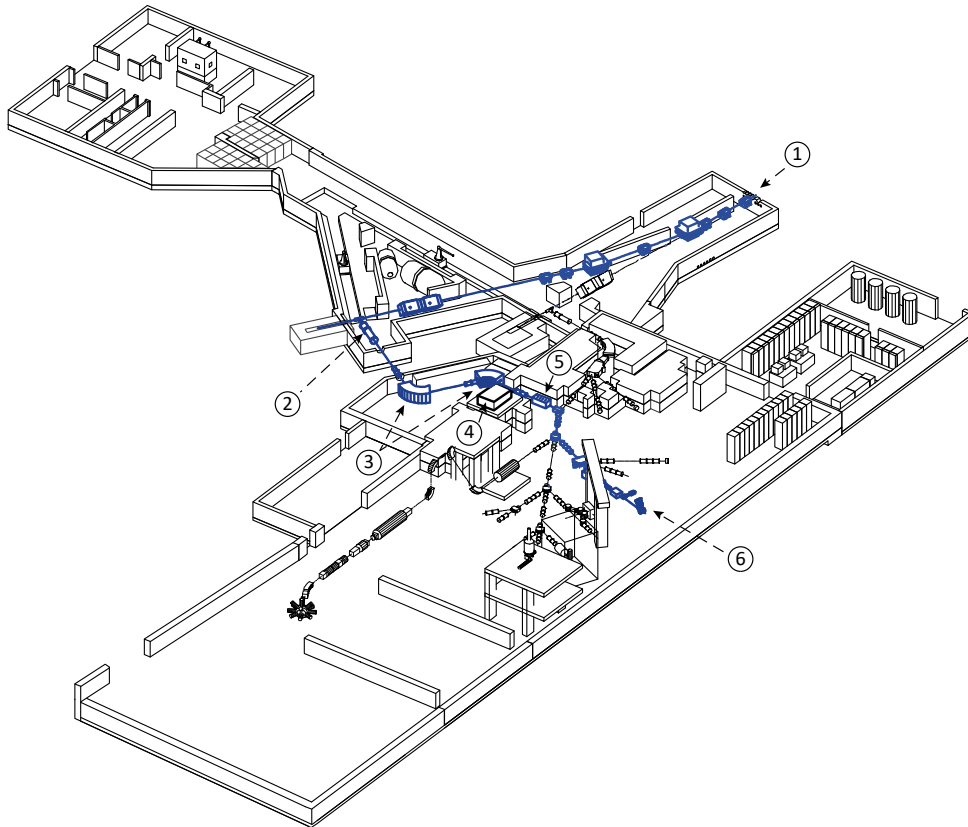


Figure 3.1: Layout of the ISOLDE facility. The beam path up to the laser spectroscopy experiment is highlighted. 1. Proton beam; 2. Target; 3. HRS; 4. RILIS; 5. ISCOOL; 6. COLLAPS. Adapted from [60].

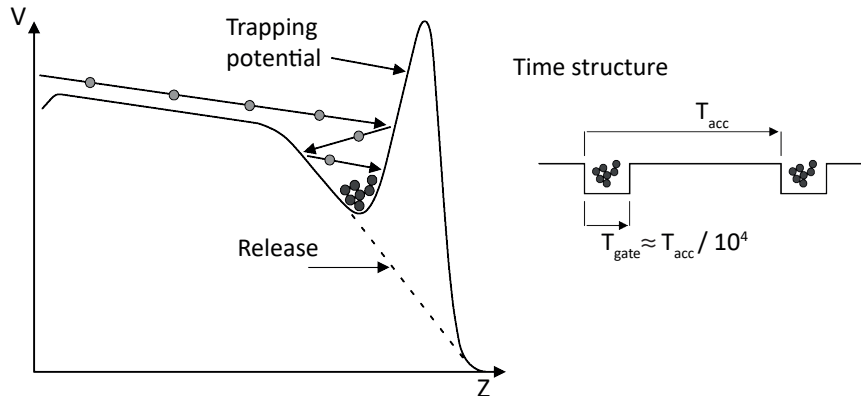


Figure 3.2: Diagram of the segmented radiofrequency quadrupole trap. The time structure of the resulting bunches is shown. Adapted from [59].

ISCOOL provides beams with a reduced transverse emittance, either continuously or in bunches with a well-defined temporal structure. Bunched beams were used, allowing synchronization of the optical detection system with the time window of the bunch. As a result, the background is reduced by a factor of $T_{\text{acc}}/T_{\text{gate}} \approx 10^4$ for a trap-accumulation time (T_{acc}) of 100 ms and a temporal bunch (T_{gate}) of 10 μs , see Fig. 3.2. The beam is ejected towards the collinear laser spectroscopy beamline (COLLAPS) shown in Fig. 3.3. Detailed information on the ISOLDE facility can be found elsewhere [61–63].

3.2 Experimental setup

A schematic representation of the COLLAPS beamline is sketched in Fig. 3.3. The incoming tin ions are overlapped with a linearly polarized laser beam via two electrostatic deflectors. Once the ions are in a collinear configuration with the laser beam, they reach the post-acceleration section for Doppler tuning. Subsequently, they enter a charge exchange cell to be neutralized through multiple collisions with sodium vapor [65]. At a precise laser frequency, the atomic electrons are resonantly excited, and during the de-excitation, the atoms fluoresce in the transition of their hyperfine structure. The fluorescence spectrum is detected with four photomultiplier tubes [66] as a function of the laser fre-

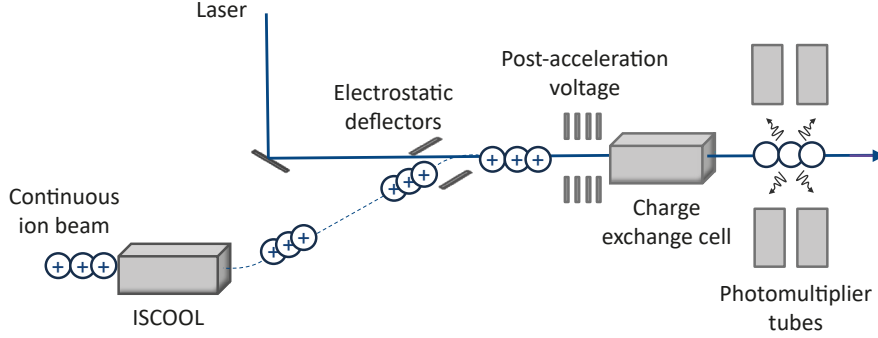


Figure 3.3: Sketch of the COLLAPS set-up at ISOLDE, CERN. Adapted from [64].

quency in the reference frame of the beam:

$$\nu = \nu_0 \sqrt{\frac{1 - \beta}{1 + \beta}}, \quad (3.1)$$

with

$$\beta = \frac{|\vec{v}|}{c} = \sqrt{1 - \left(\frac{mc^2}{eU_{\text{total}} + mc^2} \right)^2} \quad (3.2)$$

Here ν_0 is the laser frequency in the laboratory frame, m is the mass of the atom and U_{total} is the total acceleration voltage. The latter is applied to scan ν across the hyperfine range while keeping the laser fixed to ν_0 . It can be expressed as:

$$U_{\text{total}} = U_{\text{acc}} - (U_{\text{offset}} + k_{\text{kepco}} U_{\text{scan}}) \quad (3.3)$$

where U_{acc} is the voltage applied after the ISCOOL cooler/buncher, U_{offset} is an isotope-dependent voltage used to tune ν_0 close to the frequency of the transition under study and k is an amplification factor used to amplify the scanning voltage, U_{scan} .

Two independent experiments were carried out using transitions with complementary properties in the neutral atom, $5p^2\ ^1S_0 \rightarrow 5p6s\ ^1P_1$ and $5p^2\ ^3P_0 \rightarrow 5p6s\ ^3P_1$ at $\lambda = 452\ \text{nm}$ and $\lambda = 286\ \text{nm}$, respectively. The lower levels were populated in a quasi resonant charge exchange reaction with sodium, see Fig. 2.3. Optical detection of the $5p^2\ ^3P_0 \rightarrow 5p6s\ ^3P_1$ transition is based on the fluorescence at 286 nm, while the $5p^2\ ^1S_0 \rightarrow 5p6s\ ^1P_1$ transition is detected

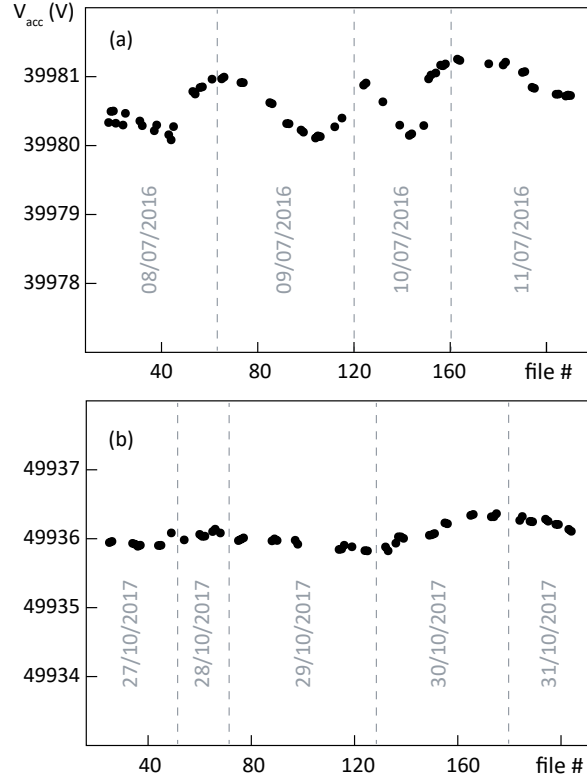


Figure 3.4: Stability of the voltage V_{acc} at ISCOOL during the study of the $5p^2\ ^1S_0 \rightarrow 5p6s\ ^1P_1$ transition (a) and $5p^2\ ^3P_0 \rightarrow 5p6s\ ^3P_1$ transition (b). Dashed lines delimit the different days of the experiment.

by the subsequent decay along the $5p6s\ ^1P_1 \rightarrow 5p^2\ ^1D_2$ transition at 326 nm which avoids optical pumping and acts as an efficient background suppression. In the upper states, the singlet offers high sensitivity to the quadrupole moment while the triplet facilitates a large magnetic splitting. It is worth noticing that in both cases the lower state does not have hyperfine splitting ($J = 0$).

3.2.1 Voltages read-out

The stability and precision of the voltages entering in (3.3) have a direct influence on the reliability of the parameters extracted from the analysis; therefore, the electronic devices are monitored during the experiment. The reading of

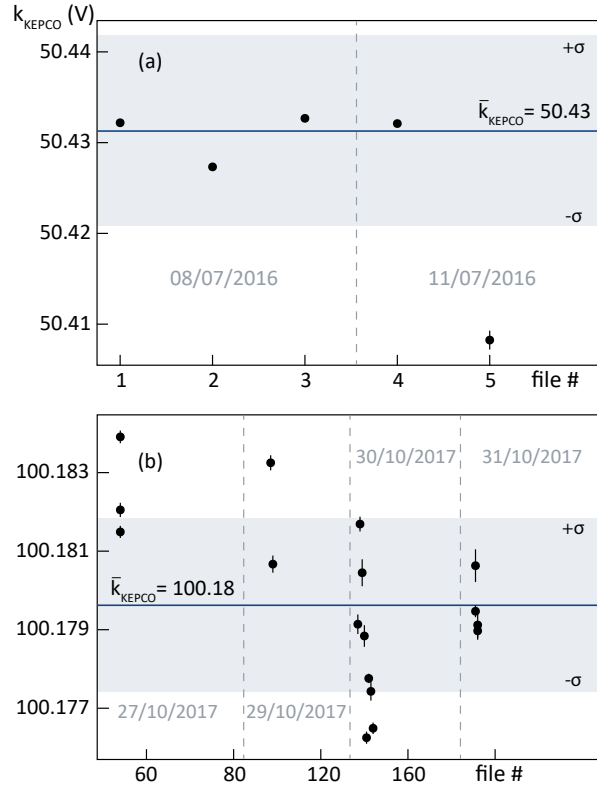


Figure 3.5: The amplification factor of the KEPCO linear voltage amplifier determined during the measurements in the $5p^2\ ^1S_0 \rightarrow 5p6s\ ^1P_1$ transition (a) and $5p^2\ ^3P_0 \rightarrow 5p6s\ ^3P_1$ transition (b). Dashed lines delimit different days of the experiment, and the horizontal solid blue line represents the weighted mean of all measurements. Grey bands enclose the 1σ confidence level for this value.

U_{acc} is done automatically along the scan of each isotope. A digital multimeter, Agilent 34461A, is used, coupled to a high-voltage divider ($1:10^4$). The values are recorded in the output file of the data acquisition system (Measurement and Control Program MCP). The U_{acc} remained stable during the measurements of the two studied transitions, see Fig. 3.4, with fluctuations smaller than the reported uncertainty for the divider (relative error of 10^{-4}). For each isotope, the averaged value of U_{acc} is determined from the individual read-out recorded in the data file.

The voltage of the post-acceleration part, U_{offset} , is measured at the COLLAPS beam line in a similar way to the one explained for U_{acc} . A Prema 6040 digital

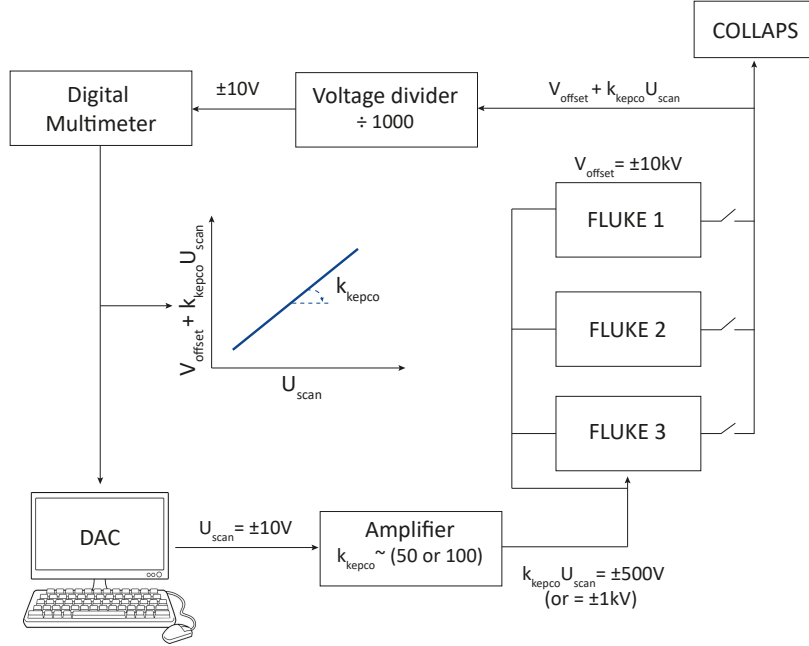


Figure 3.6: Block diagram of the data acquisition system. See the text for details.

multimeter coupled to a voltage divider ($1:10^3$) is employed. They are saved in the data file, and the averaged value is used for the analysis. Additionally, the post-acceleration voltage requires the calibration of the linear amplifier (Kepco). The calibration consists of the scanning of U_{scan} from -10V to $+10\text{V}$ while measuring the post-acceleration voltage applied to the beam line. This procedure is repeated for the three power supplies (Fluke). During the study of the $5p^2\ ^1S_0 \rightarrow 5p6s\ ^1P_1$ transition, the Kepco BOP 500DM high voltage power supply, which can be used to scan up to 500V , was used while during the study of the $5p^2\ ^3P_0 \rightarrow 5p6s\ ^3P_1$ transition it was replaced by the BOP 1000DM model, that extends the scan range up to 1 kV . A different high-voltage amplifier is justified by a seven times larger hyperfine splitting of the atomic state. A total of five ($5p^2\ ^1S_0 \rightarrow 5p6s\ ^1P_1$) and seventeen ($5p^2\ ^3P_0 \rightarrow 5p6s\ ^3P_1$) calibration measurements were recorded and afterward fitted with a linear function with slope k_{kepco} . The final values of $\bar{k}_{\text{kepco}} = 50.43(1)$ and $\bar{k}_{\text{kepco}} = 100.180(2)$, were determined as the weighted mean for all the individual measurements, see Fig. 3.5.

In Fig. 3.6 a simplified scheme of power supplies for the post-acceleration region and read-out electronics at COLLAPS is shown.

3.2.2 Laser system

A continuous wave (cw) $\text{Nd}^{3+}:\text{YVO}_4$ laser [67] is used to pump a Spectra-Physics Matisse laser, configured for Ti:Sa during the study of the singlet and dye during the study of the triplet, as the gain medium [68, 69]. The single-frequency cw beam out of the Matisse laser enters an external cavity (Wave Train [70]) where a second-harmonic is generated resulting in the desired wavelength.

The output beam of the Matisse laser was steadily measured with a HighFinesse WSU2 wavelength meter, calibrated with reference to a temperature-stabilized HeNe laser. The reference isotope was measured in a systematic way allowing us to detect any possible drift or instability of the laser.

3.3 Data collection

The hyperfine spectra are saved as data files that contain the number of fluorescent photons in each photomultiplier versus the scan voltage, U_{scan} in (3.3). For the analysis, the x -axis is transformed to frequency using the relativistic Doppler effect for a collinear configuration, represented by (3.1). The masses of the tin isotopes used for the conversion are taken from [71].

3.3.1 Lineshapes observation

Symmetric *Voigt profiles* are commonly used to describe experimental line shapes in collinear laser spectroscopy. Asymmetric resonances with small additional peak(s) or a tail on its low-frequency side have been observed when a neutralization process is involved [65]. These satellite peaks can be associated to charge-exchange processes or/and inelastic collisions with the vapour medium [72, 73]. Throughout the measurements, the experimental conditions were optimized to obtain nearly symmetric lineshapes which favor better accuracy of the fitting. A symmetric *Voigt profile* was considered the most

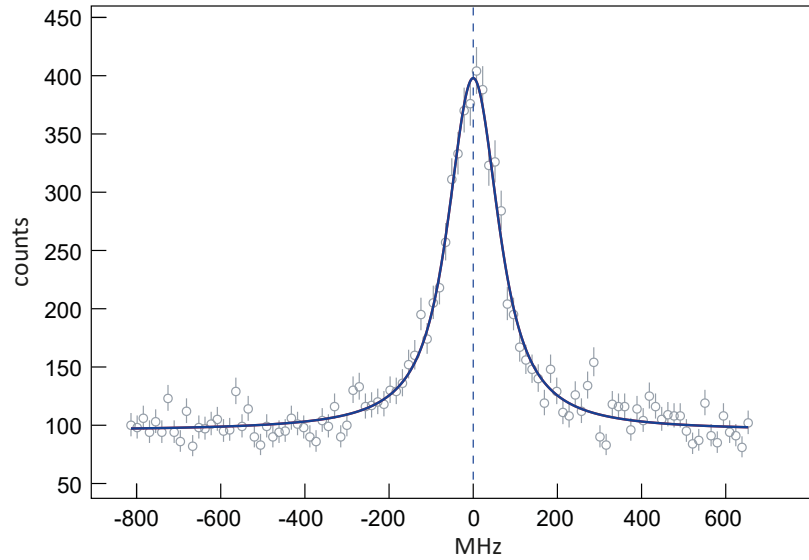


Figure 3.7: Measurement of the reference isotope ^{124}Sn recorded in the $5p^2\ ^3P_0 \rightarrow 5p6s\ ^3P_1$ transition. The solid blue line represents a fit with a symmetric *Voigt profile*. The reduced chi-square of the fitting is 1.3.

adequate way of fitting numerous spectra with a good precision. In Fig. 3.7, a measurement of the reference isotope ^{124}Sn in the $5p^2\ ^3P_0 \rightarrow 5p6s\ ^3P_1$ transition is depicted as an example. In general, the extraction of the hyperfine parameters and isotope shifts is relatively insensitive to the exact description of the line shape as long as the same profile is used for all the components.

The numerical calculation of the true *Voigt profile* is time-consuming, and therefore inappropriate for a fitting routine. Instead, the *extended pseudo-Voigt profile* described in [74] is used. It contains two symmetric functions, irrational and hyperbolic, in addition to the original Gaussian and Lorentzian functions for approximating the *Voigt profile*. [75].

Chapter 4

Data analysis and results

The only trouble with a sure thing is the uncertainty.

- Taken from a teabag -

4.1 Independent analysis

4.1.1 Fitting procedure I

Using the ROOT framework [76] with the MINUIT2 [77] package for the minimization procedure a fitting routine is written in C++ to fit the experimental data. The position of each resonance is constrained by the following expression

$$\begin{aligned}\nu_{\text{peak};i}^{A'} - \nu_i^A &= c_1 A_{(5p6s^1P_1)} + c_2 B_{(5p6s^1P_1)} + \delta\nu_i^{A,A'} \\ \nu_{\text{peak};j}^{A'} - \nu_j^A &= c_3 A_{(5p6s^3P_1)} + c_4 B_{(5p6s^3P_1)} + \delta\nu_j^{A,A'}\end{aligned}$$

where $i : 5p^2^1S_0 \rightarrow 5p6s^1P_1$ and $j : 5p^2^3P_0 \rightarrow 5p6s^3P_1$ are the studied transitions, $c_{1,2,3,4}$ are constants that depend on J , I and F , see (2.47) and (2.50), $A_{(5p6s^1,3P_1)}$ and $B_{(5p6s^1,3P_1)}$ are the hyperfine structure constants of the corresponding states, $\delta\nu_{i,j}^{A,A'}$ is the isotope shift in the transition i or j and $\nu_{i,j}^A$ is the transition frequency of the reference isotope, ^{124}Sn . The latter was selected based on the fact that it is a stable isotope with no hyperfine splitting ($I = 0$) and it is in the center of the range of measurement.

Table 4.1: Parameters in the fitting routine.

Name	Nomenclature	Fit
Isotope shift	$\delta\nu^{A,A'}$	free
Isomer shift	$\delta\nu^{A^{(g)},A^{(*)}}$	free
<i>A</i> -factor	A	free
<i>B</i> -factor	B	free
Nuclear spin	<i>I</i>	fixed
Total elect. angular momentum	<i>J</i>	fixed
Gaussian width	Γ_G	free
Lorentzian width	Γ_L	free
Baseline	BL	free
Relative peak intensities	$\mathcal{I}_{F \rightarrow F'}$	free/fixed

The total fit function is built as a sum of a *pseudo-Voigt profile* at each resonance position. If an isomeric state is present, the two structures are fitted simultaneously with the difference between their centroids as a link parameter, known as isomer shift. The parameters of the fit are summarized in Tab. 4.1.

4.1.2 The $5p^2\ ^1S_0 \rightarrow 5p6s\ ^1P_1$ transition

Data were recorded in the entire range from $^{109,112}\text{Sn}$ up to ^{134}Sn . The fluorescence spectra of the long-lived isomers in ^{113}Sn , ^{123}Sn , ^{128}Sn and the ground states of ^{133}Sn , ^{134}Sn were assessed for the first time. The spectra were analyzed following the procedure explained in Sec. 4.1.1.

The hfs splittings in this transition are small, in certain cases comparable with the experimental linewidth. The following two examples have the purpose of demonstrating the ambiguity that is present in the analysis for most of the odd-*A* cases due to the unresolved singlet state. These difficulties are later resolved by doing a combined analysis including the triplet state, as presented in the following sections. In Fig. 4.1, under the assumption of spin 7/2, which will be confirmed in the next chapter, there are two possible variations of the fitting (upper and lower panel), corresponding to markedly different electromagnetic moments. The reduced chi-square of the two fits is nearly the same, being difficult to discriminate between the two based on the quality of

the fit.

Fig. 4.2 shows a more complicated case, where a long-lived isomeric state is present. The weaker state, ($I = 3/2$), is superimposed with the isomeric ($I = 11/2$) state. All the expected resonances of the latter (three) were resolved while only one resonance was indicative of the low-spin state. The hyperfine constants of the well-resolved state are in agreement in the two fits, within the errors, while differences appear for the non-resolved one.

A second transition is studied in order to constrain the fit and to extract a final set of hyperfine parameters.

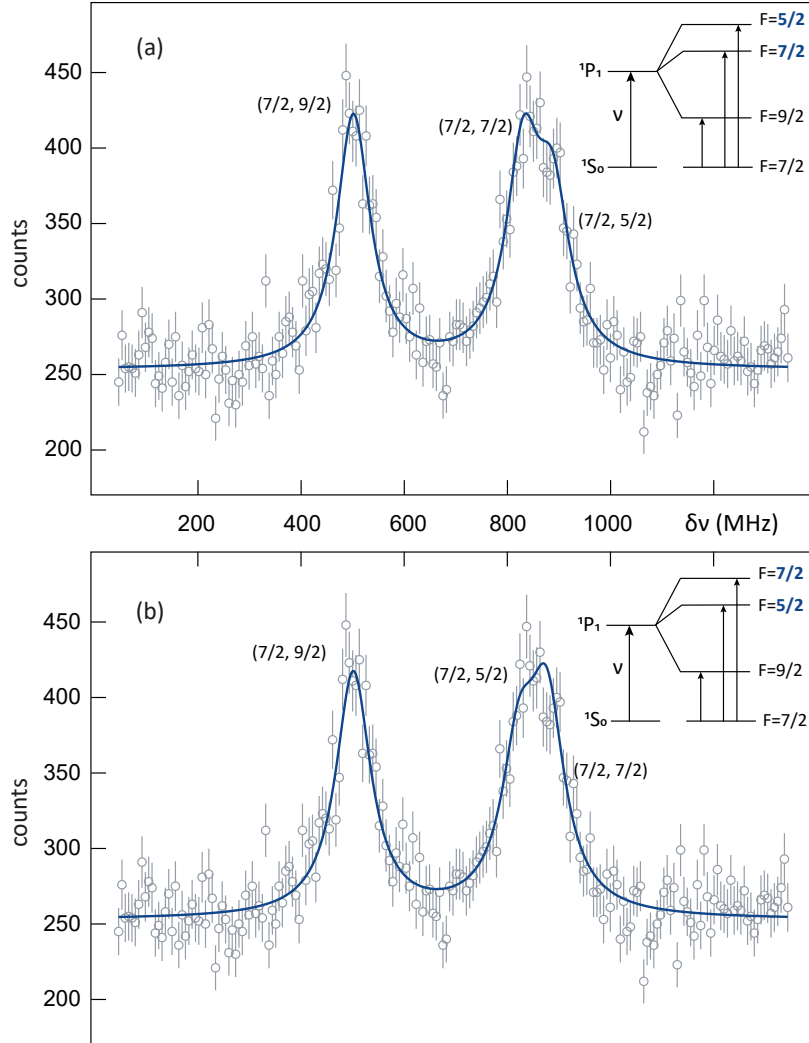


Figure 4.1: Hyperfine structure of ^{133}Sn in the $5p6s \ ^1P_1$ level. The solid line represents a fit of the ground $7/2^-$ state with fixed intensities under two assumptions for the hyperfine states ordering in 1P_1 (upper and lower panel). The hyperfine components have been labeled by the corresponding F quantum numbers. The x -axis is relative to the resonance frequency of ^{124}Sn . The $\chi_{\text{red}}^2 = 1.06$ in (a) and $\chi_{\text{red}}^2 = 1.09$ in (b), for the same NDF. The reversal of the $5/2$ and $7/2$ hyperfine states in the two fits is visible from the shape of the right maximum.

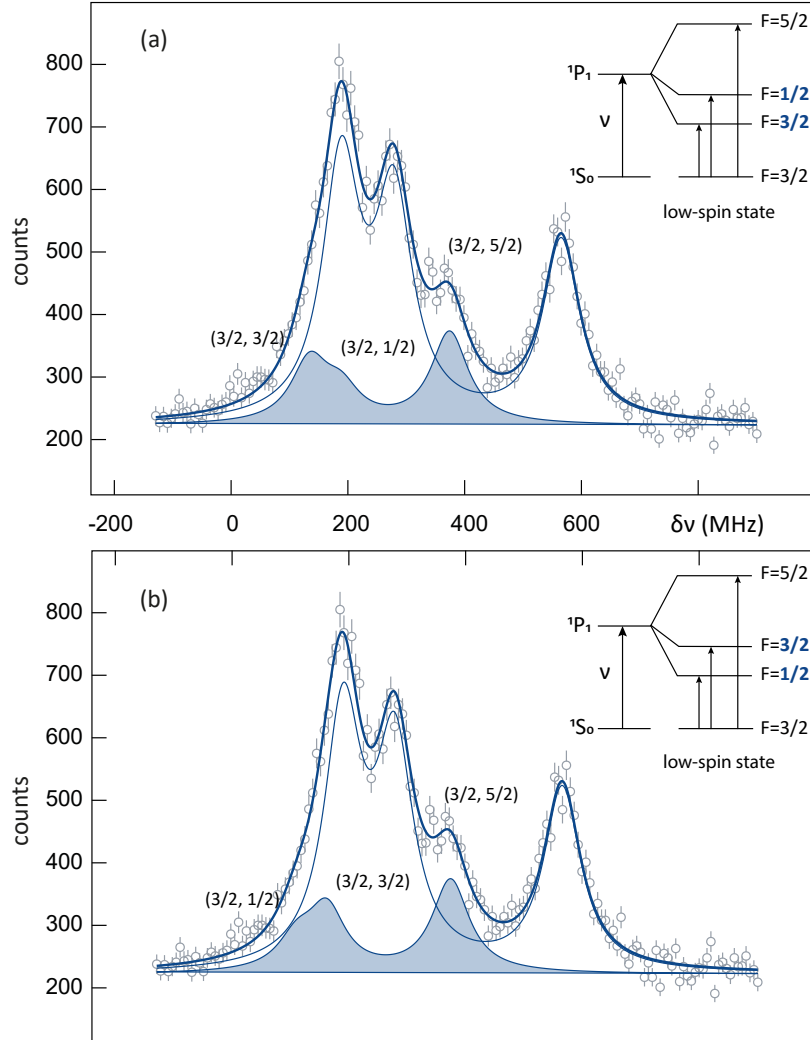


Figure 4.2: Hyperfine structure of ^{129}Sn . The thick blue line represents a total fit of two states on a common background. The lower-spin state ($I = 3/2$) is indicated by a semitransparent fill under two assumptions for the level ordering in 1P_1 (upper and lower panel). The hyperfine components of the latter have been labeled by the corresponding F quantum numbers. The x -axis is relative to the resonance frequency of ^{124}Sn . The $\chi_{\text{red}}^2 = 1.22$ in (a) and $\chi_{\text{red}}^2 = 1.21$ in (b), for the same NDF.

4.1.3 The $5p^2\ ^3P_0 \rightarrow 5p6s\ ^3P_1$ transition

The magnetic splitting of the excited state in this transition is twenty times larger than the one of the previously-discussed singlet state; therefore, the spectra are completely resolved. The spectroscopy was performed along the entire neutron-rich range $^{108-134}\text{Sn}$. The experimental data is fitted following the same procedure explained before. The hyperfine parameters A were extracted with high precision for all the measured isotopes except for $^{129,131}\text{Sn}$ and the odd-even cases with $I \neq 0$, where two resonances belonging to different states collided. Hyperfine parameters B were also extracted, with a somewhat smaller relative accuracy due to a smaller quadrupole splitting.

By way of illustration, the hyperfine spectra recorded in this transition for the same two isotopes considered in Sec. 4.1.2 are shown in Fig. 4.3 and Fig. 4.4. In the first case, the resonances are distant from each other, and the fitting is constrained to only one set of hyperfine coupling constants. In the second one, the smaller resonance of the ground ($I = 3/2$) state coincides with the strongest resonance of the isomeric ($I = 11/2$) state, reducing the accuracy of the hyperfine parameters mainly for the low-spin state. The reduced chi-square of the two fits is the same for the same NDF.

A more complex analysis, consisting in a simultaneous fitting of the two transitions has been performed in order to obtain the highest possible accuracy for all the parameters. The details and the results of this analysis are explored in the following section.

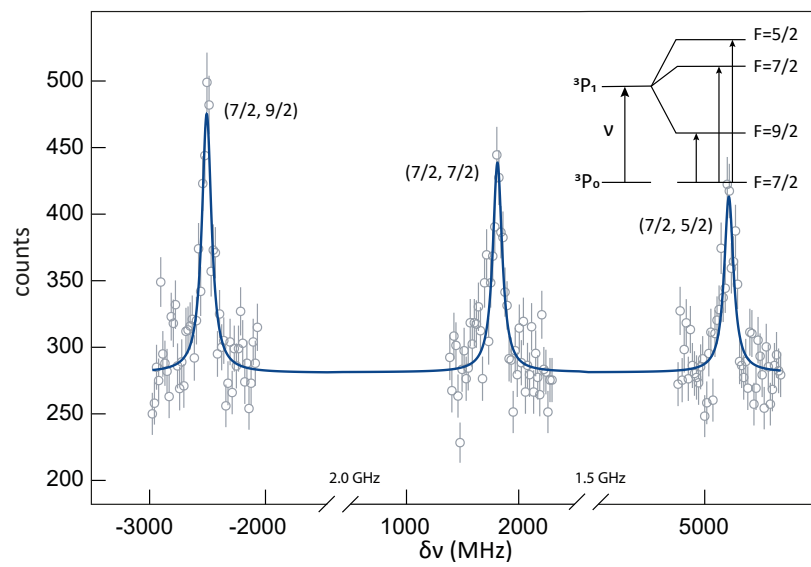


Figure 4.3: Hyperfine structure of ^{133}Sn in the $5p6s\ ^3P_1$ level. The hyperfine components have been labeled by the corresponding F quantum numbers. The frequency scale is relative to the resonance frequency of ^{124}Sn .

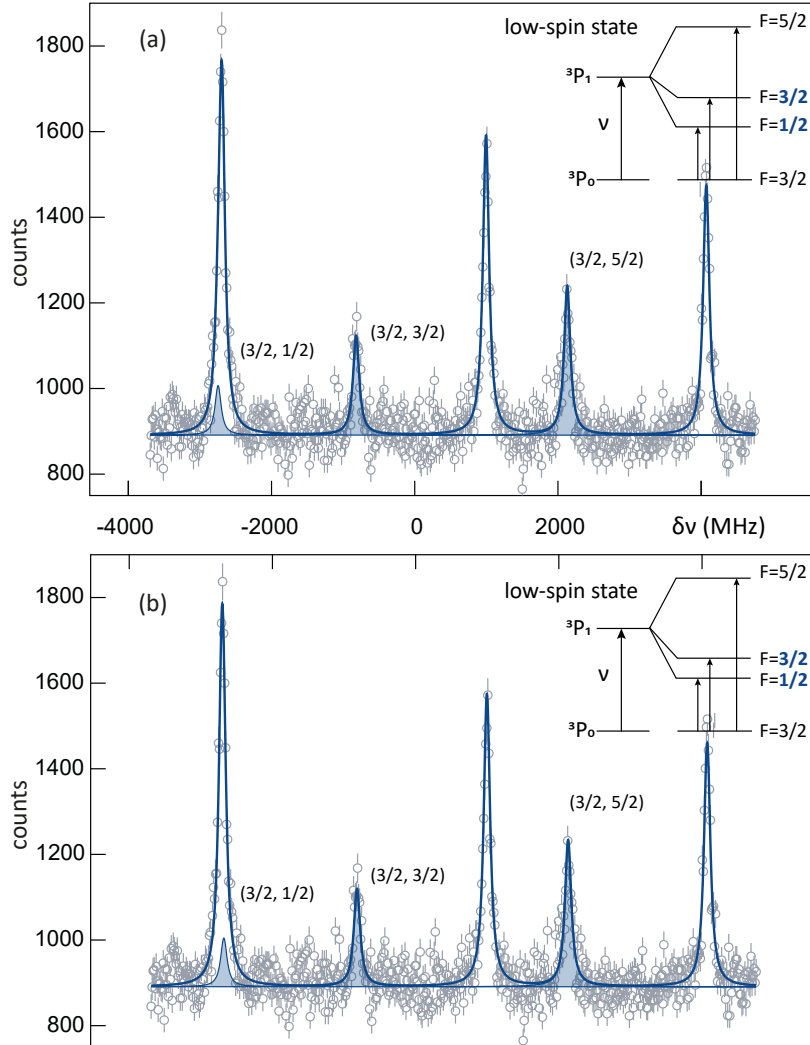


Figure 4.4: Hyperfine structure of ^{129}Sn in the $5p6s\ ^3P_1$ level. The thick blue line represents a total fit of two states on a common background. The lower-spin state ($I = 3/2$) is indicated by a semitransparent fill. The hyperfine components of the latter have been labeled by the corresponding F quantum numbers. The x -axis is relative to the resonance frequency of ^{124}Sn . The $\chi_{\text{red}}^2 = 1.80$ in (a) and $\chi_{\text{red}}^2 = 1.81$ in (b), for the same NDF.

4.2 Simultaneous analysis

A self-consistent analysis of the two data sets is performed in order to obtain the highest possible accuracy for all the parameters involved in the fit. As explained before, the singlet state provided high sensitivity to quadrupole moments while the triplet facilitated a large magnetic splitting. The fit function was set in such a way that the free hyperfine parameters were the $A_{(5p6s\ ^3P_1)}$ and the $B_{(5p6s\ ^1P_1)}$ while the others hyperfine parameters were constrained to the corresponding ratios. The results obtained from this analysis are considered as final results and are used to determine the magnetic and quadrupole moments of the tin nuclei.

4.2.1 Fitting procedure II

For the simultaneous analysis a more sophisticated C++ code is implemented. The code fits all the spectra of the same isotope in the two transitions simultaneously. A combined χ^2 is built and minimized using the MINUIT2 package of ROOT. The hyperfine parameters of the two atomic states are connected via the ratios defining the position of each resonance as follow

$$\nu_{\text{peak};i}^{A'} - \nu_i^A = c_1 R_A A_{(5p6s\ ^3P_1)} + c_2 B_{(5p6s\ ^1P_1)} + \delta\nu_i^{A,A'}$$

$$\nu_{\text{peak};j}^{A'} - \nu_j^A = c_3 A_{(5p6s\ ^3P_1)} + c_4 R_B B_{(5p6s\ ^1P_1)} + \delta\nu_j^{A,A'}$$

where $i : 5p^2\ ^1S_0 \rightarrow 5p6s\ ^1P_1$ and $j : 5p^2\ ^3P_0 \rightarrow 5p6s\ ^3P_1$ and R_A and R_B are the *hyperfine coupling constants ratio*. The ratios were fixed in the fit and shared for all the isotopes. The procedure for its determination is explained in the following section. The isotope shift, linewidth, baseline and the relative intensities were kept free and independent for each measurement. The relative parameters, hyperfine constants and isomer shifts were kept free but common for all the scans of the same isotope.

4.2.2 *A* and *B*-ratios

The ratio of the hyperfine constants, R_A and R_B , of the two atomic states, can be considered constant along the isotopic chain. For the extraction of the first one, the three stable isotopes with $I = 1/2$, i.e., $B_{(5p6s\ 1,3P_1)} = 0$, were selected. The simultaneous approach explained before has been used to fit all the spectra of these isotopes in the two transitions, with R_A as a free parameter. The extracted value is $R_A = A_{(5p6s\ 1P_1)}/A_{(5p6s\ 3P_1)} = 0.0517(1)$. This value may deviate slightly for isotopes with different spins if one takes into account the sensitivity of the atomic states to the nuclear magnetization distribution, the so-called hyperfine anomaly [78, 79]. This effect is expected to be considerably smaller than the 2×10^{-3} relative uncertainty on the above ratio, which therefore is statistically consistent to the corresponding ratio in states with any other spin. Only for the observed spin of $1/2$, there are isotopes in the tin chain studied by Nuclear Magnetic Resonance (NMR); therefore, the anomaly cannot be estimated. The overall accuracy of the magnetic moments will be further improved by a dedicated computational study of the anomaly in the relevant atomic state. For the determination of R_B , two isotopes were selected, ^{109}Sn and ^{133}Sn , based on the non-presence of an isomeric state in the spectrum. R_A was fixed in the fitting where all the scans in the two transitions were analyzed simultaneously. The value of $R_B = B_{(5p6s\ 3P_1)}/B_{(5p6s\ 1P_1)} = -0.25(2)$ was extracted.

4.2.3 Even-even isotopes

The first isomeric state ($I = 7$) in the even-even isotopes, ^{128}Sn and ^{130}Sn , was assessed during the experimental campaigns. The first one was measured for the first time. The hyperfine parameters A were extracted with high precision for both isotopes, allowing the determination of their magnetic moments. A negative sign was unambiguously determined from the fit. Hyperfine B parameters were also extracted; however, they were found to have contrary signs for the two isotopes, a fact that could be a result of the non-resolved hyperfine structure of ^{128}Sn in the singlet. Example spectra of both isotopes are shown in Fig. 4.5 and 4.6. The two fits in the figure lead to similar hyperfine parameters $A_{(5p6s\ 3P_1)}$ of negative sign and similar absolute values of the hyperfine

parameters $B_{(5p6s\ ^1P_1)}$. The differences between the results of the fit for (a) and (b) lie in the sign of $B_{(5p6s\ ^1P_1)}$, which is positive in (a) and negative in (b), for both isotopes. In Fig. 4.5, the correct fit is evident from the shape of the left maximum in the singlet and the reduced chi-square. The fit in (a) can be selected as the correct one leading to a positive value of the quadrupole moment for this isotope. The value reported in the literature [8] is negative, which is in contradiction with the one reported in this thesis. We have to note that the literature value was extracted from the B factor in the $5p6s\ ^3P_1$ state which offers lower sensitivity to quadrupole splitting. The value reported here has benefited from the simultaneous fitting of the two levels, mainly in the singlet where the quadrupole splitting is about four times larger than in the triplet.

In the case of ^{128}Sn , depicted in Fig. 4.6, within the envelope of the resonances it is not possible to determine the correct fit. Based on the chi-square the right fit is the one in (b), which gives a negative value for the quadrupole moment. The hfs splitting of this isomer in the singlet is comparable with the experimental linewidth, and the results of the fit are constrained only by the small peak in the lower frequency side because the quadrupole splitting in the triplet is nearly zero. Therefore, the negative sign has to be further investigated. The nuclear properties of this state are unknown and the results presented here are the most accurate yet. The selected results are summarized in Tab. 4.2.

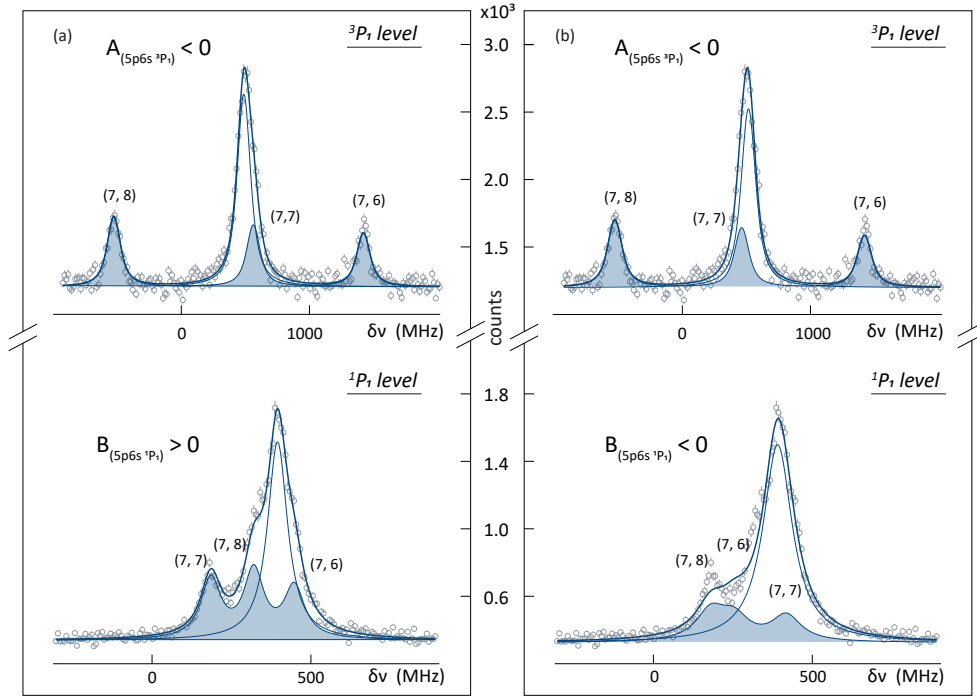


Figure 4.5: Simultaneous fitting of the hyperfine spectra of ^{130}Sn in the $5p6s\ ^3P_1$ and $5p6s\ ^1P_1$ levels. Two possible ways of fitting are labelled as (a) and (b) corresponding to a positive and negative value of $B_{(1P_1)}$, respectively. $A_{(3P_1)}$ is negative in both cases. The thick blue line represents a total fit of two states on a common background. The isomeric state ($I = 7$) is indicated by a semitransparent fill under two assumptions for the level ordering in 1P_1 , (a) and (b). The hyperfine components of the latter have been labeled by the corresponding F quantum numbers. The x -axis is relative to the resonance frequency of ^{124}Sn . The $\chi_{\text{red}}^2 = 1.68$ in (a) and $\chi_{\text{red}}^2 = 2.45$ in (b), for the same NDF.

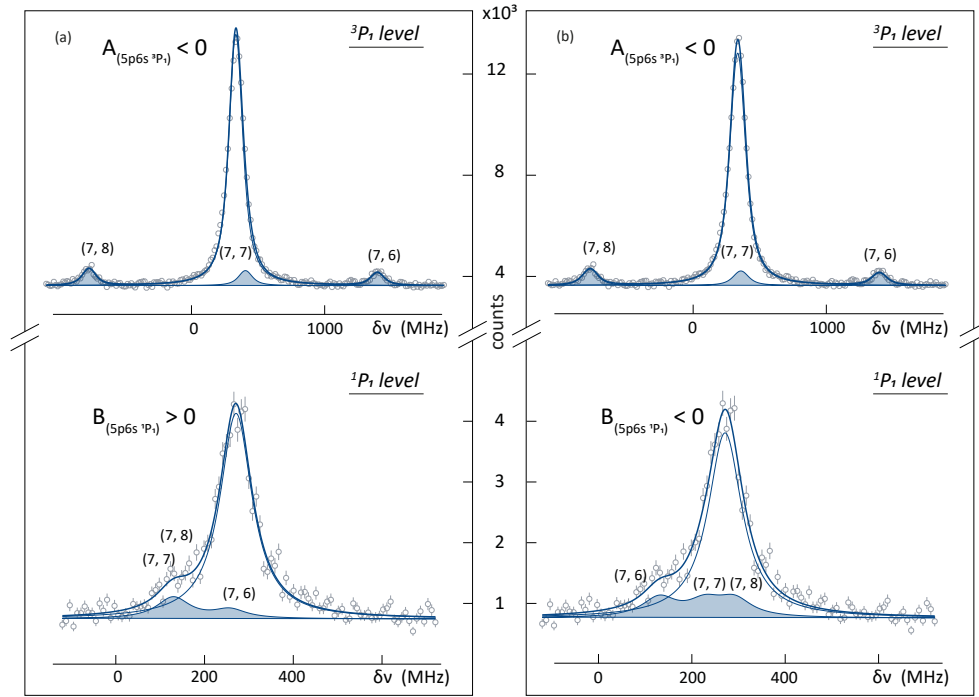


Figure 4.6: Simultaneous fitting of the hyperfine spectra of ^{128}Sn in the $5p6s\ ^3P_1$ and $5p6s\ ^1P_1$ levels. Two possible ways of fitting are labelled as (a) and (b) corresponding to a positive and a negative value of $B_{(1P_1)}$, respectively. $A_{(3P_1)}$ is negative in both cases. The thick blue line represents a total fit of two states on a common background. The isomeric state ($I = 7$) is indicated by a semitransparent fill under two assumptions for the level ordering in 1P_1 , (a) and (b). The hyperfine components of the latter have been labeled by the corresponding F quantum numbers. The x -axis is relative to the resonance frequency of ^{124}Sn . The $\chi_{\text{red}}^2 = 2.37$ in (a) and $\chi_{\text{red}}^2 = 1.78$ in (b), for the same NDF.

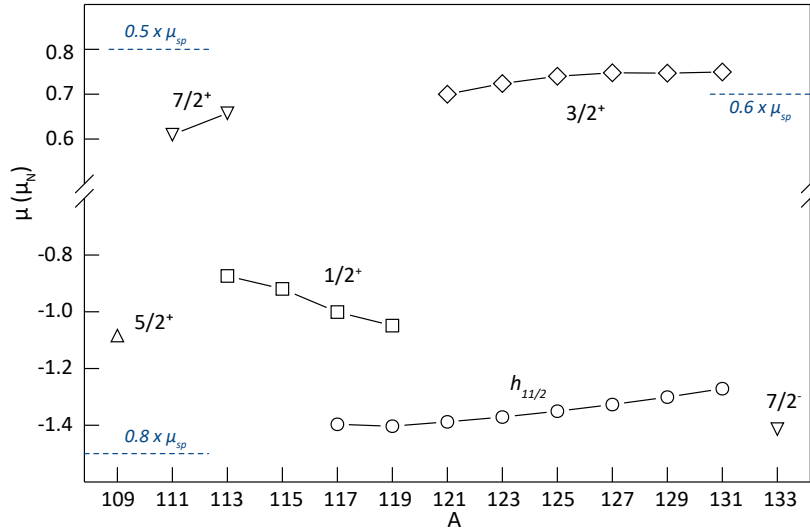


Figure 4.7: Magnetic moments of odd isotopes in the tin chain. The experimental error bars are smaller than the markers. The dotted lines represent the single-particle Schmidt values for each configuration.

4.3 Nuclear moments

4.3.1 Magnetic moments

The nuclear magnetic dipole moments were evaluated from the hyperfine constants $A_{(5p6s\ 3P_1)}$ with the aid of (2.45) using as reference the known value of the magnetic moment of ^{117}Sn [80], derived from NMR measurements and corrected for diamagnetism. The resulting values are presented in Tab. 4.2 and plotted in Fig. 4.7.

The sign of the extracted moments, including the magnetic moments of the odd-neutron isotopes reported in this work for the first time, agrees with the ones predicted by the corresponding Schmidt moments, yet the values differ by an average of 35%. As expected, the nucleus with the closest magnetic moment to the Schmidt value is the double-magic plus one neutron nucleus ^{133}Sn with a deviation of about 26%. This might suggest a closed shell structure of its ground state for which the single-particle model can be considered as a fair approximation.

Table 4.2: Hyperfine parameters and electromagnetic moments of tin isotopes determined from this work. Uncorrelated and correlated uncertainties are enclosed in parentheses and square brackets, respectively. Asterisks refer to isomeric states. Magnetic moments derived from NMR [80] measurements are showed for comparison, where available.

$N + Z$	I^π	$A_{(5p6s\ ^3P_1)}$ (MHz)	μ (μ_N)	$\mu_{(NMR)}$ (μ_N)	$B_{(5p6s\ ^1P_1)}$ (MHz)	Q (mb)
109	5/2 ⁺	-1035.8 (6)	-1.0837 (7)		154 (5)	+259 (8) [26]
111	7/2 ⁺		+0.6097 (14) ^a			+153 (27) [15] ^b
113	1/2 ⁺	-4176.0 (256)	-0.8738 (53)			
113*	7/2 ⁺	448.9 (6)	+0.6575 (9)		144 (1)	+243 (2) [24]
115	1/2 ⁺	-4393.8 (23)	-0.9194 (5)	-0.91883 (7)		
117	1/2 ⁺	-4784.2 (33)		-1.00104 (7) ^c		
117*	11/2 ⁻	-606.9 (3)	-1.3967 (8)		-185 (3)	-312 (5) [31]
119	1/2 ⁺	-5012.5 (21)	-1.0488 (4)	-1.04728 (7)		
119*	11/2 ⁻	-609.7 (4)	-1.4033 (9)		-121 (2)	-204 (4) [20]
121	3/2 ⁺	1115.0 (19)	+0.6999 (12)		-37 (3)	-62 (5) [6]
121*	11/2 ⁻	-603.1 (3)	-1.3880 (7)		-64 (2)	-107 (3) [11]
123	11/2 ⁻	-595.7 (3)	-1.3711 (7)		-9 (1)	-15 (2) [2]
123*	3/2 ⁺	1152.9 (18)	+0.7237 (11)		-18 (2)	-30 (4) [3]
125	11/2 ⁻	-586.8 (2)	-1.3505 (5)		43 (1)	+73 (2) [7]
125*	3/2 ⁺	1178.8 (17)	+0.7400 (10)		12 (3)	+20 (05) [2]
127	11/2 ⁻	-576.6 (3)	-1.3270 (6)		78 (2)	+132 (3) [13]
127*	3/2 ⁺	1191.1 (27)	+0.7477 (17)		41 (7)	+69 (12) [7]
128*	7 ⁻	-144.5 (4)	-0.4229 (11)		-118 (28)	-199 (47)[20]
129	3/2 ⁺	1189.9 (25)	+0.7469 (16)		61 (4)	+103 (6) [10]
129*	11/2 ⁻	-565.2 (2)	-1.3008 (5)		119 (2)	+200 (3) [20]
130*	7 ⁻	-130.3 (3)	-0.3816 (9)		222 (2)	+374 (4) [37]
131	3/2 ⁺	1194.0 (13)	+0.7495 (8)		60 (2)	+101 (3) [10]
131*	11/2 ⁻	-552.3 (2)	-1.2711 (5)		144 (2)	+242 (3) [24]
133	7/2 ⁻	-965.2 (5)	-1.4138 (8)		-102 (3)	-172 (5) [17]

^{a,b} Extracted in the $5p6s\ ^1P_1$ multiplet.

^c Magnetic moment used as reference.

The systematic measurement of eight magnetic moments in the $11/2^-$ states can provide some insights into the shell structure in the region. A comparison for the same states in the neighboring cadmium and tellurium elements is plotted in Fig. 4.8. The magnetic moments of the tin isotopes are closer to the Schmidt value than those of the isotopes with two holes inside and two protons outside the shell closure which might mean that the magnetic moments are sensitive to second-order core polarization. Another observation is the deviation of the trend occurring in the three elements at $N = 70$. This could be related to a first-order core polarization effect that should be minimal at the middle of the shell. It was suggested in [3] that the neighboring orbitals $3s_{1/2}$, $2d_{3/2}$, $2d_{5/2}$ and $1h_{11/2}$, of relevance to the cadmium, tin, and tellurium isotopes, are nearly degenerate and fairly separated from the $1g_{7/2}$. Under this assumption, the region between $N = 58$ and $N = 82$ could be considered as an isolated subshell with the middle at $N = 70$. The observed behavior in tin might provide added support to the assumed structure that is beside sustained by a recent theoretical study of the cadmium chain from a simple shell model picture [81]. Finally, we should expect that of a pair of isotopes that differ by two neutrons, the nucleus closest to the shell gap has a magnetic moment closer to the Schmidt value, as occurs for the tellurium isotopes. This is not the case in tin where the magnetic moment of ^{129}Sn is closer to the single particle value than ^{131}Sn . Nevertheless, all the isotopes have almost identical magnetic moments, and the deviation is very small in comparison with the same occurrence in the cadmium isotopes. This might be an effect of the first-order core polarization mentioned above that gives a deviation from the Schmidt value more accentuated in cadmium than in tin.

Comparison with literature values

Fig. 4.12 shows a compilation of literature values, magnetic moments are displayed on the left side and quadrupole moments in the right side, reported to date. For a more clear comparison with our measurements, the differences between this work and literature are plotted. The error of our measurements is enclosed by shading bands. As can be seen on the left side of the figure, the overall agreement is good within the error bars except for the isotopes ^{125}Sn , ^{127}Sn and ^{129}Sn with $I = 3/2$, derived from a laser spectroscopy experiment

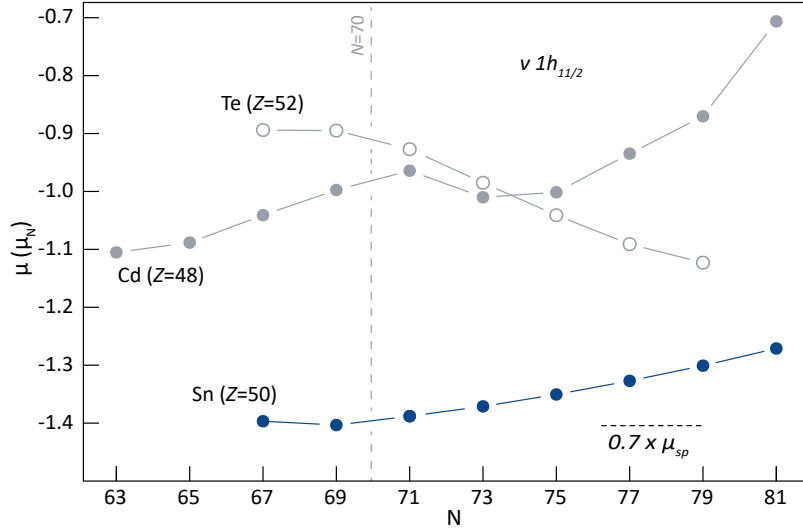


Figure 4.8: Magnetic moments of the $h_{11/2}$ neutron states in cadmium, tin and tellurium. The dashed black line represents the single particle magnetic moment calculated with the Schmidt value for the $h_{11/2}$ orbit. The experimental error bars are smaller than the markers.

in the $5p6s$ 3P_1 state [8]. We have to point out that the overall accuracy of the results presented in this thesis has benefited from the study of two complementary transitions.

4.3.2 Quadrupole moments

As explained in Ch.2, the spectroscopic quadrupole moment of a nucleus can be measured from the hyperfine splitting of the atomic spectral line if the electric field gradient generated by the electrons at the position of the nucleus, V_{JJ} in (2.51), is known. For the $5p6s$ 1P_1 and $5p6s$ 3P_1 -configurations, the corresponding field gradients have been calculated by Eberz *et al.* [7] following two theoretical approaches. The resulting values are,

$$eV_{JJ}({}^1P_1) = 593(59) \text{ MHz/b},$$

$$eV_{JJ}({}^3P_1) = -138(13) \text{ MHz/b}$$

The ratio $R_{V_{JJ}} = V_{JJ}({}^3P_1)/V_{JJ}({}^1P_1) = -0.23(3)$ is in good agreement with

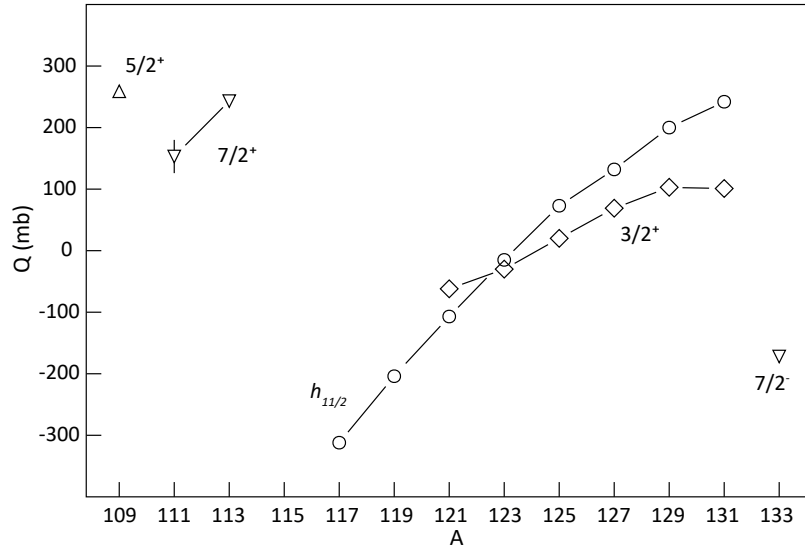


Figure 4.9: Quadrupole moments of odd-isotopes in the Sn chain. The experimental error bars are smaller than the markers except for ^{111}Sn . See text for details.

the experimental ratio, $R_B = -0.25(2)$, determined in this work. The quadrupole moments listed in Tab. 4.2 and plotted in Fig. 4.9 are determined using the field gradient estimated by Eberz and the $B_{(5p6s\ 1P_1)}$ factors extracted from the simultaneous fitting. The overall accuracy of the quadrupole moments will be further improved due to a dedicated computational study of the electric field gradient, triggered by the results of this work, in the relevant atomic states.

We have to note in Fig. 4.9 that experimental errors bars are smaller than the markers except for ^{111}Sn . The hyperfine structure of this isotope was measured only in the triplet state and therefore the simultaneous analysis could not be used. Its quadrupole moment was determined using $B_{(5p6s\ 3P_1)}$ and the electric field gradient for this state-configuration.

Statistical errors are due to the experimental uncertainty of $B_{(5p6s\ 1P_1)}$. The systematic error of the latter is very small and can be neglected while the electric field gradient introduces a systematic uncertainty of about 10%, see Tab. 4.2.

The quadrupole moments of the $11/2^-$ states show a nearly linear trend as a

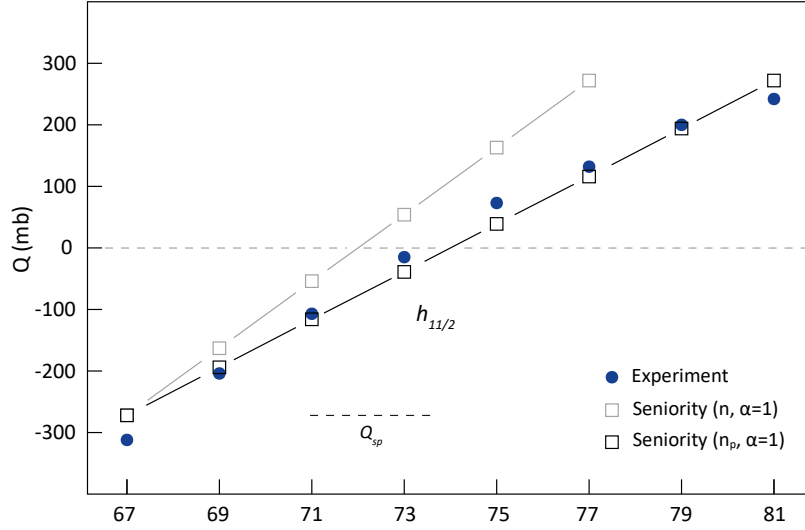


Figure 4.10: Experimental quadrupole moments of the $I^\pi=11/2^-$ states in tin compared to those calculated using the seniority scheme. See text for details.

function of the neutron number. They are plotted in Fig. 4.10 and compared with those calculated in the framework of the seniority scheme [35] for n nucleons filling a j -orbital. Squares represent the quadrupole moment calculated with the aid of (2.31) assuming that one of the valence nucleons is unpaired ($\alpha=1$ or “normal coupling”). The $\langle \hat{Q}_{zz} \rangle_\nu^{S.P.}$ is calculated using (2.29) where $\langle r_j^2 \rangle_\nu$ is approximated by 5/3 of the mean square charge radius of ^{117}Sn [82], considering spherical nuclei with uniform charge distributions. The resulting value is $\langle \hat{Q}_{zz} \rangle_\nu^{S.P.} = -273$ mb. The difference between the black and grey squares lies in the assumption of n . For the first case (grey squares), n is determined in the spherical shell model framework, where the filling of the $h_{11/2}$ orbit involves $n = 1$ neutron at $N = 67$ up to $n = 11$ at $N = 77$. This simple estimation does not agree with the experimental behavior; either can reproduce the number of eight quadrupole moments following a systematic trend. Therefore, in the second case, n is defined in terms of the probability p for pair occupation suggested in [3], n_p . This interpretation assumes that the relevant orbitals are degenerate in terms of total energy per pair. Under this assumption, there are $n_p = 11$ neutrons in ^{131}Sn down to $n_p = 1$ neutron in ^{117}Sn , being able to explain the n dependence of the quadrupole moments beyond

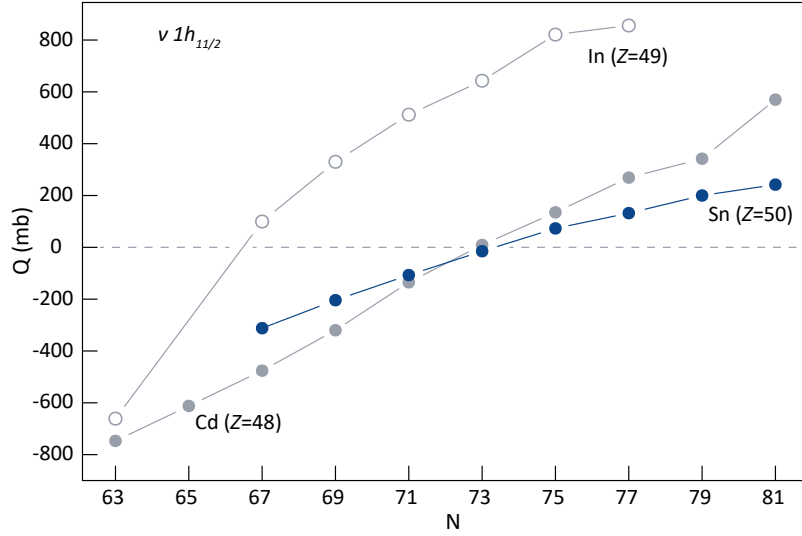


Figure 4.11: Systematics of the $h_{11/2}$ neutron states in cadmium, indium and tin. The plotted values for indium were determined with the aid of the quadrupole additivity rule of the $I = 8$ isomeric states [83] while the quadrupole moments of cadmium were taken from [3]. See text for details.

the natural capacity of the $h_{11/2}$ shell. The quadrupole moments obtained in this way seem to reproduce the experimental trend. According to (2.31), the observed moments should cross zero at mid-shell, $N = 74$, which fairly agrees with the experimental observation. An empirical $\langle \hat{Q}_{zz} \rangle_{\nu, \text{emp}}^{S.P.}$ can be estimated by averaging the quadrupole moment produced by the unpaired neutron and the single-hole at the beginning and at the end of the shell, respectively, resulting in a value of $\langle \hat{Q}_{zz} \rangle_{\nu, \text{emp}}^{S.P.} = -277$ mb. The comparison of this empirical value with the one predicted by the shell model leads to an effective charge of $e_{\nu}^{\text{eff}} = 1.01e$. The observed trend is not as linear as the one observed in cadmium for which a strong first-order core polarization was suggested. The small effective charge together with the quantitative agreement between the calculated and the experimental moments might suggest a spherical core with no considerable influence in the quadrupole moments as expected for a semi-magic nucleus. The latter assumption was also indicative of the analysis of the magnetic moments.

In Fig. 4.11, the $h_{11/2}$ quadrupole moments in tin, cadmium, and indium are

compared as a function of the neutron number. For indium, semi-empirical quadrupole moments were calculated with the aid of the additivity rule for quadrupole moments [84] using the experimental quadrupole moments of the odd-odd $I = 8$ isomeric states and the adjacent odd-even indium isotopes with $I = 9/2$. The configuration $[\pi(1g_{9/2})^{-1}\nu(1h_{11/2})]^{8-}$ is assumed for the $I = 8$ states. In all cases, a transition from negative to positive quadrupole moments, as the neutron shell is filled, is characteristic of the observed trends. The measured quadrupole moments in tin are about half of the measured values in cadmium. It was suggested in [3] and supported in [85] that the deformed proton core in cadmium contributes to half of each measured quadrupole moment. The proton-core polarization was reflected in a large effective charge of about $e_{\nu}^{\text{eff}} = 2.5e$. This could explain the quantitative differences with tin, for which an effective charge of about $e_{\nu}^{\text{eff}} = 1.01e$ was determined. A singular agreement for the quadrupole moments for cadmium and indium is observed only at $N = 63$. The remarkable discrepancies result in an underestimation of the quadrupole moments of the $I = 8$ states in indium when considering the neutron contribution from the cadmium chain.

Comparison with literature values

On the right side of Fig. 4.12, the differences between the values extracted in this work and literature values for low and high spin states have been plotted versus the atomic mass number. Small differences, arising from the use of a different V_{JJ} , are observed for isotopes with $A < 125$, however, remarkable differences are observed for $A \geq 125$. The latter have been measured using the hyperfine parameters B in the 3P_1 atomic state poorly sensitive to quadrupole splitting, which is evident in the large error bars of the measured moments.

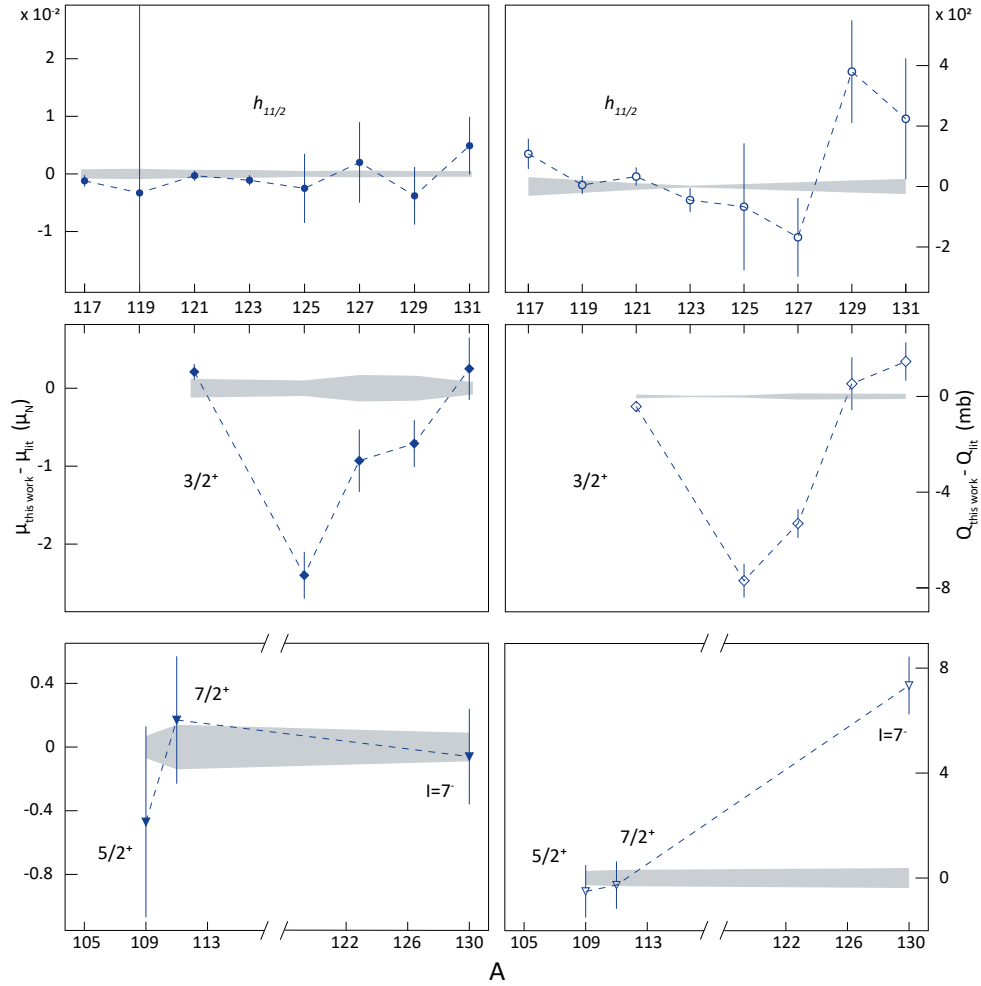


Figure 4.12: Differences between the values extracted in this work and literature values for low and high spin states versus the atomic mass number. Shaded bands represent the error associated with our measurements.

4.4 Charge radii

4.4.1 Isotope and isomer shifts

As mentioned in previous sections, the isotope shifts were determined with respect to ^{124}Sn . Statistical uncertainties arise from the experimental error on the absolute positions of the peaks while systematic uncertainties arise from the relative uncertainty of the source voltage $\Delta U_{acc}/U_{acc} \approx \Delta U_{offset}/U_{offset} \approx 1.5 \times 10^{-4}$. The extracted isotope shifts, as well as literature values from previous measurements, are presented in Tab. 4.3. The latter were converted to be relative to ^{124}Sn in order to compare with our results. They were converted by:

$$\delta\nu_{lit}^{124,A'} = \delta\nu_{lit}^{116,A'} + \delta\nu_{lit}^{124,116} \quad (4.1)$$

for [7]^a and

$$\delta\nu_{lit}^{124,A'} = \delta\nu_{lit}^{120,A'} + \delta\nu_{lit}^{124,120} \quad (4.2)$$

for [5, 8]^{b,c}.

A good agreement is found with respect to the values reported in [5, 7] within the error bars, however, some of the results presented in [8] are inconsistent with ours.

The high resolution provided by the technique and the presence of two states in the same spectrum allow the measurement of the field shift between isomer and ground state, the so-called isomer shift. The direct measurement of this effect, that in our case is sometimes a few MHz, benefits the overall accuracy of the extracted values being almost insensitive to systematic uncertainties. The isomer shifts derived from the analysis are presented in Tab. 4.4. The literature values were determined as the difference between the isotope shift in both states (ground and isomeric states) using the following relation:

$$\delta\nu_{lit}^{A'(g),A'(*)} = \delta\nu_{lit}^{A,A'(*)} - \delta\nu_{lit}^{A,A'(g)} = \nu_{lit}^{A'(*)} - \nu_{lit}^{A'(g)} \quad (4.3)$$

where A is the reference isotope and (g) and $(*)$ denote ground and isomeric state of the isotope A' , respectively.

Table 4.3: Isotope shifts of $^{108-134}\text{Sn}$ in the transitions $5p^2\ ^1S_0 \rightarrow 5p6s\ ^1P_1$ and $5p^2\ ^3P_0 \rightarrow 5p6s\ ^3P_1$, from this work and literature values [7]^a [5]^b [8]^c. Statistical uncertainties are quoted in round brackets while systematic uncertainties in square brackets.

		Isotope shifts (MHz)			
		$5p^2\ ^1S_0 \rightarrow 5p6s\ ^1P_1$		$5p^2\ ^3P_0 \rightarrow 5p6s\ ^3P_1$	
$N + Z$	I	This work	Literature values ^a	This work	Literature values ^{b,c}
108	0			-2416.8 (118) [98]	
109	5/2	-1895.4 (17) [51]	-1898.6 (80)	-2238.6 (19) [92]	
110	0			-2015.2 (103) [84]	-2007.7 (70)
111	7/2			-1910.6 (36) [77]	-1896.2 (170)
112	0	-1382.7 (17) [40]	-1380.3 (40)	-1652.1 (80) [71]	-1659.4 (2)
113	7/2	-1322.1 (14) [37]		-1574.4 (38) [65]	
114	0	-1115.4 (16) [32]	-1115.7 (20)	-1335.6 (86) [58]	-1341.8 (2)
115	1/2	-1044.2 (12) [29]	-1044.3 (20)	-1250.4 (28) [52]	-1246.1 (1)
116	0	-841.3 (9) [26]	-842.6 (80)	-1007.6 (92) [45]	-1017.2 (2)
117	1/2	-761.5 (9) [23]	-759.1 (10)	-906.6 (50) [40]	-912.6 (1)
118	0	-584.1 (24) [19]	-588.4 (20)	-688.0 (76) [33]	-711.4 (2)
119	1/2	-514.0 (10) [16]	-521.4 (20)	-619.7 (28) [28]	-620.7 (1)
120	0	-360.8 (8) [12]	-360.3 (40)	-448.6 (93) [22]	-441.2 (2)
121	11/2	-308.7 (23) [9]		-370.2 (20) [17]	-369.2 (17)
122	0	-166.7 (12) [6]	-162.8 (60)	-206.3 (84) [10]	-205.8 (15)
123	11/2	-114.5 (23) [3]		-135.5 (31) [5]	-144.0 (20)
125	11/2	48.4 (12) [3]		61.0 (24) [5]	63.2 (75)
126	0	146.8 (8) [7]		178.7 (69) [12]	188.9 (100)
127	11/2	190.5 (26) [9]		246.2 (32) [16]	243.9 (10)
128	0	270.4 (24) [12]		339.5 (51) [21]	359.9 (120)
129	11/2	326.5 (33) [15]		411.0 (30) [26]	439.9 (90)
130	0	396.1 (18) [18]		486.6 (44) [31]	564.9 (10)
131	11/2	449.9 (18) [20]		572.5 (21) [36]	784.9 (10)
132	0	498.1 (10) [24]		624.1 (34) [42]	698.9 (6)
133	7/2	705.8 (16) [26]		868.5 (29) [46]	
134	0	981.9 (36) [29]		1196.5 (83) [51]	

Table 4.4: Isomer shifts of $^{113-131}\text{Sn}$ in the $5p^2\ ^1S_0 \rightarrow 5p6s\ ^1P_1$ and $5p^2\ ^3P_0 \rightarrow 5p6s\ ^3P_1$ transitions. Statistical errors are quoted in round brackets. The systematic errors are negligible. Literature values are taken from [5]^a and [8]^b.

$N + Z$	Isomer shifts (MHz)		
	$5p^2\ ^1S_0 \rightarrow 5p6s\ ^1P_1$	$5p^2\ ^3P_0 \rightarrow 5p6s\ ^3P_1$	Literature values
	This work	This work	
113	-53 (6)	-87 (27)	
117	-11 (1)	-9 (2)	-12 (2) ^a
119	-10 (1)	-6 (3)	
121	-19 (3)	-15 (3)	-19 (3) ^a
123	7 (2)	5 (4)	
125	-10 (2)	-12 (3)	-48 (14) ^b
127	-24 (4)	-38 (3)	-63 (14) ^b
128	-39 (8)	-110 (4)	
129	58 (2)	60 (4)	87 (14) ^b
130	-83 (1)	-88 (3)	-100 (13) ^b
131	97 (1)	105 (2)	85 (16) ^b

4.4.2 King plot

To extract the isotopic differences between nuclear mean square charge radii, the optical electronic factors entering in (2.62) must be known. For its determination using the two studied transitions, a self-consistent procedure is performed. Following the procedure described in Sec. 2.3.3, the measured isotope shift and the known mean-square charge radii of the stable isotopes were linked through (2.63) and (2.65) and plotted in Fig. 4.13. With consistent data sets, the plots should result in two straight lines with the slopes and the y -intercepts linked by the F_i and K_i factors. A simultaneous fitting of the two King plots is performed with the electronic factors of the $i : 5p^2\ ^1S_0 \rightarrow 5p6s\ ^1P_1$ transition as a common parameter. The fit was performed using the ROOT framework with the MINUIT2 including x - and y -errors. In the first plot, Fig. 4.13 (a), only stable isotopes are used while in the two-lines King plot Fig. 4.13 (b) the rest of the measured isotopes in both transitions are included. The known values for the charge radii were taken from muonic measurements [86].

Table 4.5: Electronic field shift F and mass shift K factors deduced from *king plots*. Literature values from different experimental data sets [7]^a, [8]^c and Dirac-Fock calculations [7]^b are included for comparison.

	Electronic factors					
	$5p^2\ ^1S_0 \rightarrow 5p6s\ ^1P_1$			$5p^2\ ^3P_0 \rightarrow 5p6s\ ^3P_1$		
	This work	Literature values		This work	Literature values	
F (GHz/fm ²)	2.79 (23)	2.24 (27) ^a	1.98 ^b	2.98 (25)	3.30 (27) ^c	2.41 ^b
K (GHz u)	-724 (21)			-568 (23)	-761 (200) ^c	

All points lie fairly well on a straight line implying a good consistency between our two experiments and the muonic data. Statistical errors were included in a first fit to extract the parameters K and F and the error of the latter. Systematic error were included in a second fit to determine the uncertainty of the mass factor. The results are listed in Tab. 4.5. The extracted factors are statistically consistent with the values reported in the literature from the analysis of other experimental data and they are around 30% larger than the values predicted from Dirac-Fock calculations.

4.4.3 Charge radii

The $\delta\langle r^2 \rangle^{A,A'}$ values have been extracted from the experimental isotope shift with the aid of (2.62) and the electronic factors resulting from the King plot analysis. Statistical errors were propagated from (2.62), dominated by the statistical uncertainty on the isotope shift. For the correlated errors, the systematic uncertainties on the isotope shift, the masses, and the electronic factors were included. The two sets of arising values are listed in Tab. 4.6 and plotted against each other in Fig. 4.14 for all ground and isomeric states. The results in the two transitions are statistically consistent and in good agreement with the ones obtained from muonic data, when available. Their evolution as a function of the mass number is shown in Fig. 4.15.

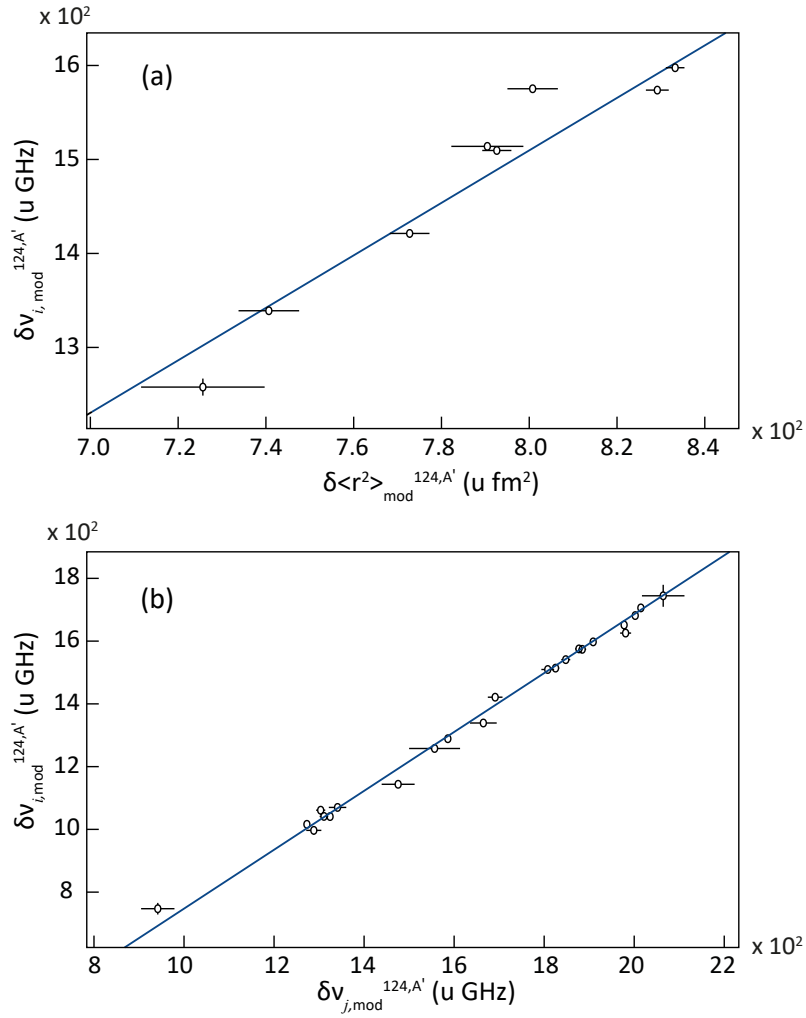


Figure 4.13: King plot of the measured isotope shifts against the differences in charge radii of stable isotopes (a) and King plot of the isotope shifts measured in the $i : 5p^2 1S_0 \rightarrow 5p6s^1 P_1$ transition versus the isotope shift measured in the $j : 5p^2 3P_0 \rightarrow 5p6s^3 P_1$ transition (b).

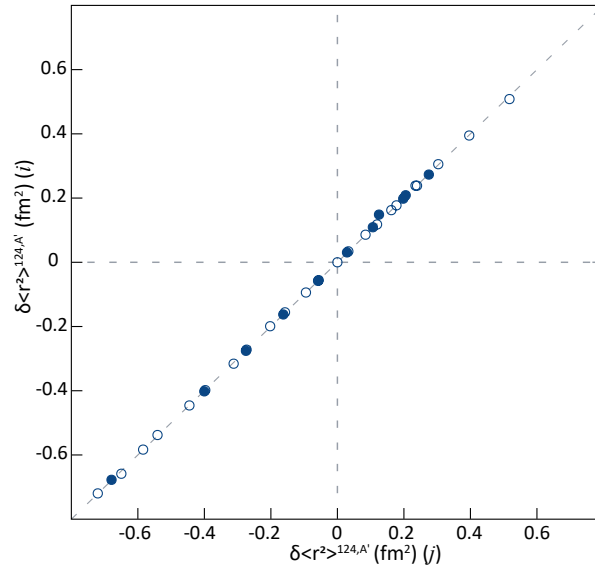


Figure 4.14: Changes in mean square nuclear charge radii determined in the $i : 5p^2 \ ^1S_0 \rightarrow 5p6s \ ^1P_1$, versus those determined in the $j : 5p^2 \ ^3P_0 \rightarrow 5p6s \ ^3P_1$ transition. The experimental uncertainties are smaller than the dots. Open circles indicate ground-states while full circles represent isomeric states.

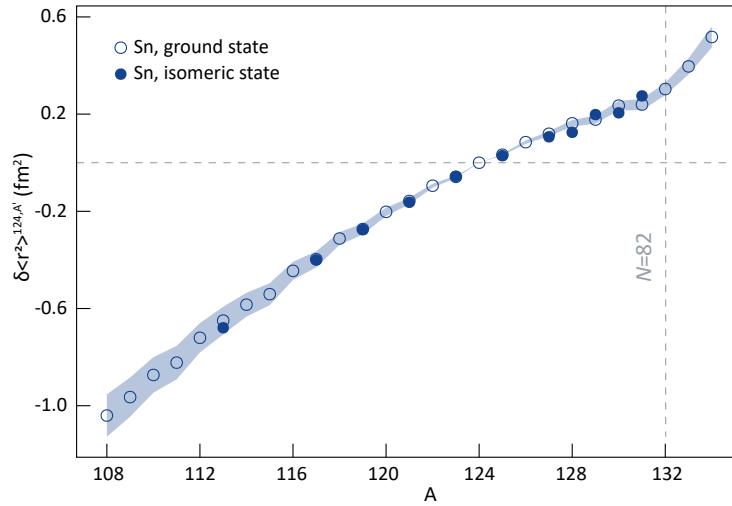


Figure 4.15: Differences in mean square charge radii of tin isotopes determined in the $5p^2 \ ^3P_0 \rightarrow 5p6s \ ^3P_1$ transition. Statistical errors are smaller than the symbols. Systematic uncertainties are indicated by an “error band” enclosing the experimental points.

Table 4.6: Changes in mean square nuclear charge radii of tin isotopes determined in the $5p^2 \ ^1S_0 \rightarrow 5p6s \ ^1P_1$ and $5p^2 \ ^3P_0 \rightarrow 5p6s \ ^3P_1$ transitions, respectively. Statistical errors are quoted in round brackets while systematic errors are in square brackets. Asterisks refer to isomeric states.

$N + Z$	I	Changes in mean square nuclear charge radii $\delta\langle r^2 \rangle^{A,A'}$ (fm)		
		$5p^2 \ ^1S_0 \rightarrow 5p6s \ ^1P_1$	$5p^2 \ ^3P_0 \rightarrow 5p6s \ ^3P_1$	Literature values [86]
108	0		-1.0404 (32) [872]	
109	5/2	-0.9670 (6) [599]	-0.9645 (6) [808]	
110	0		-0.8734 (25) [732]	
111	7/2		-0.8227 (12) [690]	
112	0	-0.7197 (6) [599]	-0.7205 (19) [604]	-0.7212 (73)
113	1/2	-0.6585 (23) [564]	-0.6497 (89) [570]	
113*	7/2	-0.6774(5) [563]	-0.6792 (13) [569]	
114	7/2	-0.5833 (6) [485]	-0.5842 (21) [490]	-0.5877 (73)
115	0	-0.5379 (4) [447]	-0.5409 (9) [453]	
116	1/2	-0.4458 (3) [371]	-0.4450 (27) [373]	-0.4417 (73)
117	1/2	-0.3981 (3) [331]	-0.3973 (14) [333]	-0.3871(79)
117*	11/2	-0.4020 (4) [331]	-0.4002 (16) [333]	
118	0	-0.3158 (7) [263]	-0.3120 (23) [262]	-0.3176 (73)
119	1/2	-0.2721 (4) [227]	-0.2731 (9) [229]	-0.2684 (79)
119*	11/2	-0.2757 (6) [227]	-0.2750 (15) [229]	
120	0	-0.1991 (3) [166]	-0.2022 (27) [170]	-0.1996 (79)
121	3/2	-0.1558 (14) [135]	-0.1576 (13) [137]	
121*	11/2	-0.1625 (8) [135]	-0.1627 (7) [136]	
122	0	-0.0941 (4) [78]	-0.0946 (25) [80]	-0.0962 (79)
123	3/2	-0.0580 (8) [48]	-0.0581 (10) [49]	
123*	11/2	-0.0556 (10) [48]	-0.0564 (16) [49]	
125	3/2	0.0341 (4) [29]	0.0329 (8) [28]	
125*	11/2	0.0307 (9) [29]	0.0289 (13) [28]	
126	0	0.0859 (3) [72]	0.0846 (23) [71]	
127	3/2	0.1178 (9) [98]	0.1192 (11) [101]	
127*	11/2	0.1091 (19) [99]	0.1066 (24) [101]	
128	0	0.1624 (9) [136]	0.1621 (16) [137]	
128*	7	0.1485 (29) [136]	0.1251 (20) [140]	
129	3/2	0.1773 (15) [167]	0.1776 (16) [168]	
129*	11/2	0.1982 (12) [166]	0.1980 (10) [167]	
130	0	0.2387 (6) [199]	0.2348 (13) [198]	
130*	7	0.2088 (8) [201]	0.2053 (16) [199]	
131	3/2	0.2385 (8) [230]	0.2394 (10) [234]	
131*	11/2	0.2732 (6) [228]	0.2749 (7) [232]	
132	0	0.3055 (4) [255]	0.3033 (11) [256]	
133	7/2	0.3984 (6) [329]	0.3964 (10) [333]	
134	0	0.5083 (13) [423]	0.5174 (25) [434]	

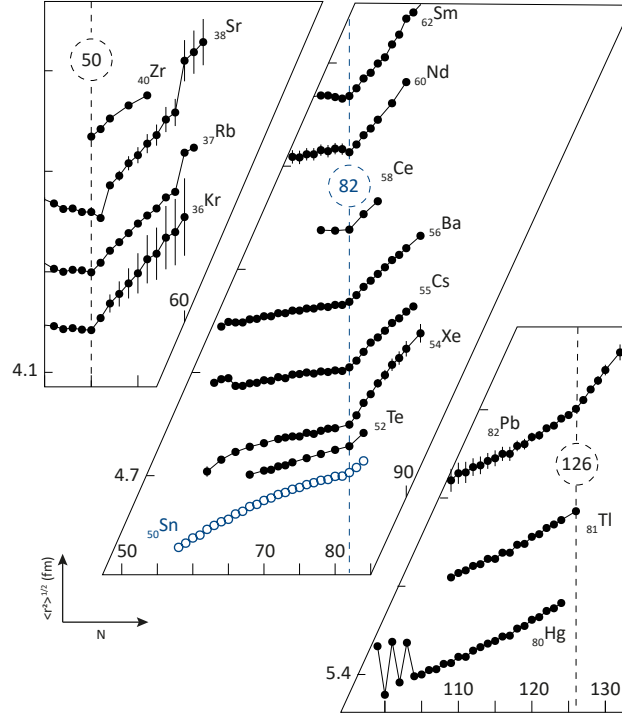


Figure 4.16: Experimental root mean-square charge radius versus neutron number around closed-shells. The values represented by black circles were taken from [82] while blue circles correspond to the values extracted from this work. Only ground states are plotted. The data have been arbitrarily offset from each other for clarity

The radii of the ground states increase smoothly with the neutron number from $N = 58$ to the shell closure with a parabolic shape and an odd-even staggering on top of a linear trend. This behavior is analogous to the one observed in the neighboring elements [50, 84] and it is well described by the droplet model until the shell closure where a sudden change in the slope is observed. This “kink” is the most striking characteristic of the charge radii, evidencing a shell effect, observed before at $N = 50, 82$ and 126 as evident in Fig. 4.16, but there was no experimental evidence on tin before this thesis.

The radii of the isomeric states almost coincide with the ones from the ground states around $N = 70$ and slightly deviate from them near the closed shell. The magnitude of this differences, when the unique-parity $h_{11/2}$ orbital is involved, in particular, requires a closer investigation. In order to reveal the finer details,

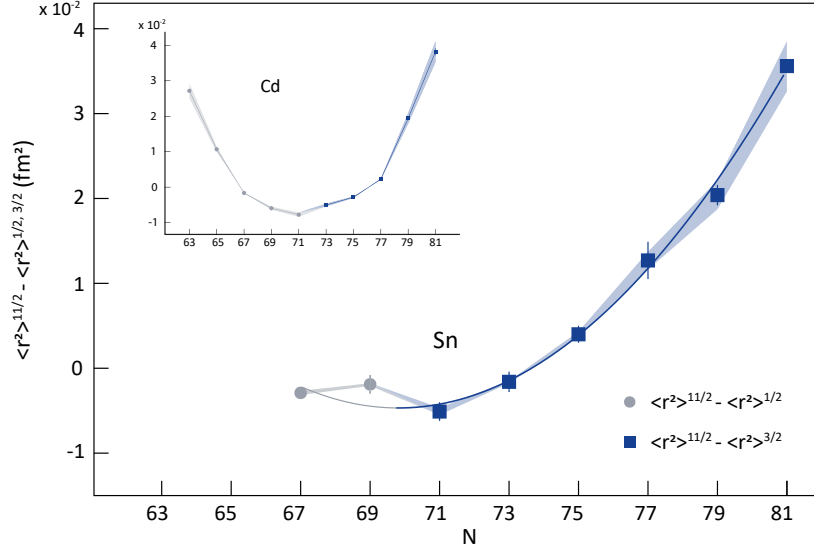


Figure 4.17: Differences in mean square charge radius between 11/2 states and 1/2, 3/2 states. The systematic error is represented by shaded bands. The inset shows a similar mass dependence of the same states in the neighbouring cadmium chain.

the latter are displayed as a function of N in Fig. 4.17. The overall picture is described by a parabolic trend, centered around $N = 70$. The charge radii of the 11/2 states are larger at the shell border and smaller than the 1/2 or 3/2 states at the mid-shell. The 11/2 states become the ground state around the mid-shell (from $N = 73$ up to $N = 77$) and the parabolic trend seems to survive. Below $N = 67$ the 11/2 states are short-lived; therefore it is unknown if the trend continues, where additionally the spin of the ground state change from 3/2 to 1/2. A similar interesting behavior has been observed before only along the cadmium chain where the 11/2 states are also present. For cadmium, the differences in charge radius between 11/2 states and 1/2 or 3/2 states were interpreted, based in (2.39), as a consequence of a linear increase of the deformation parameter (β) of the 11/2 states, assuming that the low-spin state is approximately spherical. The same approach for the observed trend in tin is under further investigation.

In Fig. 4.18, the experimental values of the mean square charge radii are compared to theoretical calculations computed at the beyond mean-field level, within the framework of the five-dimensional collective Hamiltonian (5DCH)

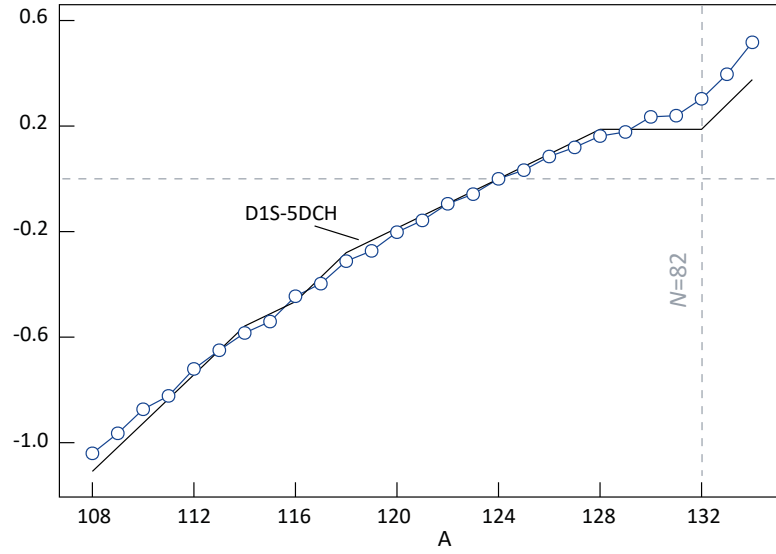


Figure 4.18: Comparison of mean square charge radii changes from this work (open circles) to the theoretical calculation of the even tin isotopes.

grounded in the generator coordinate method (GCM) with the gaussian overlap approximation (GOA) [87]. The calculation reproduces the experimental curvature and clearly shows the kink at the magic neutron number. Within this theoretical approach, the kink is related to the correlations stemming from the fluctuations of the quadrupole moments. Different calculations applying a new density functional of the Fayans type, that has been used to reproduce the trend in cadmium [88] isotopes, are in progress.

Chapter 5

Conclusions

Nuclear properties of neutron-rich tin isotopes towards and beyond the $N = 82$ shell closure have been investigated by high-resolution collinear laser spectroscopy. The hyperfine structures and isotope shifts over the range from ^{108}Sn up to ^{134}Sn were measured employing the COLLAPS instrumentation at ISOLDE, CERN. Two independent experiments using transitions with complementary properties, respectively at 452-nm and 286-nm, studied the $5p6s\ ^1P_1$ and the $5p6s\ ^3P_1$ levels in the neutral atom. A self-consistent analysis of the two datasets, linked by the common nuclear parameters, allowed the determination of nuclear spins, electromagnetic moments and charge radii with higher precision. The ground state properties of the more exotic isotopes ^{133}Sn and ^{134}Sn were assessed for the first time as well as the long-lived isomers in $^{113,123,128}\text{Sn}$.

The doubly-magic-plus-one-neutron nucleus ^{133}Sn was found to have the closest magnetic moment to the corresponding Schmidt value, suggesting a possible closed-shell structure of its ground state for which the single particle model can be considered as a fair approximation. The spin $I = 7/2$ is confirmed in our measurements. The nuclear properties of this isotope give valuable insight for future development of accurate shell-model interactions in the region.

The magnetic moments in this region seems to be sensitive to second-order core polarization effects. That is illustrated in the sequence of the $11/2$ moments which are found to be closer to the Schmidt value than those in the

neighbouring isotopes with two holes inside and two protons outside the shell closure. The magnetic moments of this state in particular have almost identical values, though first-order core polarization effects should be taken into account for an accurate description of the observed trend. An interesting behaviour is revealed by their quadrupole moments, which show a nearly linear mass dependence that acts well even beyond the natural capacity of the $h_{11/2}$ shell. A small effective charge suggests a spherical core with no considerable influence in the quadrupole moments as expected for a semi-magic nucleus. For an accurate interpretation of the observed effects, large-scale shell model calculations are necessary.

The differences in mean square charge radii beyond the shell closure $N = 82$ have been determined for the first time. The most striking behaviour is the observed “kink” at $N = 82$ that evidence the robustness of the $N = 82$ shell gap. Beyond mean-field calculations, triggered by the results of this work, provide accurate description of the radii and further relate the overall trend to correlations stemming from the fluctuations of the quadrupole moments. The measured differences in mean square charge radii between $11/2$ states and the other state present in the isotope are characterized by a parabolic behaviour. This trend seems to survive regardless if the $11/2$ states are ground or isomeric states.

Bibliography

- [1] M. G. Mayer, J. H. Jensen, *John Wiley & Sons* (1955).
- [2] H. Horie, A. Arima, *Phys. Rev.* **99**, 778 (1955).
- [3] D. T. Yordanov, *et al.*, *Phys. Rev. Lett.* **110**, 192501 (2013).
- [4] G. Neyens, *Rep. Prog. Phys.* **66**(4), 633 (2003).
- [5] M. Anselment, *et al.*, *Phys. Rev. C* **34**, 1052 (1986).
- [6] F. Dimmling, *et al.*, *Phys. Lett. B* **55**, 293 (1975).
- [7] J. Eberz, *et al.*, *Z. Phys. A* **326**, 121 (1987).
- [8] F. L. Blanc, *et al.*, *Phys. Rev. C* **72**, 034305 (2005).
- [9] K. L. Jones, A. S. Adekola, D. W. Bardayan, J. C. Blackmon, *Nature* **465**, 454 (2010).
- [10] P. Baumann, A. Huck, A. Knipper, G. Walter, *Hyp. Interact.* **129**, 141 (2000).
- [11] P. Campbell, I. Moore, M. Pearson, *Prog. Part. Nucl. Phys.* **86**, 127 (2016).
- [12] G. A. Lalazissis, *et al.*, *At. Data Nucl. Data Tables* **71**, 1 (1999).
- [13] S. Goriely, *et al.*, *At. Data Nucl. Data Tables* **77**, 311 (2001).
- [14] B. Cheal, K. T. Flanagan, *J. Phys. G: Nucl. Part. Phys.* **37**(11), 113101 (2010).
- [15] R. Neugart, *et al.*, *J. Phys. G: Nucl. Part. Phys.* **44**(6), 064002 (2017).
- [16] E. Schrödinger, *Phys. Rev.* **28**, 1049 (1926).
- [17] L. H. Thomas, *Nature* **117**, 514 (1926).

-
- [18] N. V. Polyanin, A., *Handbook of Linear Partial Differential Equations for Engineers and Scientists*. New York: Chapman and Hall/CRC (2016).
- [19] D. R. Yarkony, *Modern Electronic Structure Theory*. World Scientific Publishing Company (1995).
- [20] D. R. Hartree, *Mathematical Proceedings of the Cambridge Philosophical Society* **24**(1), 89–110 (1928).
- [21] V. Fock, *Z. Phys.* **61**(1), 126 (1930).
- [22] W. Pauli, *Z. Phys.* **31**, 765 (1925).
- [23] H. N. Russell, F. A. Saunders, *ApJ* **61**, 38 (1925).
- [24] H. Yukawa, *Proceedings of the Physico-Mathematical Society of Japan. 3rd Series* **17**, 48 (1935).
- [25] H. A. Bethe, *Phys. Rev.* **57**, 260 (1940).
- [26] L. S. Kisslinger, *Phys. Rev.* **104**, 1077 (1956).
- [27] M. G. Mayer, *Phys. Rev.* **74**, 235 (1948).
- [28] M. G. Mayer, *Phys. Rev.* **75**, 1969 (1949).
- [29] P. J. Mohr, B. N. Taylor, D. B. Newell, *Rev. Mod. Phys.* **84**, 1527 (2012).
- [30] W. Pierre, *J. Phys. Theor. Appl.* **6**, 661 (1907).
- [31] L. Kadanoff, *J. Stat. Phys.* **137** (2009).
- [32] R. D. Woods, D. S. Saxon, *Phys. Rev.* **95**, 577 (1954).
- [33] B. Castel, I. Towner, *Modern Theories of Nuclear Moments*. Clarendon Press, Oxford (1990).
- [34] K. Heyde, *The Nuclear Shell Model*. 2nd ed., Springer, Berlin Heidelberg (1994).
- [35] A. de Shalit, I. Talmi, *Nuclear Shell Theory* (1963).
- [36] M. G. Mayer, *Phys. Rev.* **78**, 16 (1950).
- [37] P. Ring, P. Schuck, *The Nuclear Many Body Problem* (1980).
- [38] D. Poenaru, W. Greiner, *Handbook of Nuclear Properties* (1996).
- [39] A. Bohr, B. Mottelson, *Nuclear Structure*, vol. I (1969).

-
- [40] C. F. V. Weizsäcker, *Z. Phys.* **96**(7), 431 (1935).
- [41] N. S. Gösta, I. Ragnarsson, *Shapes and Shells in Nuclear Structure*, vol. I (1995).
- [42] M. G. Gustavsson, A. Mårtensson-Pendrill, *Four Decades of Hyperfine Anomalies*, vol. 30 of *Advances in Quantum Chemistry*. Academic Press (1998).
- [43] R. Neugart, G. Neyens, *Nuclear Moments*, pp. 135–189. Springer Berlin Heidelberg, Berlin, Heidelberg (2006).
- [44] K. S. Krane, *Introductory Nuclear Physics*. Wiley, 1 edn. (1987).
- [45] P. C. Magnante, H. H. Stroke, *J. Opt. Soc. Am.* **59**, 836 (1969).
- [46] G. W. I.I. Sobel'man, D. ter Haar (Auth.), *Introduction to the Theory of Atomic Spectra*. Pergamon Press (1972).
- [47] H. Kopfermann, E. E. Schneider, *Nuclear Moments*. Academic Press Inc. (1958).
- [48] <https://stfc.ukri.org>.
- [49] W. H. King, *Isotope Shifts in Atomic Spectra* (1984).
- [50] M. Hammen, *Ph.D. thesis: Spins, Moments and Radii of Cd Isotopes* (2013).
- [51] E. C. Seltzer, *Phys. Rev.* **188**, 1916 (1969).
- [52] <http://isolde.web.cern.ch/>.
- [53] M. Lindroos, *Review of the ISOL Method* (2018).
- [54] <https://home.cern/>.
- [55] R. Catherall, J. Lettry, S. Gilardoni, U. Köster, *Nucl. Instrum. Methods Phys. Res.* **204**, 235 (2003).
- [56] V. Fedosseev, *et al.*, *J. Phys. G: Nucl. Part. Phys.* **44**(8), 084006 (2017).
- [57] U. Köster, *et al.*, *Nucl. Instrum. Methods Phys. Res.* **266**, 4229 (2008).
- [58] E. Kugler, *Hyp. Interact.* **129**(1), 23 (2000).
- [59] E. Mané, *et al.*, *EPJA* **42**(3), 503 (2009).
- [60] K. D. Kreim, *PhD Thesis: Collinear Laser Spectroscopy of Potassium: Nuclear Charge Radii beyond $N = 28$* . (2013).

-
- [61] M. Borge, Y. Kadi, *Nucl. Phys. News* **26**(4), 6 (2016).
- [62] A. Herlert, *Nucl. Phys. News* **20**(4), 5 (2010).
- [63] M. Borge, *Nucl. Instrum. Methods Phys. Res.* **376**, 408 (2016).
- [64] J. Papuga, *et al.*, *Phys. Rev. Lett* **110** (2013).
- [65] N. Bendali, *et al.*, *J. Phys. B* **19**(2), 233 (1986).
- [66] K. Kreim, *et al.*, *Phys. Lett. B* **731**, 97 (2014).
- [67] <https://www.coherent.com>.
- [68] <http://www.sirah.com/matisse-ds>.
- [69] <http://www.sirah.com/matisse-ts>.
- [70] <http://www.sirah.com/wavetrain-2>.
- [71] G. Audi, *et al.*, *Chinese Phys. C* **36**(12), 1157 (2012).
- [72] K. R. Anton, *et al.*, *Phys. Rev. Lett.* **40**, 642 (1978).
- [73] H. J. Beyer, H. Kleinpoppen, *Collinear Laser Spectroscopy on Fast Atomic Beams*. Progress in Atomic Spectroscopy: Part D. (1987).
- [74] T. Ida, M. Ando, H. Toraya, *J. Appl. Cryst* **33** (2000).
- [75] G. K. Wertheim, M. A. Butler, K. W. West, D. N. E. Buchanan, *Rev. Sci. Instrum.* **45**(11), 1369 (1974).
- [76] R. Brun, F. Rademakers, *Nucl. Instrum. Methods Phys. Res.* **389**(1), 81 (1997), New Computing Techniques in Physics Research V.
- [77] F. James, *Rev. Sci. Instrum.* p. 38 (1994).
- [78] A. Bohr, V. F. Weisskopf, *Phys. Rev.* **77**, 94 (1950).
- [79] J. R. Persson, *At. Data Nucl. Data Tables* **99**, 62 (2013).
- [80] W. G. Proctor, *Phys. Rev.* **79**, 35 (1950).
- [81] Y. Lei, *et al.*, *Phys. Rev. C* **92** (2015).
- [82] G. Fricke, K. Heilig, *Group I: Elementary Particles, Nuclei and Atoms* **20** (2004).
- [83] J. Eberz, *et al.*, *Nucl. Phys. A* **464**(1), 9 (1987).

-
- [84] K. Heyde, *Hyp. Interact.* **43**, 15 (1988).
- [85] P. W. Zhao, S. Q. Zhang, J. Meng, *Phys. Rev. C* **89**(1), 011301 (2014).
- [86] C. Piller, *et al.*, *Phys. Rev. C* **42**, 182 (1990).
- [87] J. Liber, M. Girod, J. P. Delaroche, *Phys. Rev. C* **60**, 121 (1999).
- [88] M. Hammen, *et al.* Submitted to *Phys. Rev. C*.
- [89] B. Brown, W. Rae, *Nuclear Data Sheets* **120** (2014).
- [90] W. Rae, <http://www.garsington.eclipse.co.uk>.
- [91] B. H. Brown, B. Wildenthal, *Annu. Rev. Nucl. Part. Sci.* **38** (1988).
- [92] B. A. Brown, W. A. Richter, *Phys. Rev. C* **74** (2006).
- [93] J. Krämer, *et al.*, *Physics Letters B* **678**(5), 465 (2009).
- [94] D. T. Yordanov, *et al.*, *J. Phys. G: Nucl. Part. Phys.* **44**(7), 075104 (2017).
- [95] F. Alder, F. C. Yu, *Phys. Rev.* **82**, 105 (1951).
- [96] M. Kowalska, *et al.*, *Phys. Rev. C* **77** (2008).

High-resolution laser spectroscopy of the neutron-rich tin isotopes

Results of experiment IS573

Liss Vazquez Rodriguez
for the COLLAPS-ISCOOL collaboration

The IS573 experiment aimed to provide charge radii and electromagnetic moments of ground and isomeric states along the isotopic chain of tin. The program included two independent measurements dedicated to different transitions in the neutral atom. Excitations from the ground state at 286-nm resolved the magnetic moment while the 452-nm transition from a metastable state improved the sensitivity to the quadrupole moment. Both measurements constitute a data set which is being analyzed self consistently in order to obtain the highest possible accuracy for all the parameters.

A major goal of IS573 was to propagate the study of tin beyond the $N = 82$ shell closure in order to observe a possible shell effect in the charge radii which may or may not be present according on various mean-field calculations. Another primary motivation was the study of the quadrupole moments and isomer shifts associated with the unique-parity $h_{11/2}$ orbital known to have a simple mass dependence in the cadmium analogues. In addition, from a shell-model perspective, the study of the doubly-magic-plus-one-neutron nucleus ^{133}Sn is considered important due to the anticipated single-particle nature of its ground state.

Hyperfine spectra were observed for all species up to ^{134}Sn (see spectrum in 5.1) which enables us to tackle the points mentioned above. Furthermore, the electromagnetic moments and charge radii of the long-lived isomers in

High-resolution laser spectroscopy of the neutron-rich tin isotopes

Results of experiment IS573

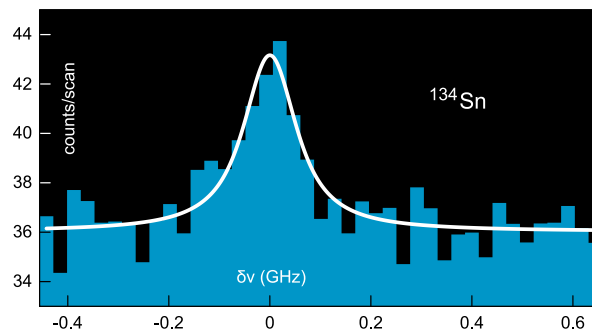
Liss Vazquez Rodriguez
for the COLLAPS-ISCOOL collaboration

Figure 5.1: Fluorescence spectrum of ^{134}Sn in the 286-nm transition in the neutral atom.

$^{113,123,128}\text{Sn}$ have been assessed for the first time. Tin has been the subject of multiple studies throughout the years. With respect to former laser spectroscopy experiments [1-3] we have been able to benefit from a number of improvements. The radioactive beams of tin at ISOLDE have been selectively laser ionized, thus aiding the suppression of contaminants, and subsequently bunched for a 10000-fold background suppression in the fluorescence spectra. Furthermore, our measurements were implemented in a collinear geometry, therefore with the highest possible resolution limited fundamentally by the natural linewidth. Simultaneous analysis of the two transitions, being linked by the common nuclear parameters, allows their extraction with higher precision. The overall accuracy of the quadrupole moments will be improved further due to a dedicated computational study of the electric field gradient in the relevant atomic states.

[1] M. Anselment *et al.*, *Phys. Rev. C* **34**, 1052 (1986).

[2] J. Eberz *et al.*, *Zeitschr. f. Phys. A* **326**, 121 (1987).

[3] F. Le Blanc *et al.*, *Phys. Rev. C* **72**, 034305 (2005).

Nuclear charge radii of even neutron-rich tin isotopes

C. Gorges¹, L. V. Rodriguez², M. L. Bissel^{3,4}, K. Blaum⁵, J.-P. Ebran⁶, R. F. Garcia Ruiz^{3,4}, W. Gins³, H. Heylen^{5,7}, S. Kaufmann⁸, M. Kowalska⁷, S. Malbrunot-Ettenauer⁷, W. Nazarewicz⁹, R. Neugart^{1,5}, G. Neyens³, W. Nörtershäuser⁸, P.-G. Reinhard¹⁰, R. Sá nchez¹¹, S. Schmidt¹², Z. Y. Xu³, D. T. Yordanov^{2,*}

¹*Institut für Kernchemie, Universität Mainz, D-55128 Mainz, Germany*

²*Institut de Physique Nucléaire, CNRS-IN2P3, Université Paris-Sud, Université Paris-Saclay, 91406 Orsay, France*

³*KU Leuven, Instituut voor Kern- en Stralingsfysica, B-3001 Leuven, Belgium*

⁴*School of Physics and Astronomy, The University of Manchester, Manchester, M13 9PL, United Kingdom*

⁵*Max-Planck-Institut für Kernphysik, D-69117 Heidelberg, Germany*

⁶*CEA, DAM, DIF, F-91297 Arpajon, France*

⁷*Experimental Physics Department, CERN, CH-1211 Geneva 23, Switzerland*

⁸*Institut für Kernphysik, Technische Universität Darmstadt, D-64289 Darmstadt, Germany*

⁹*Department of Physics and Astronomy and FRIB Laboratory, Michigan State University, East Lansing, Michigan 48824, USA*

¹⁰*Institut für Theoretische Physik II, Universität Erlangen-Nürnberg, 91058 Erlangen, Germany*

¹¹*GSI Helmholtzzentrum für Schwerionenforschung, D-64291 Darmstadt, Germany*

¹²*Institut für Kernchemie, Universität Mainz, D-55128 Mainz, Germany*

Abstract

The change in mean square nuclear charge radii of the even tin isotopic chain $^{108-134}\text{Sn}$ has been investigated by means of collinear laser spectroscopy at ISOLDE using the atomic transitions $5p^2\ ^1S_0 \rightarrow 5p6s\ ^1P_1$ and $5p^2\ ^3P_0 \rightarrow 5p6s\ ^3P_1$. With the determination of the charge radius of ^{134}Sn and the improvement in the accuracy for most of the neutron-rich isotopes the evolution of the charge radii across the $N = 82$ shell closure is established. A kink in the evolution of the nuclear charge radii at this neutron shell closure is well established in this mass region. The observed more pronounced kink in Sn compared to its neighboring elements can be well explained by theoretical models obtained by an Energy Density Functional (EDF) approach presented in this paper.

Introduction

The $Z = 50$ element tin owns more stable isotopes than any other element and far away from stability the two doubly magic isotopes ^{100}Sn and ^{132}Sn can be found. It is a key element for both theoretical and experimental understanding of nuclear physics [1-4]. Reasons for this are the closed proton shell that is advantageous for nuclear structure calculations and especially the $N = 82$ neutron closure at ^{132}Sn in the middle of a region that is extremely important for the nuclear astrophysics and nucleosynthesis, as well as the many optically accessible transitions that allow laser spectroscopic measurements with high precision. Laser spectroscopic and muonic measurements have been performed from ^{108}Sn to ^{132}Sn , partially with low accuracy, determining the nuclear charge radii up to the doubly magic nucleus [5-9]. Radii across the $N = 82$ shell closure have been measured only for elements with higher proton numbers. They exhibit a clear kink at the neutron shell closure that is very pronounced at higher proton numbers but weakening towards the proton shell closure (see e.g. [10,11]). Recently, a new density functional of the Fayans type has been established to explain the strong increase of charge radii in the calcium region. Surprisingly this functional performs very well for Cd isotopes where experimental data is available almost for the complete shell

but not across the $N = 82$ shell closure [12]. Newly developed calculations based on an Energy Density Functional (EDF) approach [13] for Sn lead to the expectation of a more pronounced kink than in the neighboring elements. Also mass measurements that have already been performed beyond the magic neutron number $N = 82$ [14-16]. revealed a very strong $N = 82$ -shell gap in tin compared with the neighboring elements. However, at the next classical neutron shell closure $N = 126$ a similar situation exists, and it has been shown that a very strong shell gap, namely at ^{208}Pb , can be linked to a weakening of the kink in the evolution of the nuclear charge radius [17]. This raises the expectation of a weak kink in the evolution of the charge radii of the tin isotopic chain. Whereas recent results obtained with a Fayans functional predicts a strong kink in the Cd chain, two protons below $Z = 50$. The charge radii extracted from the laser spectroscopic data exhibit a very pronounced kink and therefore confirm the theoretical predictions. Since the arguments established in the Pb region this would indicate a quenching of the shell closure in disagreement with the measured binding energies. Hence, a different mechanism must be at work at $N = 82$.

Experiment

Collinear laser spectroscopy has been performed at neutron-rich tin isotopes using the atomic transitions $5p^2\ ^1S_0 \rightarrow 5p6s\ ^1P_1$ (SP, 452.5 nm) and $5p^2\ ^3P_0 \rightarrow 5p6s\ ^3P_1$ (PP, 286.3 nm) at the COLLAPS experiment situated at ISOLDE CERN. Details of the setup are described elsewhere [18]. Briefly, protons from the proton synchrotron booster (PSB) with an energy of 1.4 GeV and beam currents of up to $2\ \mu\text{A}$ hit a neutron converter [19] close to a uranium carbide (UC_x) target. Neutron induced fission provides an efficient production of tin isotopes that are subsequently ionized using resonant laser ionization [20]. The tin ions are accelerated to an energy of about 40 keV, mass separated and transported to the radio frequency quadrupole cooler and buncher ISCOOL [21], where they are accumulated, cooled and ejected towards the COLLAPS beam line as an ion bunch of typically $5\ \mu\text{s}$ pulse length. The ion bunch is overlapped with a copropagating single-frequency laser beam. Charge exchange on sodium vapor was performed to populate the lower level

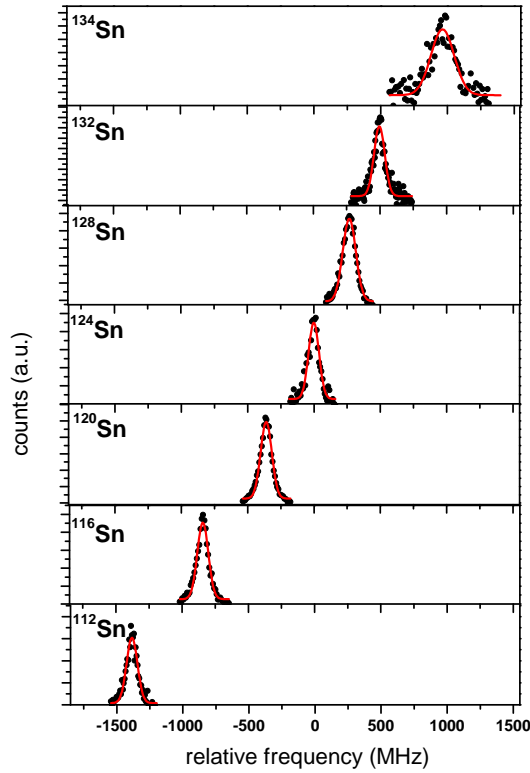


Figure 5.2: Optical spectra of some chosen isotopes for the determination of the isotope shift in the $5p^2\ ^1S_0 \rightarrow 5p6s\ ^1P_1$ transition. Shown is the number of counts as a function of the relative frequency.

of the observed transitions in atomic tin. The potential of the charge exchange region is varied to scan the laser frequency in the rest frame of the atom. In Fig. 5.2 a few of the obtained spectra are shown. For the determination of the isotope shift, the x-axis in this graph is already converted into relative frequencies. Optical detection of the PP transition is based on the fluorescence at 286 nm, while the SP transition is detected by the subsequent decay along the $5p6s\ ^1P_1 \rightarrow 5p^2\ ^1D_2$ transition at 326 nm which avoids optical pumping and acts as an efficient background suppression.

Linear polarized light is generated by a Ti:Sa ring laser which is frequency doubled and long term stabilized to a wavemeter that is regularly calibrated using a stabilized HeNe laser. A long term stability of better than 10 MHz/h is achieved. Reference scans of ^{124}Sn are carried out regularly between the

spectra.

Spectra were obtained from both transitions from the ground states of the even isotopes $^{112-134}\text{Sn}$ and in the PP transition also $^{108,110}\text{Sn}$ could be observed.

Results

All isotope shifts

$$\delta\nu^{124,A} = \nu_0^A - \nu_0^{124} = \frac{m_A - m_{124}}{m_A \cdot m_{124}} \cdot M + F \cdot \delta \langle r^2 \rangle^{124,A}, \quad (5.1)$$

with the field shift factor F and the mass shift factor M of the respective transition and the isotope masses m_A , are determined with respect to the isotope ^{124}Sn . Optical spectra were fitted using Voigt profiles with Lorentzian width fixed to the natural linewidth. The full width at half maximum obtained from fitting is below 100 MHz for all isotopes. Fitting with pure Lorentzian and Gaussian profiles resulted in the same centroids. In all cases the residuals are structureless and statistically fluctuating. Typical hints of asymmetric profiles due to the charge exchange processes [22] were not observed.

The largest uncertainties arise from the relative voltage uncertainties $\Delta U_{\text{acc}}/U_{\text{acc}} \approx \Delta U_{\text{offset}}/U_{\text{offset}} \approx 1.5 \times 10^{-4}$ of the starting potential U_{acc} at ISCOOL and the Doppler tuning voltage U_{offset} . The arising isotope shifts for $^{108-124}\text{Sn}$ resulting from our data are within the uncertainties in very good agreement with the values provided in [7]. A usual King plot analysis [23] was performed using muonic data as well as V-factors from electron elastic scattering provided in [11], and the isotope shifts measured here for both transitions individually. An additionally performed King plot analysis comparing the two investigated transitions showed that the extracted isotope shifts agree with each other and lead to the same nuclear charge radii. A detailed description of the procedure for the determination of the change in mean square nuclear charge radii can be found in [12] where an identical analysis was performed. The analysis performed here results in a field shift factor of $F_{SP} = 2.44(47)$ GHz/fm² for the SP transition which is in good agreement both with the experimental field shift factor $F_{King} = 2.24(27)$ GHz/fm² obtained in [7], where it is determined via a King plot analysis in different transitions, and with the fac-

tor of $F_{DF} = 1.98 \text{ GHz/fm}^2$ based on theoretical Dirac-Fock calculations also mentioned in [8]. There is a discrepancy to the factor $F = 3.29(20) \text{ GHz/fm}^2$ given in [11] that can easily be explained by the used reference values for the nuclear charge radii. The charge radii used in their analysis differ from the ones given in [11] which has of course a huge impact of the slope parameter in the King plot analysis.

The analysis of the King plot in the PP transition yielded in $F_{PP} = 2.88(60) \text{ GHz/fm}^2$ which is in agreement with both the Dirac-Fock value of $F_{DF} = 2.408 \text{ GHz/fm}^2$ and the deduced value of $F_{King} = 2.39(27) \text{ GHz/fm}^2$ given in [7]. The extracted field shift factor agrees also with the factor of $F = 3.3(3) \text{ GHz/fm}^2$ that is used in [6]. The mass shift factor results in $K_{SP} = -575(5) \text{ uGHz}$, and $K_{PP} = -506(5) \text{ uGHz}$ respectively. From both transition, changes in mean square nuclear charge radii were determined and the arising average values are listed in Table 5.1. The evolution of the nuclear charge radii of the even tin isotopes is also shown in Fig. 5.3. Clearly visible is a linear trend that is superimposed by a parabola. This behavior is considered by the droplet model and describes the data quite well until $N = 82$. Above this magic number, there is a kink showing a deviation from this behavior. Fig. 5.3 shows also the theoretical calculation for the change in mean square nuclear charge radii which describes the trend of the experimental values qualitatively and also shows the kink at the magic neutron number.

Theory

At a moderate computational cost, the framework of EDFs enables an accurate description of ground-state properties and collective excitations from relatively light systems to superheavy nuclei, and from the valley of β stability to the particle drip lines. The lowest order, i.e., the single-reference (SR) EDF also referred to as the mean-field approximation, involves Hartree-Fock-Bogoliubov (HFB) calculation of the binding energy surface with the mass multipole moments as constrained quantities - here the quadrupole axial and triaxial moments (Q_{20}, Q_{22}). The corresponding static nuclear mean-field is characterized by symmetry breaking: translational, rotational, and particle number, allowing to incorporate in a clever way important nondynamical correlations (e.g.,

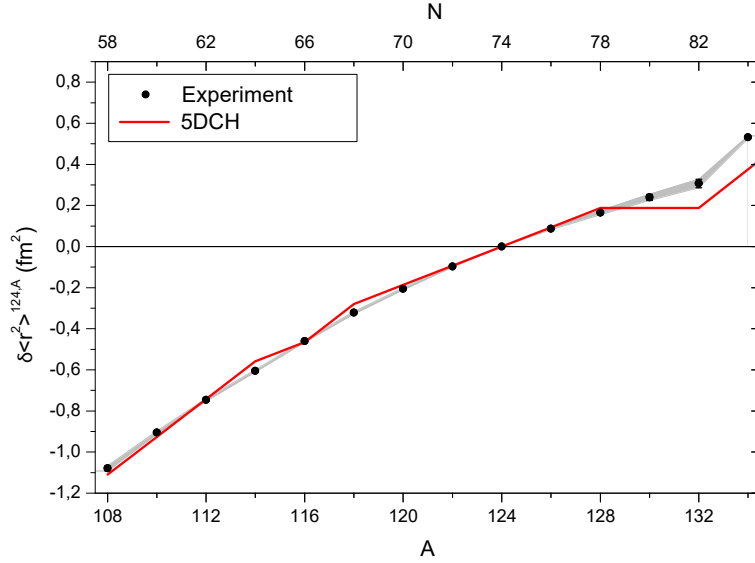


Figure 5.3: Evolution of the nuclear charge radii of the tin isotopic chain. Shown is the change in mean square nuclear charge radius $\delta \langle r^2 \rangle$ as a function of the mass number (lower x-axis), respectively the neutron number (upper x-axis). The red line shows the theoretical prediction.

angular and pairing ones). However, atomic nuclei being finite objects, its eigenstates do preserve the symmetries of the nuclear Hamiltonian such that the static self-consistent solution can only provide an approximate description of bulk ground-state properties such as masses and radii. Additional correlations related to restoration of broken symmetries and fluctuations in collective coordinates have to be accounted for in a post mean-field treatment. The approach used in this study to take into account five-dimensional quadrupole dynamics that restores rotational symmetry and allows for fluctuations around triaxial mean-field minima is the five-dimensional collective Hamiltonian (5DCH) grounded in the generator coordinate method (GCM) with the Gaussian overlap approximation (GOA) [24]. The charge radii of tin isotopes computed at the SR and 5DCH levels with the Gogny D1S parametrization [25] are displayed Fig. 5.3. At the SR level, the tin charge radii increase smoothly with the neutron number. One has to go to the 5DCH level in order to observe a sudden change in the slope of the charge radii versus neutron number around

Table 5.1: Isotope shifts $\delta\nu_{IS}^{124,A}$ and changes in mean square nuclear charge radii $\delta\langle r^2 \rangle^{124,A}$ for all even isotopes with mass number A in the $5p^2\ ^1S_0 \rightarrow 5p6s\ ^1P_1$ (SP) and the $5p^2\ ^3P_0 \rightarrow 5p6s\ ^3P_1$ (PP) transition. The first bracket shows the statistical uncertainty, the second bracket the systematical error. For the change in nuclear charge radii, the total uncertainties are given.

A	$\delta\nu_{SP,IS}^{124,A}$ (MHz)	$\delta\nu_{PP,IS}^{124,A}$ (MHz)	$\delta\langle r^2 \rangle^{124,A}$ (fm ²)
108		-2416.8 (118)(98)	-1.0791 (166)
110		-2015.2 (103)(84)	-0.9046 (108)
112	-1384.2 (22)(84)	-1652.1 (80)(71)	-0.7464 (68)
114	-1115.0 (19)(69)	-1335.6 (86)(58)	-0.6044 (52)
116	-842.9 (14)(55)	-1007.6 (92)(45)	-0.4604 (47)
118	-586.1 (11)(40)	-688.0 (76)(33)	-0.3220 (59)
120	-359.6 (13)(27)	-448.6 (93)(22)	-0.2059 (52)
122	-168.3 (16)(13)	-206.3 (84)(10)	-0.0967 (38)
126	148.0 (13)(13)	178.7 (69)(12)	0.0867 (47)
128	277.8 (23)(39)	339.5 (51)(21)	0.1651 (97)
130	393.6 (35)(67)	486.6 (44)(31)	0.2392 (151)
132	497.2 (11)(50)	624.1 (34)(42)	0.3071 (212)
134	980.1 (36)(62)	1196.5 (83)(51)	0.5322 (65)

the magic number $N = 82$. Within this approach, such a kink is hence related to the correlations stemming from the fluctuations of the quadrupole moments. Those correlations are maximal at mid-shell and drop to zero at a shell closure, explaining the slope change.

Conclusion

The changes in the mean square nuclear charge radius of the even tin isotopic chain $^{108-134}\text{Sn}$ have been determined by means of collinear laser spectroscopy. With the measurements of the most neutron-rich isotope ^{134}Sn we were able to determine a charge radius beyond the neutron shell closure for the first time. Below the neutron shell closure, the evolution of the charge radii can be described by simple droplet model considerations. The expected kink at $N = 82$ has been observed and it turned out that it is as expected by theory much more pronounced than for the neighboring elements.

This work has been supported by the Max-Planck Society, the German Federal Ministry for Education and Research under Contract Nos. 05P15RDCIA, the Helmholtz International Center for FAIR (HIC for FAIR) within the LOEWE

program by the State of Hesse, the Belgian IAP Project No. P7/12, the FWO-Vlaanderen, the European Union seventh framework through ENSAR under Contract No. 262010, We thank the ISOLDE technical group for their professional assistance.

*yordanov@ipno.in2p3.fr

† this work is part of the theses of C.G. and L.V., both have contributed in equal parts to this work

- [1] F. Dimmling *et al.*, *Phys. Lett.* **55B**, 293 (1975).
- [2] J. Dobaczewski *et al.*, *Nucl. Phys. A* **422**, 103 (1983).
- [3] R. Bhattacharya *et al.*, *Zeitschr. f. Phys. A* **349**, 101 (1994).
- [4] J. Libert *et al.*, *Nucl. Phys. A* **786**, 47 (2007).
- [5] P. E. G. Baird *et al.*, *Jour. of Phys. B* **16**, 2485 (1983).
- [6] M. Anselment *et al.*, *Phys. Rev. C* **34**, 1052 (1986).
- [7] J. Eberz *et al.*, *Zeitschr. f. Phys. A* **326**, 121 (1987).
- [8] C. Piller *et al.*, *Phys. Rev. C*, **42** 182 (1990).
- [9] F. Le Blanc *et al.*, *Phys. Rev. C* **72**, 034305 (2005).
- [10] W. Borchers *et al.*, *Phys. Lett. B* **216**, 7 (1989).
- [11] G. Fricke and K. Heilig, *Nuclear Charge Radii* , Group I: Elementary Particles, Nuclei and Atoms Volume 20 (Springer, 2004).
- [12] M. Hammen *et al.*, submitted to *Phys. Rev. Lett.* (2018).
- [13] M. Bender *et al.*, *Rev. Mod. Phys.* **75**, 121 (2003).
- [14] M. Dworschak *et al.*, *Phys. Rev. Lett.* **100**, 072501 (2008).
- [15] J. Hakala *et al.*, *Phys. Rev. Lett.* **109**, 032501 (2012).
- [16] D. Atanasov *et al.*, *Phys. Rev. Lett.* **115**, 232501 (2015).

- [17] P. Campbell *et al.*, *Progr. in Part. and Nucl. Phys* **86**, 127 (2016).
- [18] A. Müller *et al.*, *Nucl. Phys. A* **403**, 234 (1983).
- [19] R. Catherall *et al.*, *Nucl. Instr. Meth. Phys. Res. B* **204**, 235 (2003).
- [20] B. A. Marsh, *Rev. of Sc. Instr.* **85**, 02B923 (2014).
- [21] E. Mané *et al.*, *Eur. Phys. Jour. A* **42**, 503 (2009).
- [22] H. Bendali *et al.*, *J. Phys. B* **19**, 233 (1986).
- [23] W. H. King, Proceedings of the Royal Society of London Series A **280**, 430 (1964).
- [24] J. Libert *et al.*, *Phys. Rev. C* **60** , 054301 (1999).
- [25] J.-F. Berger *et al.*, *Comput. Phys. Commun.* **63**, 365 (1991).

Appendix

“Other work: Shell model calculations for Mg”

The shell model is used to investigate the magnetic moments of odd magnesium isotopes with neutron number up to 17. The calculations were carried out using the NuShellX @ MSU [89,90] code that provides a powerful tool for nuclear structure predictions. The latter are based on the *sd* residual interactions USD [91] and USDA/B [92] involving the $0d_{3/2}, 0d_{5/2}$ and $1s_{1/2}$ active orbitals for protons and neutrons. They have been obtained from the fits of two-body matrix elements (TBME) and single-particle energies to experimental binding and excitation energies. USDA/B are an updated version of the USD with the main difference in terms of energy associated to the neutron-rich nuclei. USDB, in particular, provides the best fit to the data.

The theoretical results from this work are listed in Tab. 5.2. The overall agreement between the calculations and the experimental values is reasonably good with differences smaller than 10%.

Regarding energy levels, the USDB interaction provides the most accurate description of the level ordering in ^{29}Mg . The comparison between the experimental ground state and theoretical values are shown in Fig. 5.4. According to the single-particle shell model, the ground state properties are dominated by one single neutron in the $d_{3/2}$ shell which is in agreement with the $I = 3/2^+$ spin-parity, measured experimentally [96]. From the shell model calculations using the USD/USDA Hamiltonian the $3/2^+$ is an excited state located at 40/

Table 5.2: Calculated magnetic moments from this work. The experimental values listed in the second column are taken from [93–96].

N+Z	I π	$\mu(\mu_N)$				
		Schmidt	Exp	USD	USDA	USDB
21	5/2 ⁺	-1.913	-0.98300 (700)	-0.96780	-0.83900	-0.84810
23	3/2 ⁺	-1.913	-0.53660 (30)	-0.51590	-0.42400	-0.40970
25	5/2 ⁺	-1.913	-0.85545 (7)	-0.90860	-0.84820	-0.84870
27	1/2 ⁺	-1.913	-0.41100 (200)	-0.42060	-0.35330	-0.41190
29	3/2 ⁺	1.146	0.97800 (60)	0.95340	1.05800	1.07100

90 keV. It becomes the ground state only when the USDB interaction is taken into account. Conversely, the USD Hamiltonian provide a better description of the magnetic moment which also occurs in other isotones with one unpaired neutron in the shell [96].

Although the three Hamiltonians seem to adequately describe the magnesium isotopes, somewhat better results are obtained with USD for the neutron-deficient isotopes and USDB for the neutron-rich which is consistent with the fact that the USDB Hamiltonian includes more recent experimental data for the neutron-rich nuclei in the relevant shell. Fig. 5.5 illustrates the experimental moments versus the calculated values that best approach the experimental data.

Shell model analysis using the USD Hamiltonian for the neutron-deficient isotopes:

- ²¹Mg. The major contribution to the wave function of 59% is given by the protons and neutrons coupled to spin 0 and 5/2, respectively. Inside this contribution, about 42% corresponds to the one predicted by the single-particle shell model with a single neutron in the $d_{5/2}$ shell and four protons in the same orbit.
- ²³Mg. The calculation reproduces the experimental moment with differences smaller than 4%, see Tab. 5.2. The recent determination of a negative sign for the magnetic moment [94] infers the contribution of the $d_{5/2}$ orbital in the 3/2 ground state configuration of this isotope. Indeed, in the calculations, the $d_{5/2}$ orbital is dominant with about 75%

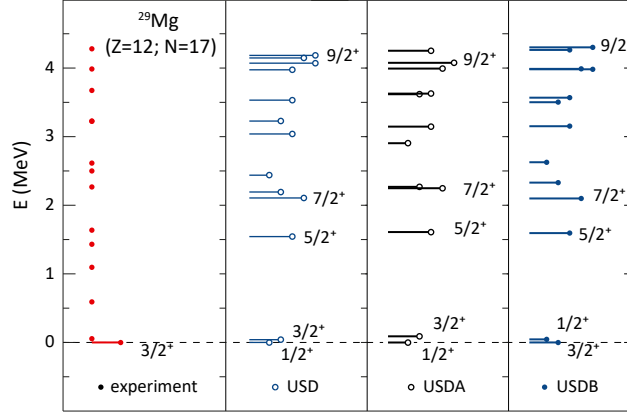


Figure 5.4: Energy levels for ^{29}Mg . The ground-state energy value is plotted in the first column. Red points without lines on the y -axis indicate that the J is not known with certainty. The theoretical results, corresponding to different Hamiltonians (USD, USDA and USDB) for the sd -shell, are shown in the last three columns.

occupation for both protons and neutrons. The most abundant neutron configurations involve the three valence neutrons in the $d_{5/2}$ orbital coupled to either spin $3/2$ or $5/2$ and the four valence protons in the same orbital coupled to either spin 0 or 2 , however, those fractions are not large (about 16 % and 18% for the neutron configurations and about 20 % and 11% for the proton configurations, respectively). The protons contribute about 60% of the wave function when they are coupled to spin 2 or 4 . The wave function is very fragmented and a leading configuration can not be highlighted.

Shell model analysis using the USDB Hamiltonian for the neutron-rich isotopes:

- ^{25}Mg . As in ^{23}Mg , no prevailing configuration can be extracted from the calculations. The prominent neutron configuration involves the five valence neutrons in the $d_{5/2}$ orbital coupled to spin $5/2$, in about 17%. The protons contribute in about 60% of the wave function when they are coupled to spin 2 or 4 .
- ^{27}Mg . In the single particle approach, the ground-state configuration of

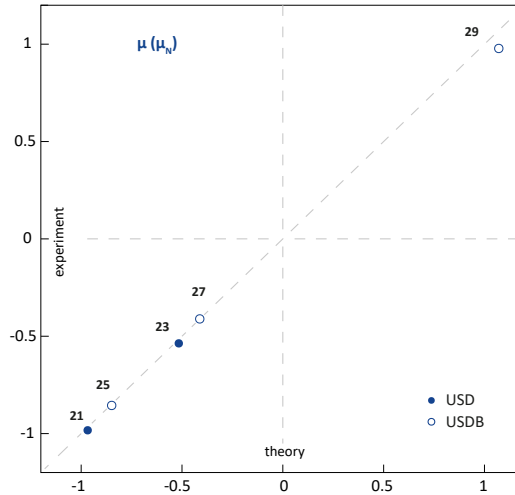




Figure 5.5: Experimental magnetic moments of odd-magnesium isotopes versus calculated values using two different Hamiltonians (USD and USDB) for the sd -shell. Experimental errors are smaller than the dots.

this isotope should be determined by the unpaired neutron in the $s_{1/2}$ shell. Indeed, the most significant contribution of the wave function comes from the single neutron in the $s_{1/2}$ orbital, giving a spin 1/2, and the four valence protons coupled to spin 0, those fractions at 37% and 47%, respectively.

- ^{29}Mg . The leading configuration of the wave function at 60% is given by the protons and neutrons coupled to spin 0 and 3/2, respectively. Inside this contribution, the most abundant neutron and proton configurations contain an unpaired neutron in the $d_{3/2}$ orbital and four protons in $d_{5/2}$, those fractions at 47% and 39%, respectively. This isotope together with ^{27}Mg has been already well discussed in [96].

The predicted magnetic moments for $^{27-29}\text{Mg}$ are in agreement with previous calculations using the shell-model code ANTOINE [96] with the “universal” sd -interactions. The results obtained in this work were included in a publication “Spin and magnetic moment of ^{23}Mg ” that is attached to the thesis.

Spin and magnetic moment of ^{23}Mg

D T Yordanov^{1,2,3} , M L Bissell^{4,5}, K Blaum², M De Rydt⁵,
Ch Geppert^{6,7}, J Krämer^{6,7}, K Kreim², M Kowalska^{2,3},
A Krieger⁷, P Lievens⁸, R Neugart^{2,7}, G Neyens⁵,
W Nörtershäuser^{6,7,9} , L V Rodríguez¹, R Sánchez^{7,9} and
P Vingerhoets⁵

¹ Institut de Physique Nucléaire, CNRS-IN2P3, Université Paris-Sud, Université Paris-Saclay, F-91406 Orsay, France

² Max-Planck-Institut für Kernphysik, Saupfercheckweg 1, D-69117 Heidelberg, Germany

³ Experimental Physics Department, CERN, CH-1211 Geneva 23, Switzerland

⁴ School of Physics and Astronomy, The University of Manchester, Manchester, M13 9PL, United Kingdom

⁵ Instituut voor Kern- en Stralingsfysica, KU Leuven, Celestijnenlaan 200D, B-3001 Leuven, Belgium

⁶ Institut für Kernphysik, Technische Universität Darmstadt, D-64289 Darmstadt, Germany

⁷ Institut für Kernchemie, Universität Mainz, D-55128 Mainz, Germany

⁸ Laboratorium voor Vaste-Stoffysica en Magnetisme, KU Leuven, Celestijnenlaan 200D, B-3001 Leuven, Belgium

⁹ GSI-Helmholtzzentrum für Schwerionenforschung GmbH, D-64291 Darmstadt, Germany

E-mail: Yordanov@ipno.in2p3.fr

Received 23 January 2017, revised 31 March 2017

Accepted for publication 8 May 2017

Published 31 May 2017



CrossMark

Abstract

A negative magnetic moment of ^{23}Mg has been determined by collinear laser spectroscopy at CERN-ISOLDE. The absolute value is in agreement with previous measurements by nuclear magnetic resonance while the sign points at high-seniority configurations. The result is consistent with shell-model predictions for nuclei with valence nucleons in the *sd* shell.

Keywords: laser spectroscopy, nuclear moments, spin

(Some figures may appear in colour only in the online journal)

1. Introduction

Collinear laser spectroscopy was deployed for charge-radii measurements over the magnesium isotopic chain [1]. An important objective was to propagate the study towards both ends of the

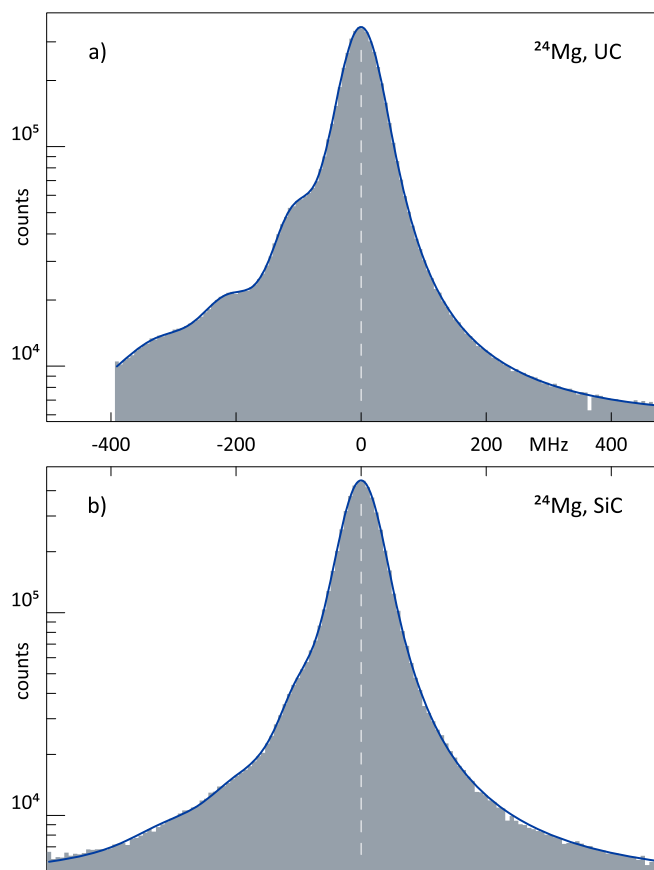


Figure 1. Fluorescence spectra of ^{24}Mg from a UC target (a) and a SiC target (b). The vertical scales are logarithmic.

sd shell where expected cluster configurations on one side and cross-shell excitations on the other would influence the nuclear size. The experiment indeed determined a transition to a deformed configuration at ^{31}Mg , and found a trend of ever increasing radii by the removal of neutrons from the lighter isotopes down to ^{21}Mg . This work combined for the first time fluorescence spectroscopy and laser-induced nuclear orientation for charge-radii measurements. The resulting magnetic moments have never been published, partly because alternative values had already been reported [2–7]. However, ^{23}Mg currently lacks electromagnetic-moments sign determination since it has been examined by nuclear magnetic resonance alone [3, 4, 8]. Furthermore, the associated experimental accuracy is not greater than the one offered by the present study. Apart from its importance from the nuclear-structure point of view, ^{23}Mg is also a key probe for the study of fundamental interactions [9] specifically as a group member of the isospin 1/2 nuclei with mirror β transitions [10]. Below we discuss an independent spin and magnetic-moment measurement of ^{23}Mg , and offer an interpretation in terms of the spherical shell model.

2. Experiment

The experiment was carried out with the collinear laser spectroscopy setup [6] at ISOLDE-CERN. Radioactive nuclei were produced by high-energy protons impinging on a silicon

carbide target. Magnesium atoms were resonantly laser ionized [11], accelerated to an energy of 50 keV and mass separated. The ion of ^{23}Mg was excited in the transition $3s\ ^2S_{1/2} \rightarrow 3p\ ^2P_{1/2}$ at 280.35 nm [12] which is free of quadrupole interactions and has a well resolved hyperfine structure. The corresponding ultraviolet light was produced by frequency doubling the output of a stabilized ring dye laser, using Rhodamine 19 as the active medium, pumped at 532 nm. The ion beam was overlapped with a laser beam and directed through an electrostatic lens for post-acceleration. Atomic excitations were detected in the ion-beam fluorescence as a function of the Doppler-shifted laser frequency.

2.1. Empirical line shapes

Typically, the shape of a spectroscopic line is closely described by the Voigt profile which is a convolution of a Lorentzian function representing the natural absorption profile and a Gaussian component accounting for Doppler broadening due to the thermal motion of the atoms in the ion source. Through the years the Voigt profile has been approximated very accurately by the use of explicit mathematical functions for computational ease [13]. In most applications of collinear laser spectroscopy the Voigt line shape is in agreement with the observations, however, additional effects may also play a role. The spectral lines of ^{24}Mg in figure 1 illustrate the asymmetric line profile associated with the present study. The two measurements are taken under similar conditions in separate experiments. Both clearly show additional structures at the lower-energy side of the main resonance. It should be noted that the apparent effect in figure 1 is exaggerated by the logarithmic scale which has the purpose of magnifying the details at the base of the spectra. Clearly the intruder structures are periodic and seem to resemble the effect of inelastic collisions reported by Bendali and co-workers [14]. In their work a mono-energetic sodium ion beam passed through a sodium vapor for neutralization. Depending on the vapor densities side peaks resulting from multiple inelastic collisions with an energy defect corresponding to the $3s$ - $3p$ energy difference became prominent. The periodicity in our spectra does indeed correspond to a $3s$ - $3p$ excitation in the magnesium ion. However, our measurements do not involve neutralization, therefore the medium causing collisions is likely to be the residual gas in the vacuum beamlines after the point of ionization. In this respect, differences from one experiment to another, such as those in figures 1(a) and (b), could be attributed partly to different vacuum conditions. The collisional excitations reported by Bendali and co-workers represent a particular case of forward scattering where the collision partners are identical atoms. The arrangement in the present work is considerably more complex since molecules and atoms of different masses and ‘softness’ to excitation are involved. A change in the residual-gas density upstream from the ion source may also play a role. Modeling of the exact processes is challenging and would require a dedicated study. In this work we have analyzed the data using a realistic line profile consisting of a main resonance and three equidistant side peaks with positions determined by the $3s$ - $3p$ energy difference in the magnesium ion. High-statistics scans, as the one presented in figure 1(b), have been made throughout the experiment in order to determine the height and the Gaussian width of the individual side peaks relative to the main peak. Subsequently these parameters have been used to fit the isotopes with hyperfine structure. The Lorentzian width, common to all peaks, and the Gaussian width of the main resonance have been maintained as free parameters. With such a line profile we have been able to obtain a very good description of the data, in particular reduced- χ^2 values close to unity have been obtained after fitting.

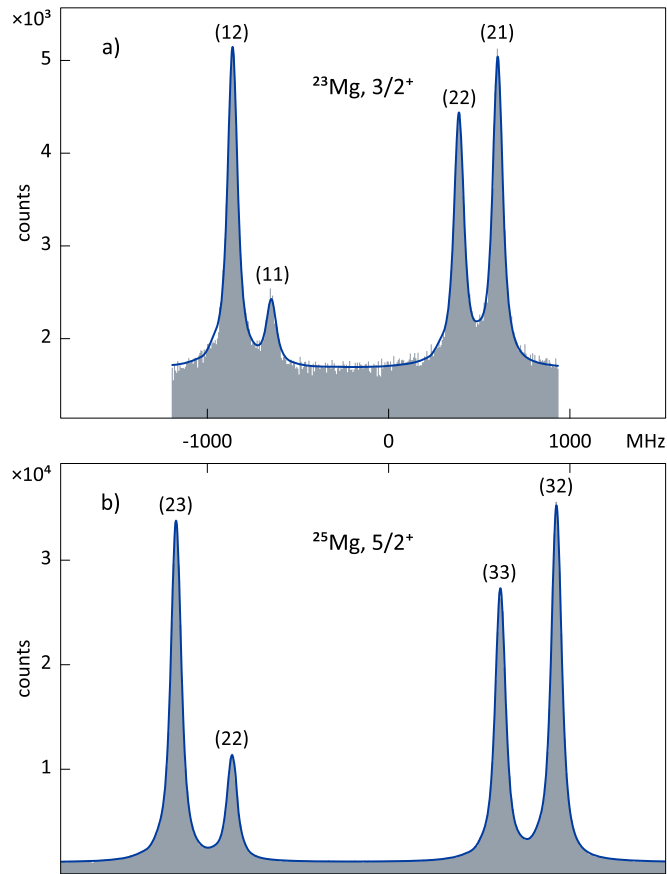


Figure 2. Fluorescence spectra of ^{23}Mg (a) and ^{25}Mg (b). The corresponding F quantum numbers are indicated above the individual transition peaks.

2.2. Magnetic moment

The atomic transition in use is free of quadrupole interactions. The relative positions of individual lines are, therefore, determined by the equation:

$$E_F = A \frac{F(F+1) - I(I+1) - J(J+1)}{2}, \quad (1)$$

applied for both the ground and the excited atomic states, where I is the nuclear spin, J are the respective electronic angular momenta, F are the total angular momenta, and A are the magnetic hyperfine parameters. The hyperfine anomaly in singly-ionized magnesium, taking into consideration the data on atomic sodium [15–17], is expected to be small with respect to the experimental uncertainties in this work. The A factors and the nuclear magnetic moments of any two magnesium isotopes are then related through the expression:

$$A \frac{I}{\mu} = \text{const.} \quad (2)$$

The constant essentially represents the average magnetic field per unit angular momentum induced at the origin by the atomic electrons. Its value is always positive allowing for sign determinations of nuclear magnetic moments directly from hfs measurements.

Table 1. Hyperfine A parameters from this work and a new value for the magnetic moment of ^{23}Mg .

	I	$A (3p \ ^2P_{1/2})$	$A (3s \ ^2S_{1/2})$	μ/μ_N
^{23}Mg	3/2	-107.4(3)	-623.5(3)	-0.5366(3) ^a
^{25}Mg	5/2	-103.1(2)	-596.4(2)	-0.85545(8) ^b

(MHz)

^a Extracted in the $S_{1/2}$ multiplet; uncorrected for hyperfine anomaly; to be compared with $|\mu(^{23}\text{Mg})| = 0.5364(3)\mu_N$ from NMR [3].

^b Reference magnetic moment of ^{25}Mg [18].

Considering the relative intensities of spectral lines, also known as Racah intensities [19], we have identified the hyperfine components in figure 2 and labeled them by the corresponding F quantum numbers. For both isotopes the line doublet starting from the state with the lower angular momentum is also lower in excitation energy. The hyperfine levels of $S_{1/2}$ are therefore inverted with the lower angular-momentum state being higher in energy. This arrangement is characteristic of negative A factors and consequently negative magnetic moments, as evident from the equations above. All experimental results are presented in table 1. The reference isotope is the stable ^{25}Mg whose magnetic resonance has been measured relative to ^{14}N [5]. However, we adopt the reevaluated value from [18] incorporating diamagnetic corrections and later numbers for the proton moment, recently supported by a double Penning-trap measurement [20], and the ^{14}N -to- ^1H frequency ratio [21]. The A factors of ^{25}Mg are consistent with previous studies [6, 22]. The $S_{1/2}$ parameters have been used for determining the final magnetic moment of ^{23}Mg . Without discussing the independent evidence, such as the relative intensities and the isotope shift, the fact that the magnetic moment of ^{23}Mg from this work is in agreement with the result from nuclear magnetic resonance [3] fixes the spin of ^{23}Mg with absolute certainty to $I = 3/2$. Indeed, there can be only one half-integer value that is consistent with the observed $S_{1/2}$ splitting $\Delta\nu = A(I + 1/2)$ and the A factor derived from NMR measurements with the aid of equation (2). With regard to the differential hyperfine anomaly in the $S_{1/2}$ state one is able to calculate $^{25}\Delta^{23} = -0.04(8)\%$ according to the definition in [15] and using the hyperfine parameters in table 1, and the known NMR values [3, 18].

3. Interpretation

A negative magnetic moment can not be generated in the neutron sd shell without a $d_{5/2}$ contribution, hence the $3/2$ ground-state of ^{23}Mg must be determined by multi-particle interactions involving that orbital. Such high-seniority configurations are more likely to occur in the middle of the $d_{5/2}$ shell, and indeed the neighboring odd isotopes ^{21}Mg and ^{25}Mg both have ground-state spins of $5/2$ as one would expect from normal coupling. An equivalent spin change also occurs in the respective mirror partners, namely along the $N = 12$ isotonic chain of ^{21}F , ^{23}Na and ^{25}Al . The magnetic moment of ^{23}Mg has been previously discussed in the framework of isospin $1/2$ mirror doublets in the sd shell [3]. To gain a further insight into the configurations involved we have carried out shell-model calculations with the universal sd Hamiltonians USD [23] and USDB [24] using the code NuShellX @ MSU [25]. Experiment and theory are plotted against each other in figure 3 for all odd magnesium isotopes in the sd shell, except ^{31}Mg whose ground state involves particle-hole excitations into the pf shell [7].

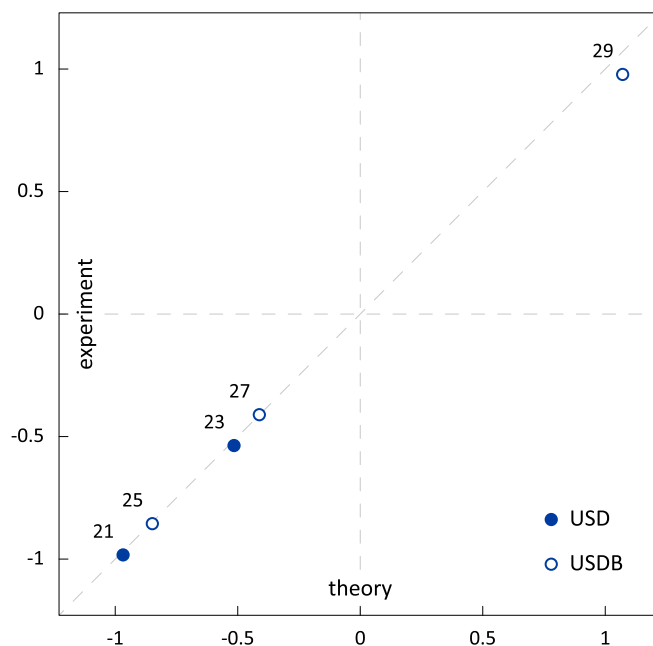


Figure 3. Ground-state magnetic moments of magnesium isotopes in the sd shell in units μ_N , versus shell model calculations. The respective mass numbers are indicated. The experimental uncertainties are smaller than the dots.

In line with our previous findings [2, 6], in the beginning of the sd shell the USD interaction generates more accurate results, whereas already by midshell the USDB Hamiltonian is required, particularly for predicting the correct level ordering in ^{29}Mg . In all calculations free g factors have been used. The agreement between theory and experiment is generally good. In the case of ^{23}Mg it is the USD interaction that approaches the magnetic moment closer by the value $-0.52 \mu_N$. As expected, the $d_{5/2}$ orbital is dominant with about 75% occupation for both protons and neutrons. The protons do indeed play an important role since they undergo 2^+ or 4^+ coupling in about 60% of the wave function. The most abundant neutron configurations contain the three valence neutrons in the $d_{5/2}$ orbital coupled to either spin $3/2$ or $5/2$, but those fractions at 16% and 18%, respectively, are not large. In reality the wave function is very fragmented and a dominant configuration can not be highlighted. As to the magnetic moment of ^{31}Mg , a very close match with the USDB value $-0.83 \mu_N$ of the lowest $1/2^+$ state in ^{29}Mg has been previously pointed out [26, 27]. This is consistent with the picture of a cross-shell excitation of two paired neutrons which do not contribute directly to the magnetic moment. If the corresponding point was to be added in figure 3, similarly to the other cases it would lie close to the identity line.

4. Summary

In brief, we have studied ^{23}Mg by high-resolution collinear laser spectroscopy. An empirical approach to the observed spectroscopic line shapes has been discussed. The ground-state spin $3/2$ has been confirmed and a negative magnetic moment has been measured, thus highlighting the importance of high-seniority configurations. The absolute value is found

consistent with previous studies by nuclear magnetic resonance. The odd magnesium isotopes in the sd shell have been investigated in the framework of the spherical shell model using the well-known universal sd Hamiltonians. The calculation on ^{23}Mg , indeed points to a strong $d_{5/2}$ contribution from both protons and neutrons and only a minor occupation of the neutron $d_{3/2}$ shell.

Acknowledgments

This work has been supported by the Max-Planck Society, the German Federal Ministry for Education and Research under contract no. 06MZ9178I, the Helmholtz Association (VH-NG-148), the P6-EURONS (RII3-CT-2004-506065), the BriX IAP Research Program (P6/23), and the FWO-Vlaanderen. We thank the ISOLDE technical group for their professional assistance.

ORCID

D T Yordanov  <https://orcid.org/0000-0002-1592-7779>

W Nörtershäuser  <https://orcid.org/0000-0001-7432-3687>

References

- [1] Yordanov D T *et al* 2012 *Phys. Rev. Lett.* **108** 042504
- [2] Krämer J *et al* 2009 *Phys. Lett. B* **678** 465
- [3] Fukuda M *et al* 1993 *Phys. Lett. B* **307** 278
- [4] Lindroos M *et al* 1997 *Nucl. Instrum. Methods Phys. Res., Sect. B* **126** 423
- [5] Alder F and Yu F C 1951 *Phys. Rev.* **82** 105
- [6] Kowalska M *et al* 2008 *Phys. Rev. C* **77** 034307
- [7] Neyens G *et al* 2005 *Phys. Rev. Lett.* **94** 022501
- [8] Matsuta K *et al* 1999 *Hyp. Interact.* **120/121** 673
- [9] Severijns N and Naviliat-Cuncic O 2011 *Annu. Rev. Nucl. Part. Sci.* **61** 23
- [10] Severijns N, Phaet M T T and Towner I S 2008 *Phys. Rev. C* **78** 055501
- [11] Köster U *et al* 2003 *Nucl. Instrum. Methods Phys. Res., Sect. B* **204** 347
- [12] Kaufman V and Martin W C 1991 *J. Phys. Chem. Ref. Data* **20** 83
- [13] Ida T, Ando M and Toraya H 2000 *J. Appl. Cryst.* **33** 1311
- [14] Bendali N *et al* 1986 *J. Phys. B: At. Mol. Phys.* **19** 233
- [15] Persson J R 2013 *At. Data Nucl. Data tables* **99** 62
- [16] Chan Y W, Cohen V W, Lipsicas M and Silsbee H B 1966 *Phys. Rev.* **150** 933
- [17] Beckmann A, Böklen K D and Elke D 1973 *Z. Phys.* **270** 173
- [18] Raghavan P 1989 *At. Data Nucl. Data tables* **42** 189
- [19] Magnante P C and Stroke H H 1969 *J. Opt. Soc. Am.* **59** 836
- [20] Mooser A *et al* 2014 *Nature* **509** 596
- [21] Fuller G H 1976 *J. Phys. Chem. Ref. Data* **5** 835
- [22] Itano W M and Wineland D J 1981 *Phys. Rev. A* **24** 1364
- [23] Wildenthal B 1984 *Prog. Part. Nucl. Phys.* **11** 5
- [24] Brown B A and Richter W A 2006 *Phys. Rev. C* **74** 034315
- [25] Brown B A and Rae W 2014 *Nucl. Data Sheets* **120** 115
- [26] Brown B A 2005 *Discussion at the Gordon Research Conf. on Nuclear Chemistry*
- [27] Neyens G 2011 *Phys. Rev. C* **84** 064310

Acknowledgments

I would like to thank all the people who have accompanied me during these three years of challenges and adventures.

To Dr. Deyan Yordanov, for whom I have the honor of being the first Ph.D. student, for giving me the opportunity to work on such an incredible research topic. Working under his supervision not only allowed me to gain a deep insight into the field of experimental nuclear physics but also enabled me to grow as a research scientist. For all the unforgettable experiences at IPN/CERN and *for showing me the snow for the first time!*,

To the COLLAPS collaboration, for the invaluable work carried out during the experiments,

To the ISOLDE technical group and the RILIS team, for their extraordinary support,

To Dr. Serge Franchoo, for all his advice and for making me feel part of the laser team,

To Prof. Klaus Blaum, for giving me the opportunity to experience being a scientist at CERN now as part of his group,

To Jackes and Celine, for being like my family in France,

To all my friends and colleagues, for all our moments of happiness,

To my friend Tais, for our life-long (10 years ;)) friendship,

To my family, for their infinite support and love,

To the chiral center of my life, *Ariel, por ser la otra mitad del liaf-team,*

Muchas gracias!

Titre : Spectroscopie laser de l'étain au-delà de $N = 82$

Mots clés : Spectroscopie laser colinéaire - Structure nucléaire - Paramètres hyperfins - Moments électromagnétiques - Rayon de charge

Résumé : L'objectif de cette thèse est l'étude par spectroscopie laser colinéaire à haute résolution de la structure nucléaire des isotopes d'étain riches en neutrons, vers de la fermeture de couche $N = 82$ et au-delà. Les structures hyperfines et les déplacements isotopiques le long de $^{108-134}\text{Sn}$ ont été mesurés en utilisant l'expérience COLLAPS à ISOLDE au CERN. Deux expériences indépendantes, utilisant des propriétés de transitions complémentaires l'une à 452 et l'autre à 286 nanomètres, ont étudiées les états $5p6s^1P_1$ et $5p6s^3P_1$ dans l'atome neutre. L'état singulet fournit une sensibilité élevée au moment quadropolaire tandis que le triplet facilite une grande séparation magnétique. A partir d'une analyse auto-cohérente des deux en-

sembles de données, les spins nucléaires, les moments électromagnétiques et les rayons de charge ont été extraits. Les propriétés des isomères à vie longue des noyaux $^{113,123,128}\text{Sn}$ ainsi que l'état fondamental de ^{133}Sn et ^{134}Sn ont été évalués pour la première fois. Les moments quadropolaires des états $11/2^-$, déterminés avec une plus grande précision que les études précédentes, suivent une tendance presque linéaire. Un coude à $N = 82$ dans la courbe des rayons a été observé pour la première fois. Des calculs de champ moyen fournissent une description précise des rayons et relie en outre la tendance globale aux corrélations provenant des fluctuations des moments quadropolaires

Title : Laser spectroscopy of tin across $N = 82$

Keywords : Collinear laser spectroscopy - Nuclear structure - Hyperfine parameters - Isotope shift - Electromagnetic moments - Charge radii

Abstract : The aim of this thesis is the study of nuclear structure properties of the neutron-rich Sn isotopes towards the $N = 82$ shell closure and beyond by high-resolution collinear laser spectroscopy. The hyperfine structures and isotope shifts along $^{108-134}\text{Sn}$ were measured using the COLLAPS instrumentation at ISOLDE, CERN. Two independent experiments using transitions with complementary properties, respectively at 452 and 286 nanometres studied the $5p6s^1P_1$ and the $5p6s^3P_1$ states in the neutral atom. The singlet state provided high sensitivity to quadrupole moments while the triplet facilitated a large magnetic splitting. From a self-consistent analysis of

the two data sets, nuclear spins, electromagnetic moments and charge radii have been extracted. The properties of the long-lived isomers in $^{113,123,128}\text{Sn}$ and the ground state of ^{133}Sn and ^{134}Sn have been assessed for the first time. The quadrupole moments of the $11/2^-$ states, determined with much higher precision than in previous studies, have been found to follow a nearly linear trend. A "kink" in the radii trend at $N = 82$ was observed for the first time. Beyond mean-field calculations provide an accurate description of the radii and further relate the overall trend to correlations stemming from the fluctuations of the quadrupole moments.

